A STUDY OF THE REACTION $p + p \rightarrow p + p + \pi^0$ FROM 320 MeV TO 500 MeV

By

THANTHIRIMUDALIGE DON SHIRVEL STANISLAUS

B.Sc., University of Sri Lanka, 1976

M.Sc., University of British Columbia, 1983

A THESIS SUBMITTED IN PARTIAL FULFILLMENT OF

THE REQUIREMENTS FOR THE DEGREE OF

DOCTOR OF PHILOSOPHY

in

THE FACULTY OF GRADUATE STUDIES

Department of Physics

We accept this thesis as conforming

to the required standard

THE UNIVERSITY OF BRITISH COLUMBIA

December 1987

In presenting this thesis in partial fulfilment of the requirements for an advanced degree at the University of British Columbia, I agree that the Library shall make it freely available for reference and study. I further agree that permission for extensive copying of this thesis for scholarly purposes may be granted by the head of my department or by his or her representatives. It is understood that copying or publication of this thesis for financial gain shall not be allowed without my written permission.

Department of Physics

The University of British Columbia
1956 Main Mall
Vancouver, Canada
V6T 1Y3

Date 29 / March / 1988

Abstract

The reaction $p+p \rightarrow p+p+\pi^0$ has been studied from threshold up to 500 MeV, by detecting the decay γ-rays of the π^0 in coincidence in two large NaI crystals (TINA and MINA). It was possible to measure the energy spectra, the differential cross sections and the asymmetry of the π^0.

The total cross sections and the angular distribution parameter b (defined by $\frac{d\sigma}{d\Omega} \propto \frac{1}{3}+b\ cos^2\theta$) determined in this measurement are consistent with previous measurements, but are of a much higher precision. The value obtained for b is very small indicating that most of the π^0 mesons are isotropically distributed in the centre of mass. Assuming the energy spectra predicted by Gell-Mann, we have deduced the intensities of the Ss, Ps and Pp transitions by a global fit to all the energy spectra and the resulting cross sections. For Ss we obtained $\sigma_T^{Ss} = (15.2 \pm 3.0)\eta_0^2$ (μb) which is smaller and more accurate than the previous measurements. A model independent σ_T^{Ss} would have an uncertainty of about 6 μb.

We have compared our results with those of the reaction $n+p \rightarrow N+N+\pi^{\pm}$ and found them to be fairly similar. Any difference would demand inelasticities in the I=0 channels, but the total cross sections indicate that σ_{01} is small.The centre of mass pion energy spectra for $pp \rightarrow pp\pi^0$ and $np \rightarrow nn\pi^+$ are also similar. However a large $cos\theta$ term is observed in the $\pi^{\pm}$ differential cross sections from the np reaction which is an indication of a significant value for σ_{01}.

The analysing powers are fairly large and negative. This is the first measurement of this observable, although evidence from the reaction $^{13}C(p,\pi^-)$ had suggested that the asymmetry in the free $pn \rightarrow pp\pi^-$ reaction might be positive.

Contents

List of Tables

List of Figures

Acknowledgements

I would like to extend my sincere gratitude and appreciation to my supervisor Professor David F. Measday for introducing me to this topic, for his assistance during the experiment and for his guidance, advice and criticism. His support and patience throughout this work has been a great source of encouragement for me.

For the smooth, orderly progress of the experiment I would like to thank Dr. Dezsö Horvàth, Dr. Martin Salomon, Tony Noble and Muna Ahmad, without whose assistance it would not have been successfully completed. Dezsö Horvàth is also thanked for very useful discussions and advice during the analysis of the data and the preparation of the thesis.

I would also like to thank Dr. Dave Hutcheon for his advice and assistance in the preparation and running of the experiment. I would also like to express my thanks to Dr. Farrokh Entezami for his invaluable assistance during the initial stages of this research.

For designing and constructing the liquid hydrogen target I am grateful to Alan Morgan and Walter Kellner. Jean Holt of the Physics Department is thanked for drawing some of the figures for this thesis.

I wish to thank my wife, Susila for her patience, support and understanding during the last 3 years.

Finally, I wish to thank my parents for their continuous help and encouragement. However, it is deeply regretted that they could not see the completion of my work at UBC.

Dedication

To

the loving memory of

my mother

Chapter 1

Introduction

The nucleon-nucleon interaction is one of the most important problems in nuclear and particle physics, and has been studied extensively both experimentally and theoretically over a very wide energy range. In nuclear physics a clear understanding of the nucleon-nucleon force leads to a better understanding of the properties of nuclei, and in particle physics, the nucleon-nucleon interaction is intimately related to an understanding of the hadrons. At low energies nucleon-nucleon scattering is mainly elastic, apart from a very small amount of bremsstrahlung production and neutron-proton capture. The inelastic channel $NN \rightarrow NN\pi$ becomes energetically possible around 290 MeV, and the cross section for this channel rises very quickly as a function of energy. For proton-proton collisions around 900 MeV the total inelastic cross section equals the elastic scattering cross section [1]. Double pion production has a threshold around 590 MeV, but has negligible cross-section even at 800 MeV [2],and does not become significant until $\Delta\Delta$ production becomes energetically possible at about 1000 MeV.

1.1 Isotopic Spin Decomposition

For pion production reactions near threshold, Watson and Brueckner [3] showed that the characteristics of the data could be interpreted using the laws of conservation of angular momentum, parity and isotopic spin. In the isospin notation of Rosenfeld [4], the total cross section for a reaction is denoted by σ_{if} where i is the initial and f is the final isotopic spin of the two-nucleon system. Thus for single

Table 1.1: Isotopic spin decomposition for total cross sections.

	Reaction	Isotopic spin decomposition
(a)	$p+p \rightarrow d+\pi^+$	$\sigma_{10}(d)$
(b)	$p+p \rightarrow n+p+\pi^+$	$\sigma_{10}(np)+\sigma_{11}$
(c)	$p+p \rightarrow p+p+\pi^0$	σ_{11}
(d)	$n+p \rightarrow d+\pi^0$	$\frac{1}{2}\sigma_{10}(d)$
(e)	$n+p \rightarrow n+p+\pi^0$	$\frac{1}{2}[\sigma_{10}(np)+\sigma_{01}]$
(f)	$n+p \rightarrow n+n+\pi^+$	$\frac{1}{2}[\sigma_{11}+\sigma_{01}]$
(g)	$n+p \rightarrow p+p+\pi^-$	$\frac{1}{2}[\sigma_{11}+\sigma_{01}]$
(i)	$n+n \rightarrow n+p+\pi^-$	$\sigma_{10}(np)+\sigma_{11}$
(j)	$n+n \rightarrow d+\pi^-$	$\sigma_{10}(d)$
(k)	$n+n \rightarrow n+n+\pi^0$	σ_{11}

pion production there are four cross sections, $\sigma_{10}(d)$, $\sigma_{10}(np)$, σ_{11} and σ_{01}. $\sigma_{10}(d)$ and $\sigma_{10}(np)$ represent reactions with a deuteron and unbound neutron and proton in the final state respectively. All the possible reactions can be expressed in terms of these independent cross sections and are listed in table 1.1. There is no σ_{00} for np collisions, since, the pion has isotopic spin 1 and so the 0 to 0 transition does not conserve isotopic spin.

Since the Coulomb interaction breaks isotopic spin invariance, these relations are subject to corrections of a few percent. A major contribution is the mass difference of the $\pi^{\pm}$ and π^0 (4.5 MeV in 140 MeV), which is itself a symptom of the Coulomb interaction. Two features to be noted from table 1.1 are:

1. In n-p collisions, the cross sections for the production of π^+ and π^- are equal.

2. The cross section for deuteron production in n-p collisions is half that in p-p collisions.

As can be seen from table 1.1, a very clean feature of the reaction that we are interested in, $pp \rightarrow pp\pi^0$, is that it involves only σ_{11}. Similarly, $\sigma_{10}(d)$ can be independently measured and of the four elementary cross sections this has been the one most extensively studied, mainly because:-

- it involves only two bodies in the final state
- the inverse reaction $\pi d \rightarrow pp$ can also be investigated
- for $pp \rightarrow \pi^+ d$ all the particles are charged and thus easy to detect
- near threshold $\sigma_{10}(d)$ has a relatively large cross section.

Thus a full amplitude analysis of $pp \rightarrow \pi^+ d$ has been attempted [5,6] and most major amplitudes are now fairly well determined. As for $\sigma_{10}(np)$, the cross-section is fairly well established at the present time; there are some asymmetry and spin transfer data, but by no means a complete set of measurements.

Using all the available experimental data from pion production reactions a phase shift analysis has been done by VerWest and Arndt [7] who have thus determined the relative strengths of the four elementary cross sections. The energy dependence of these cross sections are shown in Figure 1.1. Their results show that σ_{01} is small up to about 1000 MeV but at present there is a fair amount of inconsistency between the various estimates of σ_{01}.

1.2 Angular Momentum Analysis

The elementary partial cross sections $\sigma_{10}(d)$, $\sigma_{10}(np)$, σ_{11} and σ_{01} can be broken down to several "intensity classes" in terms of the angular momentum of the final

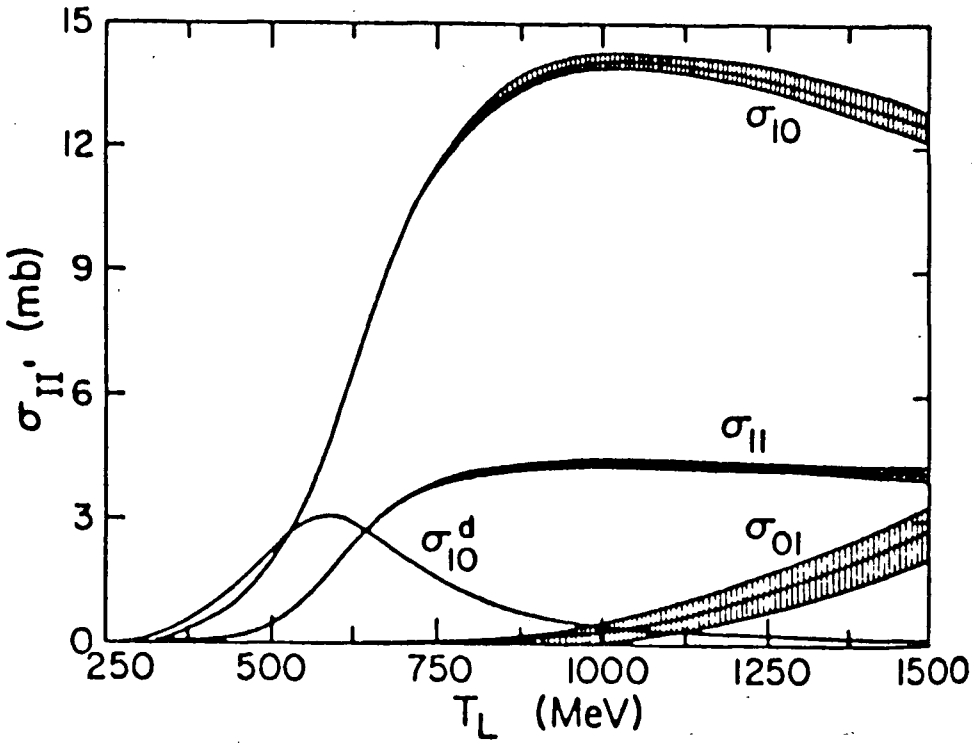

Figure 1.1: Energy dependence of the elementary cross sections.

two-nucleon system and the angular momentum of the pion [4]. It has been shown that near threshold, $l \geq 2$ could be neglected, and the final state partial waves can be classified in order of decreasing intensity as Sp, Ss, Pp and Ps. The first letter of an intensity class (S,P) refers to the relative angular momentum of the two nucleons in the final state while the second letter (s,p) refers to the angular momentum of the pion with respect to the centre of mass of the two nucleons. The allowed reactions of these intensity classes are listed in table 1.2, grouped according to the elementary cross sections and further grouped according to the intensity class. The notation used for the initial and final states of the two nucleons is $^{2S+1}L_J$ where S is the spin, L is the orbital angular momentum and J is the total angular momentum of the two nucleons. For the final state of the pion, the notation is l_J where l refer to

the orbital angular momentum of the pion and J is the total angular momentum. In table 1.2, η is the momentum of the pion in the centre of mass in units of the pion mass i.e. $\eta = \frac{P_\pi}{\mu c}$ and η_0 is the maximum momentum of the pion in the same units.

As can be seen from the table, for the reaction $pp \rightarrow pp\pi^0$, the transition Sp, which plays a major role in other meson production reactions, is forbidden due to isosin, spin and parity considerations. The ${}^1S_0p_1$ state is 1^+ and is not available in the initial pp state whereas the ${}^3S_1p_{0,2}$ transitions are allowed for the π^+ producing reactions. The absence of the Sp class is responsible for the relatively small cross sections near threshold for the $pp \rightarrow pp\pi^0$ reaction. Also it turns out that for this reaction it is impossible to explain the experimental excitation function by invoking Ss alone [4]. Therefore, for σ_{11} only, reactions of classes Pp and Ps must be considered even near threshold. (They are present in the π^+ channels, but need not be considered in a crude analysis at TRIUMF energies.)

In some simple cases, the expected angular distributions of the pions have been derived [1]. If the total angular momentum is zero or if the pion is produced in an s state, then the distribution will be isotropic. If the meson is produced in a p state and if J$\geq$1 the angular distribution takes the form $C + cos^2\theta$. The expected angular distributions of each class are also listed in the fifth column of table 1.2. These angular distributions of the pions can be used to identify the dominant transitions.

1.3 Pion Spectra and The Excitation Function

Differential energy spectra of the pions produced in the $NN \rightarrow NN\pi$ reaction have been calculated by Gell-Mann and Watson [8]. In the $pp \rightarrow pp\pi^0$ reaction let the incident energy of the bombarding protons be such that in the centre of mass a kinetic energy of T_0 is available after the reaction. Of this an amount T is taken by the pion and $E = T_0 - T$ is taken by the internal motion of the two-nucleon system

Table 1.2: Transitions of low partial waves which describe single pion production

Isotopic reaction	Class	Initial state	Final state	Angular distribution	Energy dependence
$\sigma_{10}(d)$	Ss	$^3P_1$	$^3S_1s_1$	Isotropic	η
	Sp	$^1S_0$	$^3S_1p_0$	Isotropic	η^3
		$^1D_2$	$^3S_1p_2$	$\frac{1}{3}+cos^2\theta$	η^3
$\sigma_{10}(np)$	Ss	$^3P_1$	$^3S_1s_1$	Isotropic	η_0^2
	Sp	$^1S_0$	$^3S_1p_0$	Isotropic	η_0^4
		$^1D_2$	$^3S_1p_2$	$\frac{1}{3}+cos^2\theta$	η_0^4
σ_{01}	Sp	$^3S_1$	$^1S_0p_1$	Isotropic	η_0^4
		$^3D_1$	$^1S_0p_1$	$\frac{1}{3}+cos^2\theta$	η_0^4
σ_{11}	Ss	$^3P_0$	$^1S_0s_0$	Isotropic	η_0^2
	Pp	$^3P_1$	$^3P_0p_1$	$C+cos^2\theta$	η_0^8
		$^3P_{0,1,2}$ or $^3F_2$	$^3P_1p_{0,1,2}$	$C+cos^2\theta$	η_0^8
		$^3P_{1,2}$ or $^3F_{2,3}$	$^3P_2p_{1,2,3}$	$C+cos^2\theta$	η_0^8
	Ps	$^1S_0$	$^3P_0s_0$	Isotropic	η_0^6
		$^1D_2$	$^3P_2s_2$	Isotropic	η_0^6

(neglecting recoil). The differential (energy) cross sections for the various classes of reactions have been obtained as [8]

$$\left(\frac{d\sigma_{11}}{dT}\right)_{Ss} \propto \eta\frac{(T_0-T)^{\frac{1}{2}}}{(T_0-T-B')} \tag{1.1}$$

$$\left(\frac{d\sigma_{11}}{dT}\right)_{Pp} \propto \eta^3(T_0-T)^{\frac{3}{2}} \tag{1.2}$$

$$\left(\frac{d\sigma_{11}}{dT}\right)_{Ps} \propto \eta(T_0-T)^{\frac{3}{2}} \tag{1.3}$$

Here B' is the energy of the two nucleons in a virtual $^1S_0$ state and is considered to be essentially zero ($\approx$ 60 keV). Typical spectra are shown in Figure 1.2.

From the above equations the total cross sections near threshold takes the form:

$$(\sigma_{11})_{Ss} \propto \eta_0^2 \tag{1.4}$$

$$(\sigma_{11})_{Pp} \propto \eta_0^8 \tag{1.5}$$

$$(\sigma_{11})_{Ps} \propto \eta_0^6 \tag{1.6}$$

These energy dependences are listed in the last column of table 1.2. Using the contributions from the three classes towards the total cross section, the experimental results can thus be described by an excitation function of the form

$$\sigma_{11} = B_1\eta_0^2 + B_2\eta_0^6 + B_3\eta_0^8 \tag{1.7}$$

where B_1, B_2 and B_3 are empirical parameters which provide a measure of the contributions to the total cross section of reaction (c) in table 1.1. Similar excitation functions can be written for all other reactions of table 1.1.

1.4 Previous Experiments

The first measurements of the cross section of the reaction $pp \rightarrow pp\pi^0$ were carried out in 1952 at the University of Chicago by Marshall et al. [9]. The

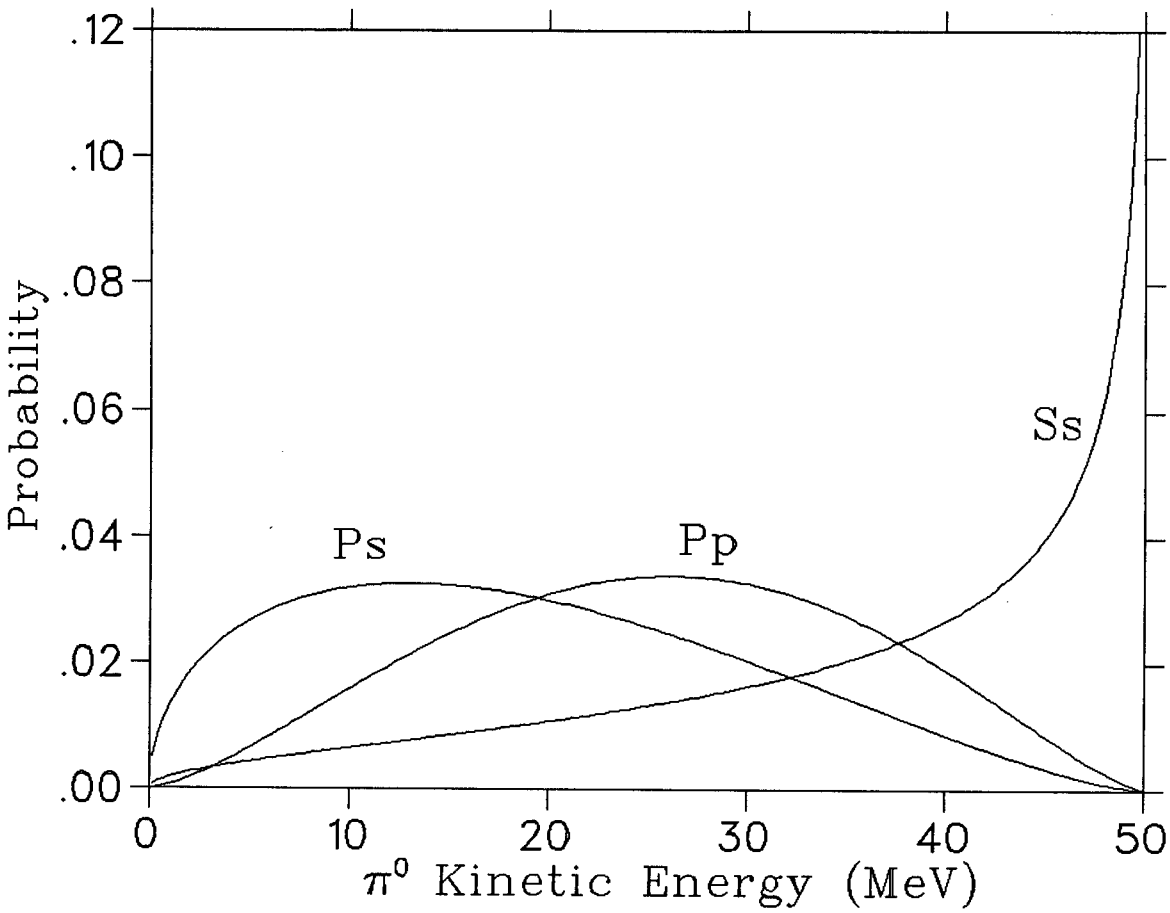

Figure 1.2: Centre of mass energy distributions of pions for the three classes Ss, Ps and Pp for an incident proton energy of 400 MeV [8].

experiment performed at an incident proton energy of 430 MeV produced a result of $450 \pm 150 \mu b$. Since then a number of other near threshold investigations have been done by Mather and Martinelli [10], Soroko [11], Moyer and Squire [12], Prokoshkin and Tiapkin [13], Stallwood et al. [14], Dunaitsev and Prokoshkin [15] and Shimizu et al. [16]. Of these except for the last, all were done during the period 1953 to 1959, the most extensive investigations being those of Stallwood et al. and Dunaitsev and Prokoshkin. Most of these measurements are effectively total cross sections and near threshold the quality is fairly poor.

Stallwood et al. studied the reaction $pp \rightarrow pp\pi^0$ by detecting the decay γ-rays from π^0 production in pp collisions for proton energies ranging from 346 to 437 MeV. Using their own data, as well as those of Mather and Martelli, and Moyer and Squire, they found that σ_{11} is best expressed by

$$\sigma_{11}(\mu b) = (27 \pm 10)\eta_0^2 - (25 \pm 90)\eta_0^6 + (75 \pm 70)\eta_0^8 \tag{1.8}$$

This is clearly non physical as the coefficients B_n should be positive. Assuming a negligible contribution from the Pp class of transitions, their best fit was

$$\sigma_{11}(\mu b) = (19 \pm 6)\eta_0^2 + (62 \pm 15)\eta_0^6 \tag{1.9}$$

Dunaitsev and Prokoshkin performed a very similar experiment in the proton energy range of 313 to 665 MeV. For energies less than 400 MeV they found as their best fit

$$\sigma_{11}(\mu b) = (32 \pm 7)\eta_0^2 + 40\eta_0^6 + 47\eta_0^8 \tag{1.10}$$

(The coefficients of the η_0^6 and η_0^8 were held fixed at the Mandelstam values; see section 2.1)

Thus values of the parameter B_1 vary from 19 to 32 μb with errors which are probably under-estimated. This means that none of these experiments had the necessary accuracy to test the validity of the expression 1.7.

The only recent measurement was that of Shimizu et al. [16]. This bubble chamber experiment done at KEK produced a lot of useful data on pion production in the pp system for $325 < T_P < 1262$ MeV. However their two points below 500 MeV on the reaction $pp \rightarrow pp\pi^0$ are clearly out of line. (This will be illustrated later in Figure 5.1)

Except for the measurements of Dunaitsev and Prokoshkin [15], all of the other experiments measured only the total cross sections of reaction (c). Dunaitsev and Prokoshkin were able to obtain the angular distributions of the pions from the γ-ray spectra, but the quality of their results is not very good, mainly because of the very poor information they had on the energy distributions of the γ-rays. The only experiment that had fairly good energy information was that of Cence et al. [17], but this was done at the higher energy of 735 MeV. From their γ-ray energy spectra they were able to deduce the π^0 energy spectra in the centre of mass.

The differential cross section for the pion is normally described by

$$\left(\frac{d\sigma}{d\Omega}\right) \propto \frac{1}{3} + b\ cos^2\theta \tag{1.11}$$

For the b parameter Dunaitsev and Prokoshkin [15] found a value of 0.06 ± 0.06 between 400 MeV and 675 MeV, Guzhavin observed 0.04 ± 0.015 at 650 MeV [18], whereas at 735 MeV Cence et al. obtained $b = 0.27 \pm 0.04$

The analysing power for the pion is defined as the ratio of the polarised to unpolarised differential cross sections. Although analysing powers have been measured for some pion producing pp reactions ($pp \rightarrow \pi^+ d$ and $pp \rightarrow pn\pi^+$), until the present experiment no measurement had been done for the reaction $pp \rightarrow pp\pi^0$.

1.5 $pp \rightarrow pp\pi^0$ and $np \rightarrow NN\pi^{\pm}$

In section 1.1 it was mentioned that σ_{01} has been found to be small up to about 1000 MeV. An important consequence of this is that if σ_{01} is negligible, then the

reactions $np \rightarrow NN\pi^{\pm}$ would be similar to the reaction $pp \rightarrow pp\pi^0$. In fact there has been a long and complex history as to whether σ_{01} is indeed non-zero.

In the Isobar model [19]

$$NN \rightarrow N\Delta \rightarrow NN\pi \tag{1.12}$$

the intermediate state can have isospin $(\frac{3}{2} \pm \frac{1}{2})$. Therefore, if isospin is conserved, there can be no pion production from an initial I=0 state in the np reaction. Hence σ_{01} can occur only via other mechanisms and would be smaller than the main channels.

The most sensitive indicator of a non-zero σ_{01} is the existence of a $cos\theta$ term in the angular distribution of the $\pi^{\pm}$ for the np reaction. If σ_{01} is zero, the reactions $np \rightarrow NN\pi^{\pm}$ are identical to $pp \rightarrow pp\pi^0$, and so in the angular distribution of the pions, a $cos\theta$ term is forbidden.

The work of Handler [20] in 1965 shows clear evidence for a fairly large $cos\theta$ term for the reaction $np \rightarrow pp\pi^-$ at 409 MeV. At SIN, Kleinschmidt et al. [21] hypothesized that, σ_{01} was small for $np \rightarrow nn\pi^+$ between 470 and 590 MeV. Unfortunately this measurement lacked sufficient angular information as they studied only small angles up to 35^0 in the centre of mass. The recent results of the same group [22], combined with the earlier measurements, seem to indicate the existence of a fairly significant $cos\theta$ term very much in line with Handler and with Dubna work at 600 MeV [23]. However at LAMPF Thomas et al. [24] studied both π^+ and π^- producing np reactions quite extensively and found little evidence for a $cos\theta$ term nor for σ_{01} at 800 MeV. The bubble chamber work of Dakhno et al. [25] from Gatchina produced total cross section measurement and also shows that σ_{01} is small. Thus the evidence is fairly uncertain regarding the exact characteristics of σ_{01}.

1.6 Phase Shift Analyses

Phase shift analyses have played an important part in our understanding of the nucleon nucleon interaction. They are the most successful of phenomenological approaches to the determination of the nucleon nucleon amplitude in the intermediate energy range [26]. These analyses are of interest for the light they shed on NN inelasticity and the possible existence of dibaryon resonances. At present phase shift analyses provide excellent results for pp scattering up to 1 GeV and np scattering up to 500 MeV [5]. The situation with regard to the NN inelastic scattering is far from satisfactory. Only the amplitudes for the $NN \rightarrow \pi^+ d$ reaction are fairly well established [6,27,28]. Of the other pion producing reactions, some analysis exists for the $pp \rightarrow pn\pi^+$ [5,29], although it is not complete. The I=0 phase shifts are not well determined. Above 500 MeV, there is scatter in partial wave parameters in the I=0 state, which is an indication of paucity in the np data base [30,26]. Bystricky et al. [26] indicate that a precise measurement of the total cross-section of the reaction $np \rightarrow np\pi^0$ is crucial for the determination of the I=0 imaginary parts of the phase shifts. An easier way of obtaining this information would be to study the reactions $np \rightarrow \pi^+ NN$, because such experiments are relatively simple to perform.

1.7 Motivation

As mentioned earlier the experimental situation with regard to the reaction $pp \rightarrow pp\pi^0$ was very poor. Near threshold even the total cross sections were not very precise, nor had the π^0 energy spectra been measured near threshold. From the available data it had not been possible to extract reliably the S wave contributions to the reaction near threshold and thus the exact form of the excitation function was not known. Up to now no polarization observables have ever been measured.

There is a lot of interest and uncertainty about the nature of σ_{01}. A precise

measurement of σ_{11}, along with an equally good measurement of the np reaction, could solve the problem once and for all. A $np \rightarrow pp\pi^-$ measurement is scheduled to begin taking data at TRIUMF in the summer of 1988 [31].

The situation with regard to theory is no better (see chapter 2). None of the existing models provide a complete picture of the existing $NN \rightarrow NN\pi$ data. For most of the existing models, no predictions have been made of the reaction $pp \rightarrow pp\pi^0$ mainly because there isn't enough data with which to compare the calculations.

Hence it was decided to study the reaction $pp \rightarrow pp\pi^0$ over a wide range of energies (319 MeV to 497 MeV) and angles (40^0 to 140^0 in the laboratory). Measurements were made of the total and differential cross sections as well as the analysing powers.

Chapter 2

Theory

Many attempts have been made over the last 35 years to calculate pion production cross sections for nucleon nucleon collisions. The first major step forward was made by Mandelstam who ascribed all pion production to excitation of the nucleon to a delta with subsequent decay to a pion. This model described the gross features and has been retained in most subsequent calculations. In the 60's most of the calculations were centred on the soft pion approach and peripheral calculations. After a rather quiet period in the early 70's the field has been revived recently by a number of new calculations. The most successful has been the Faddeev approach of Dubach, Kloet and Silbar which has benefitted from a close co-operation with experimentalists at LAMPF. A new endeavour has been to incorporate quark effects into the calculations. So far no model has been very successful in reproducing overall experimental results other than being in qualitative agreement with experiment. In this chapter some of the theoretical calculations done so far will be very briefly outlined. The literature is vast and it will be possible to mention only the highlights. A comprehensive review would also include a discussion of nucleon-nucleon elastic scattering as well as pion-deuteron interactions. However, these will be mentioned only if there is a direct relevance to the $pp\pi^0$ reaction.

2.1 The Isobar Model

One of the earliest models that was fairly successful in reproducing NN→NNπ data was the semi-phenomenological isobar model proposed by Mandelstam [19]

in 1957. In this model cross sections for pion production were found using an isospin and angular momentum analysis. One of the main assumptions of the model was that all pion production took place via an intermediate NΔ state with the subsequent decay of the Δ to a nucleon and a pion; i.e. :-

$$\begin{aligned} N \;\; N \;\; &\rightarrow \;\; N \;\; \Delta \\ &\hookrightarrow \;\; N \;\; \pi \end{aligned}$$

This theory therefore will not be accurate at about 300 MeV because the NΔ threshold is about 600 MeV, although its effect is felt much lower because of the width of the Δ. The final states were specified according to the relative momentum q of the pion and one of the nucleons, and the momentum p of the other nucleon. The interacting pion and nucleon were then assumed to be in a Δ state and the second nucleon was assumed to be either in an S-state or P-state with respect to the Δ. For the S-state production the only possible transition is the Sp transition ${}^1D_2 \rightarrow {}^3S_1 p_2$ whereas for the P-state production there are five possible contributions. The theory proceeds to calculate the matrix elements for the transitions assuming they are constant with respect to energy. Any variations in the matrix elements are attributed to the final state pion-nucleon and nucleon-nucleon interaction effects. This approach produces six parameters, one for the S-state and five for the P-state production. Further assumptions were made to set some P-state parameters equal to each other, thus reducing the final number of parameters to three. These three parameters were determined by fitting to the experimental results available at that time.

For the reaction $p + p \rightarrow p + p + \pi^0$ the theory predicts a total cross section given by

$$\sigma_T = 40\eta_0^6 + 47\eta_0^8 \;\; \mu b \tag{2.1}$$

where η_0 is the maximum momentum of the π^0 in the centre of mass in units of μc. Here the two terms become equal to one another at an energy of about 400 MeV.

The value of the cross section for neutral pion production was found to depend, to some extent, on the individual parameters which were set equal to one another. The cross section for production in the state with J=1 was less than in those with J=0 or J=2. If all the production proceeded through the state with J=1, the π^0 cross section would be much less than those given by equation 2.2, whereas if all production proceeded through the states with J=0 and J=2, the π^0 cross section would be increased by a factor of about $\frac{3}{2}$.

Predictions have also been made for the angular distribution of the pions. For neutral pions near threshold, the model predicts an angular distribution of $1+cos^2\theta$, corresponding to b=0.33 of equation 1.11, i.e 75% of the pions are isotropically distributed. At higher energies ($\sim$ 660 MeV) predictions are for a more isotropic distribution with b=0.04.

Above 700 -800 MeV this model very probably breaks down because more partial waves are involved and the constancy of the reaction matrix amplitudes cannot be valid for too wide an energy range [32].

2.2 The Coupled Channel Model

A modern developement of the isobar model is the coupled channel calculations of NN scattering by Matsuyama and Lee [33]. This is an extension of the calculations first performed by Green and Niskanen [34] to study the p-wave meson production in $pp \rightarrow \pi^+ d$. The model was constructed by extending the conventional meson exchange theory of NN forces to include the Δ excitation. Two different pion production processes were considered (see figure 2.1):

- a direct Δ production process
- a final state interaction process

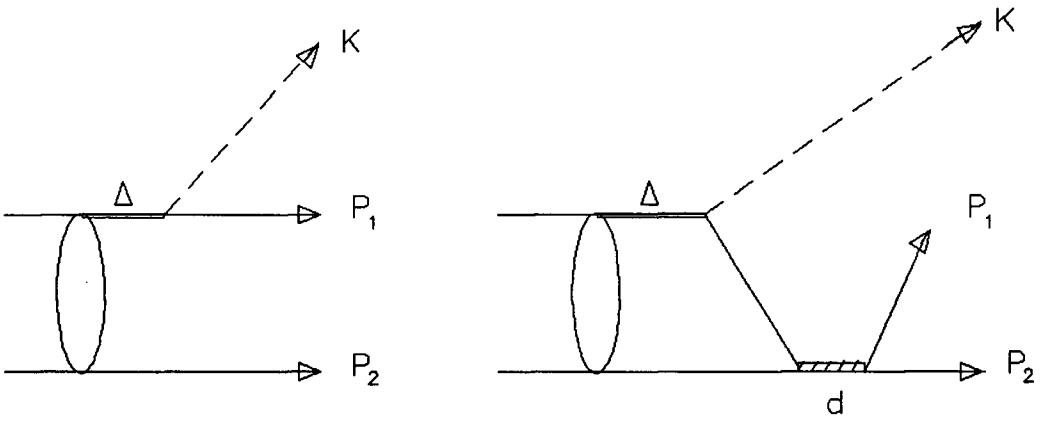

Figure 2.1: The $NN \rightarrow NN\pi$ reaction mechanisms of the coupled channel model of Matsuyama and Lee. (a) The direct production process, and (b) the final state interaction process.

The Hamiltonian for the reaction was written as

$$H = H_0 + V_{NN,NN} + h_{\pi N \leftrightarrow \Delta} + V_{NN \leftrightarrow N\Delta} \tag{2.2}$$

where H_0 is the free energy operator and $V_{NN,NN}$ is a NN potential. The pion production mechanism $NN \rightarrow N\Delta \rightarrow NN\pi$ is due to the last two operators $h_{\pi N}$ and $V_{NN \leftrightarrow N\Delta}$.

Starting from this Hamiltonian they have derived a set of scattering equations which were solved using a numerical procedure. Numerical results have been obtained for the reaction $pp \rightarrow pn\pi^+$ at 800 MeV. For cross sections, the results are only in qualitative agreement with data, and for analysing powers the predictions are further away. The discrepancies between the predictions and data were attributed to the deficiencies of the starting Hamiltonian as well as to the effects

due to the non resonant πN interaction which was neglected in the calculation.

A model employing nucleon, Δ, pion and dibaryon degrees of freedom has been developed by Sauer [35]. It has worked remarkably well for π-d elastic scattering. But, so far unfortunately it has not been extended to study the $NN\pi$ states. Coupled channel calculations have also been done by Niskanen [36,37], Andradi et al. [38], Garcilazo and Mathelistsch [39], and Mizutani et al. [40], but they too have restricted their calculations mainly to the πd channel.

2.3 The Peripheral Model

Peripheral or one pion exchange model (OPEM) calculations assume that a one pion exchange term should be dominant in inelastic processes. The four peripheral diagrams describing single pion production in nucleon nucleon collisions are shown in figure 2.2. In the figure the four momenta of the initial nucleons are denoted by p_1 and p_2 and those of the outgoing pion and the nucleons are denoted by q, q_1 and q_2 respectively. Early progress on this model was reviewed by Amaldi in 1967 [32]. One of the first peripheral calculations for $NN \rightarrow NN\pi$ done by Ferrari and Selleri [41] neglects final state interactions between the nucleons, making it valid only for higher energies ($\sim$ 800 MeV). They restricted their analysis to the isospin one channel and to reaction cross sections.

The matrix elements for the diagrams were calculated in terms of an unknown function $G(\Delta)$ assuming most of the interference terms were negligible. The form of this function was determined by fitting to experimental spectra turning the peripheral model into a semi phenomenological model. Various differential cross sections had been calculated and the predictions of the model seem to be in quite good agreement in the energy region 800 to 1300 MeV. At 600 MeV there are inconsistent comments on the application of the peripheral model to the $pp\pi^0$ reaction. The experiment of Busza et al. [42] claimed good agreement with theory yet the

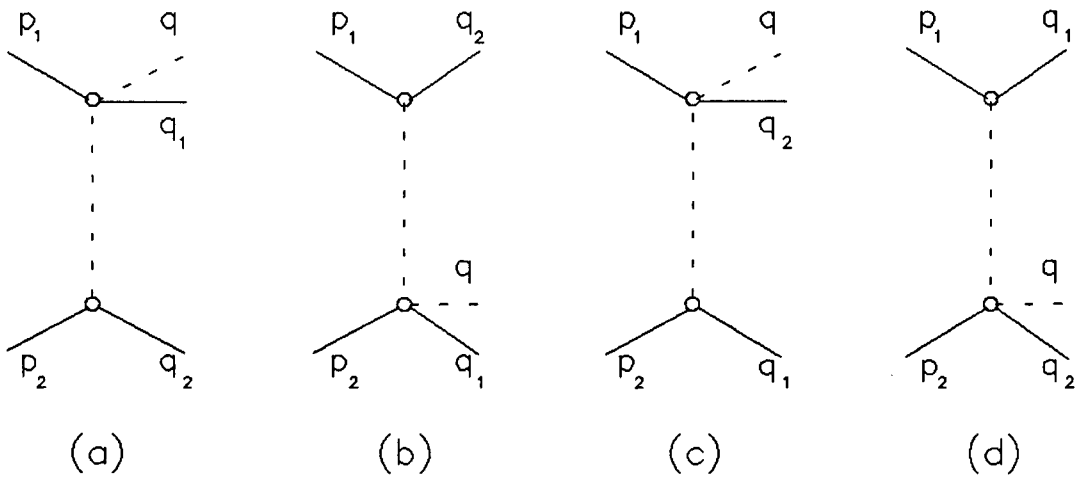

Figure 2.2: Peripheral diagrams describing single pion production in nucleon nucleon collisions.

experiment of Gugelot et al. [43] had discrepancies of a factor three.

A relatively recent peripheral calculation was done by König and Kroll [44] in 1981. They have done a more extensive calculation without restricting it to the I=1 channel. The model contains an exponential form factor with a free parameter λ in order to improve the fit to data. This parameter is fixed by fitting to well measured cross sections for $pp \rightarrow pn\pi^+$. They have been able to obtain a fairly good overall description of the spin averaged observables. For the $pp \rightarrow pp\pi^0$ reaction the shape and the overall magnitude is well reproduced by the model, but at low energies (< 800 MeV) the prediction lies systematically below the data. For the np reaction, where both I=0 and I=1 channels exist, it also predicts cross sections systematically below the data at lower energies. The existence of dibaryon resonances besides the

peripheral interaction has been cited as a possible explanation for this discrepancy. Taking the resonance parameters from elastic NN scattering, they have estimated the contributions of the resonances to the reaction cross sections and found that they have the right strength needed to bring about agreement with data (see Figure 2.3). However other mechanisms can also contribute the missing strength.

VerWest [45] had extended the basic idea of the peripheral model by including the ρ exchange in addition to the π exchange. The calculations were done using two parameters : (a) $\frac{f^2_{\pi N\Delta}}{4\pi}$, the coupling constant for the $\pi N\Delta$ vertex and (b) the momentum cut off Λ of the form factors for πNN and $\pi N\Delta$ vertices. The parameters were fixed by fitting the angular dependence of the data from ref [46] for the reaction $np \rightarrow pX$. This model has been compared with all the available experiments around 800 MeV, and seemed to agree well with all the data. Gruben and VerWest [47] have further studied this model up to 1000 MeV and found that according to this peripheral model

- The dominant contributions for σ_{10} are from the $^1D_2$ channel which reaches its maximum around 700 MeV, and the $^3F_3$ which peaks around 900 - 1000 MeV.

- In the σ_{11} cross section, the $^1D_2$ and $^3F_3$ channels do not play as dominant a role as in σ_{10}, but they still contribute and are responsible for over half of the cross section.

Apparently there is an obvious discrepancy in the ratio of σ_{10} to σ_{11} predicted by this model, compared with the results from the analysis of data [7], which cannot be corrected by adjusting form factors or coupling constants.

Recently Suslenko and Haysak [48] have improved the OPEM calculations by including contributions due to the interference between the diagrams in in figure 2.2. They have calculated triple differential cross sections for the π^+ mesons produced

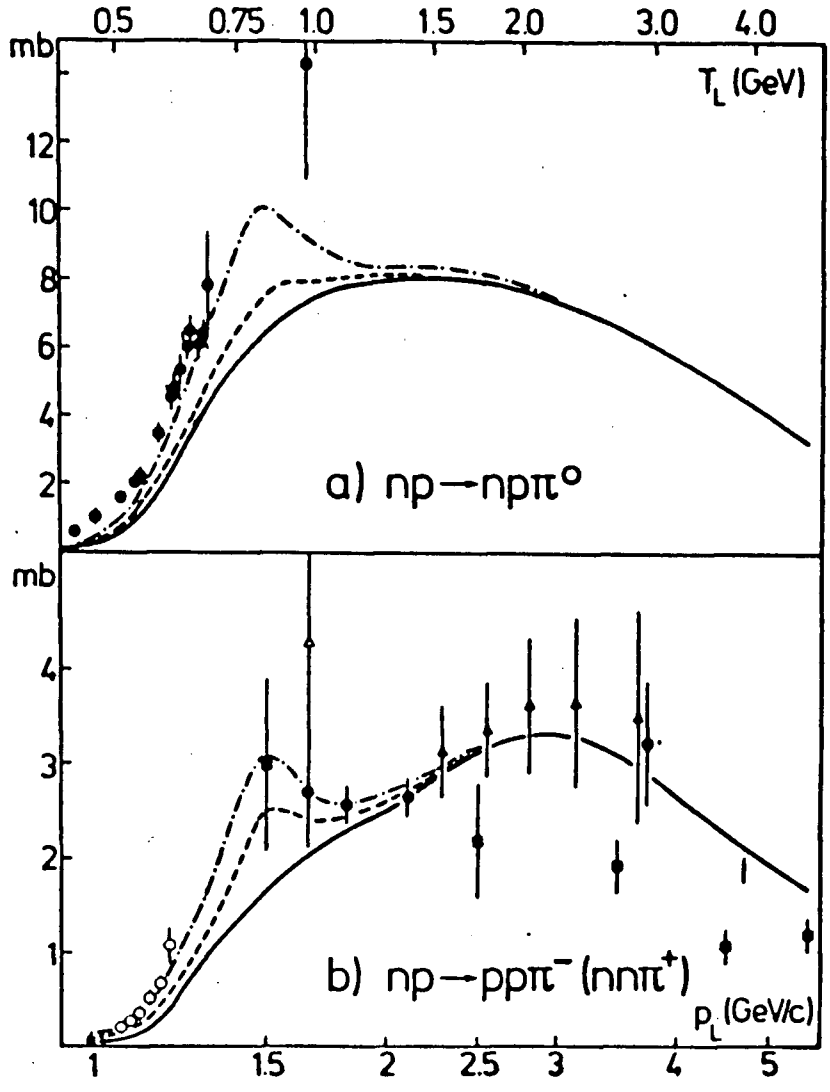

Figure 2.3: The reaction cross sections for (a) $np \to np\pi^0$ and (b) $np \to NN\pi^{\pm}$ versus lab momentum p_L and lab kinetic energy T_L. The solid lines are the peripheral model predictions of König and Kroll. The dashed (dashed-dotted) lines are the suggested contributions from the I=1 dibaryon resonance with mass 2240 (2320) MeV.

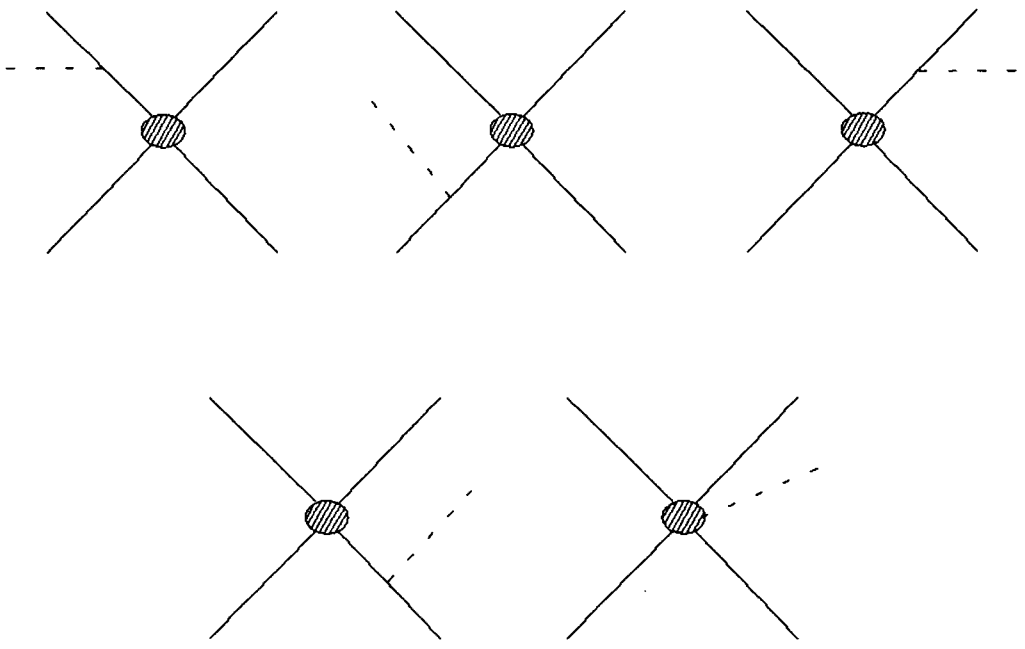

Figure 2.4: Feynman diagrams showing pion emission from external and internal lines.

in the reaction $pp \rightarrow pn\pi^+$ in the energy region 660 to 1000 MeV, in excellent agreement with the experimental data.

2.4 Soft Pion Calculations

In this approach pion emission is considered as the sum of two types of graphs (see Figure 2.4):

(a) an external nucleon line emitting a pion,

and (b) internal emission of a pion.

Since there was no knowledge of the type (b), additional constraints were imposed using the Adler-Dothan theorem [49]. This theorem relates, by the use of PCAC (partially conserved axial vector current hypothesis), the contributions of (b) to

those of (a) in lowest order of pion momentum. This reduces the calculation to calculating trivial Feynman graphs. In his calculations Beder [50] made a number of threshold approximations retaining only terms of order μ/M. Only the dominant pion emission from the initial nucleon lines survived these approximations. For the reaction $pp \rightarrow pp\pi^0$ near threshold, Beder obtained

$$\sigma_T = \left(\frac{g^2_{\pi^0 pp}}{4\pi}\right) \cdot \frac{\mu}{M} \cdot \frac{1}{8\sqrt{2}} \cdot \frac{\varepsilon^2}{M^2} \cdot \left[\overline{\sigma}_{pp} + \frac{\sigma_{pp}}{16}\right] \tag{2.3}$$

with

$$\overline{\sigma} = (\int phase\ space \cdot \sigma_{pp})/(\int phase\ space)$$

$$\varepsilon = \frac{1}{2}[T_{lab} - 2\mu - \frac{\mu}{2M}]$$

The calculations gave cross-sections which were about two or three times larger than the experimental results, but a similar calculation for $pp \rightarrow \pi^+ d$ is within 25% of experimental cross section data. Similar calculations by Baier and Kühnelt [51], but with fewer approximations than Beder, produced results further away from experimental data.

Schillaci et al. [52] had a slightly different approach in their calculations. They started by considering the S-matrix element for the process $\gamma + N_1 + N_2 \rightarrow N_3 + N_4 + \pi$ and obtained the pion production amplitude in terms of the amplitude for production of a pion on two nucleons, plus a correction integral which vanishes in the soft-pion limit (i.e. $T_\pi \rightarrow 0$). Then taking the soft-photon and soft-pion limits in the photoproduction amplitude and using the Adler-Dothan theorem, the pion production amplitude is obtained in terms of off shell nucleon-nucleon scattering amplitudes. The predictions of this calculation are in fairly good agreement with experiment at lower energies. At higher energies the calculations are slightly higher than the experimental results.

Since soft pion techniques are valid only near threshold and at moderate energies the Δ resonance makes a significant contribution, Drechsel and Weber [53]

developed a relativistic treatment for $NN \rightarrow NN\pi$ at low and moderate energies by including soft pion techniques and the Δ resonance of the isobar model. They have given predictions for the $pp \rightarrow pp\pi^0$ reaction in fairly good agreement with experiment.

Hachenberg and Pirner [54] have developed a field theoretical model to calculate the effect of S-wave pion absorption on the pion-nucleus optical potential. Considering S-wave pion production in nucleon-nucleon collisions as the time reversed process to pion absorption on a nucleon pair, they have studied the $pp \rightarrow pp\pi^0$ and $pp \rightarrow \pi^+ d$ reactions near threshold. Their calculations predicted the s-wave parameter B_1 for the $pp \rightarrow pp\pi^0$ reaction as $B_1 = 65\mu b$ [55] which is 3-4 times larger than the experimental results [14]. Recently Efrosinin et al. [56,55] performed s-wave calculations for the above reaction using the same Lagrangian proposed by Hactenberg and Pirner. However in their calculations they have considered the nucleon interaction in the initial and final states as well as the single nucleon mechanism, both of which were neglected by Hachenberg and Pirner. With these considerations the calculations predict an B_1 in the range 11-18 μb, which is slightly lower than the early experiments (but in good agreement with the present experiment).

2.5 The Unitary Model

One of the most complete calculations done so far on the nucleon-nucleon interaction is the unitary model proposed by Kloet and Silbar [57,58]. In this model elastic NN scattering and single pion production are treated in a unified way. The model is a generalisation of the Aaron-Amado-Young (AAY) model [59] applied with good success to pion nucleon interactions at intermediate energies. The coupled $NN \rightarrow NN$ and $NN \rightarrow NN\pi$ amplitudes were calculated using one pion exchange forces. All the spin complications were treated fully, and two and three body unitarity constraints were always satisfied.

The AAY model allows a pion nucleon interaction in the P_{11} and P_{33} partial waves, and their amplitudes are for the processes

$$\pi N \rightarrow \left\{ \begin{array}{c} \pi N' \\ \pi\Delta \end{array} \right\} \rightarrow \left\{ \begin{array}{c} \pi N \\ \pi\pi N \end{array} \right\}$$

where the N' and Δ represent P_{11} and P_{33} interacting πN system. When the invariant mass of N' equals the nucleon mass, N' reduces to the nucleon N. For the $NN \rightarrow NN$ and $NN \rightarrow NN\pi$ reactions, the processes analogous to the above are

$$NN \rightarrow \left\{ \begin{array}{c} NN' \\ N\Delta \end{array} \right\} \rightarrow \left\{ \begin{array}{c} NN \\ NN\pi \end{array} \right\}$$

The pion comes from the breakup of the isobars N' and Δ. This is shown diagramatically in figure 2.5 .

The P_{33} interaction, which is dominated by the Δ resonance, was fitted to the πN phase shifts in this partial wave. The P_{11} interaction was fitted to the nucleon pole and the P_{11} scattering length. Introducing the nucleon pole ensured that the model describes both the $NN \rightarrow NN$ and $NN \rightarrow NN\pi$ amplitudes.

The model was described in terms of the isobar amplitudes $T(NN \rightarrow NN')$ and $T(NN \rightarrow N\Delta)$. The amplitude $T(NN \rightarrow NN')$ with N' evaluated at the nucleon pole i.e. $q^2 = m_N^2$ gives the elastic NN scattering amplitudes. Here q^2 is the square of the four momentum of the isobar. Both isobar amplitudes contribute to pion production for $q^2 > (m_N + m_\pi)^2$. The coupled integral equations for this system were solved exactly by iteration and the use of a Padè approximation technique .

The authors have calculated explicitly a number of spin observables and cross sections for both exclusive and inclusive pion producing NN reactions. For the available exclusive $NN \rightarrow NN\pi$ data the model gives a reasonably good description. For the inclusive reactions the model underpredicts the cross sections at forward proton angles, but predicts fairly well the total elastic cross section. The short comings of this model are thought to be related to the lack of short range forces in

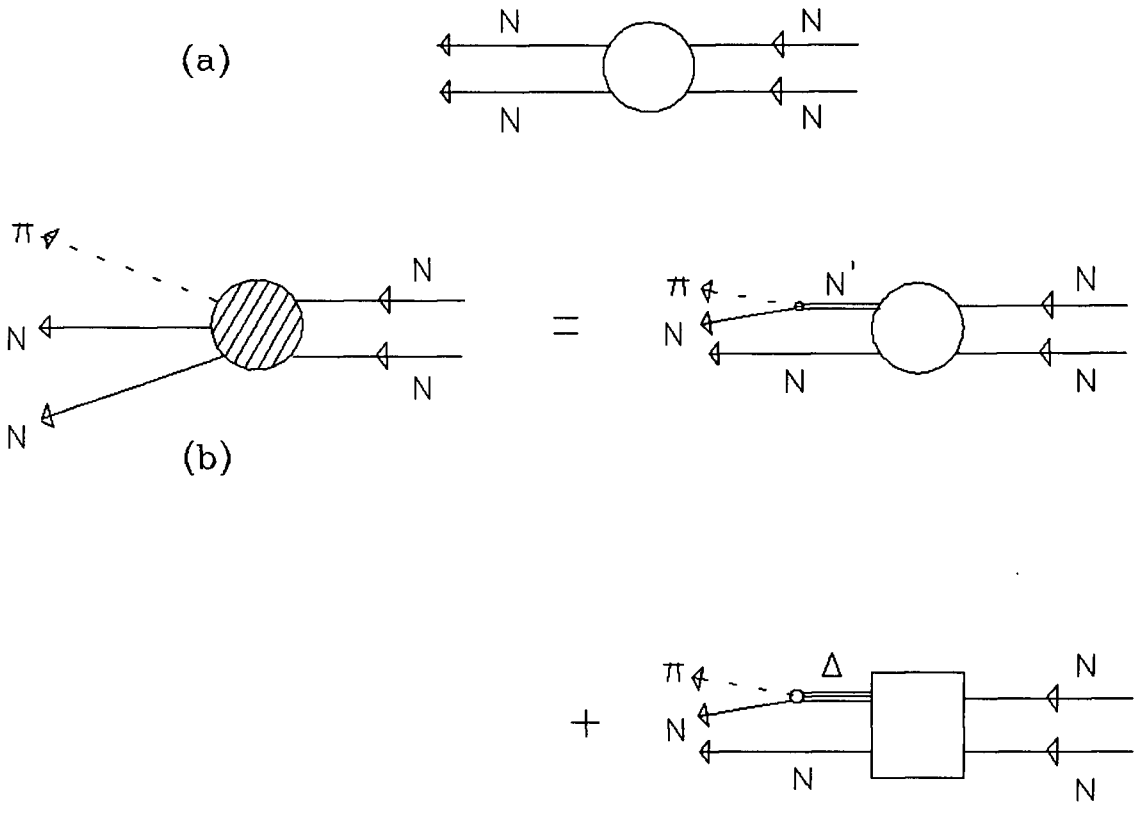

Figure 2.5: (a) elastic scattering and (b) single pion production diagrams used in the unitary model.

the model.

Apart from the above mentioned calculations of Dubach, Kloet and Silbar, there are other unitary calculations reported by Avishai and Mizutani [60,61], Tanabe and Ohta [62] and also by Ueda [63] using a scattering theory of the coupled $\pi NN - NN$ system. Their main concerns were the $\pi d \rightarrow \pi d$, $\pi d \longleftrightarrow NN$ and $NN \rightarrow NN$ reactions. Lee and Matsuyama have extended their coupled channel calculations to form a unitary meson exchange model [64], but they too have restricted their calculations to the πd channel.

2.6 Some Other Conventional Calculations

Koltun and Reitan [65] have done an investigation of the production and absorption of a pion by a free two nucleon system. They have calculated cross sections for the reactions $pp \rightarrow \pi^+ d$ and $pp \rightarrow pp\pi^0$ near threshold where the pion emerges in an s-state. The two nucleon system was treated non-relativistically, with the interaction given by the phenomenological potential of Hamada and Johnston [66]. The pion production processes considered included

(a) direct production by either nucleon

and (b) production by one nucleon and the meson rescattered by the second nucleon.

Their calculations predicted a near threshold total cross section for π^0 production given by

$$\sigma_T = 17\eta_0^2 \quad \mu b \tag{2.4}$$

Yet another near threshold ($\leq$ 300 MeV) non relativistic calculation for the reaction $pp \rightarrow pp\pi^0$ was performed by Zollmann [67] using the distorted wave Born approximations. One motive of these calculations was to determine the "true" nucleon-nucleon potential. For this purpose he proposed an ideal π^0 production experiment and calculated angular and energy distributions using two nucleon potentials Reid soft core, Reid hard core, Hamada-Johnston hard core and Bressel-Kerman-Rouben finite core. His calculations show that near threshold the differential cross sections have a reasonably strong dependence on the nucleon-nucleon potential used in the calculation. Very near threshold Zollmann found that the Reid soft core potential and the Hamada-Johnston potential produced very similar total cross sections, viz

$$\sigma_T = 7\eta_0^2 \quad \mu b \tag{2.5}$$

At 300 MeV, he obtained

$$\text{Reid soft core}: \quad \sigma_T = 8\eta_0^2 \ \ \mu b \tag{2.6}$$

$$\text{Hamada Johnston}: \quad \sigma_T = 10\eta_0^2 \ \ \mu b \tag{2.7}$$

which shows that the simple η_0^2 dependence is not exact.

Another approach has been developed by van Faassen and Tjon [68]. They have used the Bethe-Salpeter equation for coupled N-Δ scattering and extended it to satisfy unitarity. They calculate the phase-shift inelasticities but obtain only mediocre agreement.

2.7 $NN \rightarrow NN\pi$ and Quarks

At intermediate energies, the apparent observation of unusual structures in the measurement of $N-N$ and $\pi-d$ polarising observables has presented a challenge for theories that use conventional degrees of freedom i.e. nucleons and mesons. Since the constituents of nuclei are quarks and gluons whose dynamics are described by quantum chromodynamics, one expects that a traditional description of nuclei in terms of nucleons and mesons should break down at some level. With this in mind Afnan and Blankleider [69] have made an attempt to build a multiple scattering theory for $NN \rightarrow NN\pi$ system by incorporating quark model ideas originating from chiral bag models [70,71] into the unitary model. Using this approach they have been able to include some considerations that have been neglected in the traditional unitary model, but, unfortunately, the resulting equations which they have come up with are very difficult to solve, and no numerical results have been produced at the moment for comparison with experimental data.

Another calculation of $NN \rightarrow NN\pi$ using quarks have been performed by Cao and Hwang [72]. In their calculation they have assumed that the pion emission takes place effectively at the quark level and that quark-quark interactions are

described to a sufficient approximation by one gluon exchange plus effective one pion exchange. The reaction mechanisms were grouped into three categories:

1. A one nucleon mechanism where one pion is emitted from one of the two nucleon clusters

2. A two nucleon mechanism where the pion emission takes place while the two nucleon clusters exchange a virtual pion and

3. Reaction mechanisms involving quark interchange with or without one boson exchange between the two nucleon clusters.

Their numerical predictions for the reaction $pp \rightarrow \pi^+ d$ and $np \rightarrow pp\pi^-$ indicate that, for a nucleon radius of greater than 0.8 fm (as measured in the MIT bag model), reaction mechanisms involving quark interchange are as important as the conventional one-nucleon and two-nucleon reaction mechanisms, even near the pion production threshold.

There are a few other quark model calculations reported in literature. Among them Harvey et al. [73] have shown how the quark potential model through a resonating group formalism leads to a short range interaction between the nucleons of magnitude comparable to that required in boson exchange models to fit the observed phase shifts, but their calculated Δ production cross-sections are far from the experimental results. Faessler et al. [74] have done similar calculations but have restricted their calculations mainly to elastic channels.

2.8 $N - N$ Interaction and Dibaryons

Several attempts have been made to relate the observations of NN scattering to the existence of dibaryon resonances [75]. The remarkable energy dependence

shown by the longitudinal and transverse cross section differences

$$\Delta\sigma_L = \sigma^T(\rightleftarrows) - \sigma^T(\rightrightarrows) \tag{2.8}$$

$$\Delta\sigma_T = \sigma^T(\uparrow\downarrow) - \sigma^T(\uparrow\uparrow) \tag{2.9}$$

in the range $T_P \simeq 400 - 800$ MeV has been the main cause for this enthusiasm. The most conspicuous feature of $\Delta\sigma_L$ is the enhancement centred at $T_P \simeq 570$ MeV with a width of about 110 MeV. All experiments seem to qualitatively confirm this energy dependence. The most prominent features of $\Delta\sigma_T$ are the two enhancements at $T_P \simeq 570$ and 1270 MeV. The first analysis of $\Delta\sigma_L$ data by Hidaka [76] showed that the structure of $\Delta\sigma_L$ is consistent with the existence of a diproton resonance in the ${}^3F_3$ partial wave with a mass of about 2260 MeV. Since then a number of phase shift analyses have been performed which differ among themselves in several respects, but there seems to be reasonable agreement on the existence of strong effects in the ${}^1D_2$ and ${}^3F_3$ partial waves. There is also general agreement that the possible dibaryon resonances must be highly inelastic [75].

As mentioned earlier, the existence of dibaryons have been considered by König and Kroll [44] and Jauch et al. [77] in their calculations of $NN \rightarrow NN\pi$ cross sections. As was shown in figure 2.3, the inclusion of dibaryons significantly improved the predictions of their model, but that is only circumstantial evidence for dibaryons. Dubach et al. [58] have also stated that the explicit addition of dibaryon intermediate states should produce significant improvements in the predictions of their unitary model, but it cannot be considered as a proof of the existence of dibaryons, because alternative mechanisms could explain the discrepancy between the basic theory and experiment. The most widely held opinion at present is that all the observed effects can be explained in terms of threshold effects for the $N\Delta$ channel and that there is no need for specific 6 quark effects [78].

There has also been a continuing search for narrow dibaryon resonances

($\Gamma \leq$ 10-20 MeV) which would signal new and exotic physics. There have been several reported candidates [75] but the majority of the searches have not yielded any evidence for sharp structure. The general consensus is that there is no firmly established narrow resonance.

Chapter 3

Description of The Experiment

The experiment to study the reaction $p+p \rightarrow p+p+\pi^0$ was carried out in two independent runs using the polarised protons provided by the 1B primary beam line (BL1B) at TRIUMF. The first, a preliminary run lasted 3 weeks between August 20th and September 18th 1985. The final data taking was done during the 3 weeks from September 1st to 21st 1986.

3.1 1B Beam Line

The TRIUMF accelerator is a sector focussed cyclotron with six hills and six valleys in the B field. It accelerates negative hydrogen ions because they are very easy to extract from the machine with high efficiency. The beam extraction is done by inserting a thin carbon or aluminium "stripper" foil to strip off two electrons from the H^- ion. In the cyclotron tank a vacuum of 10^{-7} torr is maintained in order to avoid beam losses by gas stripping. The external beam is continuously variable in energy from 180 to 520 MeV. The energy of the extracted beam is varied by changing the radial position of the "stripper" foil. The proton beam is delivered with a 100% macroscopic duty cycle but a 23.055 MHz microscopic structure consisting of a $\sim$ 5 ns pulse every 43 ns.

The layout of the 1B primary proton beam line is shown in Figure 3.1. The experiment was performed at the 1BT1 location. The proton beam was transported from the cyclotron to the experimental area using conventional magnetic elements as shown in the figure. Several remotely insertible, gas filled multiwire proportional

chambers were available along the beam line to check the spatial properties of the beam. At the 1BT1 location, behind the experimental target a beam profile monitor (remotely insertible ZnS scintillating screen) was installed for this experiment. For beam tuning this was inserted to check on the size and shape of the beam spot, which could be monitored on a TV screen in the counting room. The beam spot was circular with a diameter of $\leq$ 1 cm.

3.2 Beam Monitoring

An in-beam polarimeter located upstream of 1BT1 was used during this experiment to measure the beam polarization. Beam current was monitored both by means of the polarimeter and an argon ion chamber located down-stream of 1BT1. For most of the runs, a third monitor, a scintillator telescope was used to check the consistency of the first two monitors. During the experiment the beam current was kept very low, around 20-200 pA depending on the proton energy and the experimental geometry (see later). The polarization was typicaly 40 - 70%, depending on the conditions in the ion source.

3.2.1 The Polarimeter

The proton polarimeter in BL1B is a symmetric four-armed telescope of plastic scintillators viewing p-p elastic scattering using a CH_2 target with an average thickness of 5.36 mg/cm^2. The polarimeter detectors are illustrated in Figure 3.2. Plastic scintillators L1, L2 and R1, R2 are placed at a laboratory angle of 17^0. The corresponding recoil protons are detected by the scintillators L3 and R3. Figure 3.3 shows the coincidence circuit associated with the polarimeter. The events were determined by the triple coincidences L1·L2·L3 and R1·R2·R3 which consist of both real and random events. The accidental contribution to the above was determined by coincidences of the same set of detectors, but with L3 and R3 delayed by 43 ns,

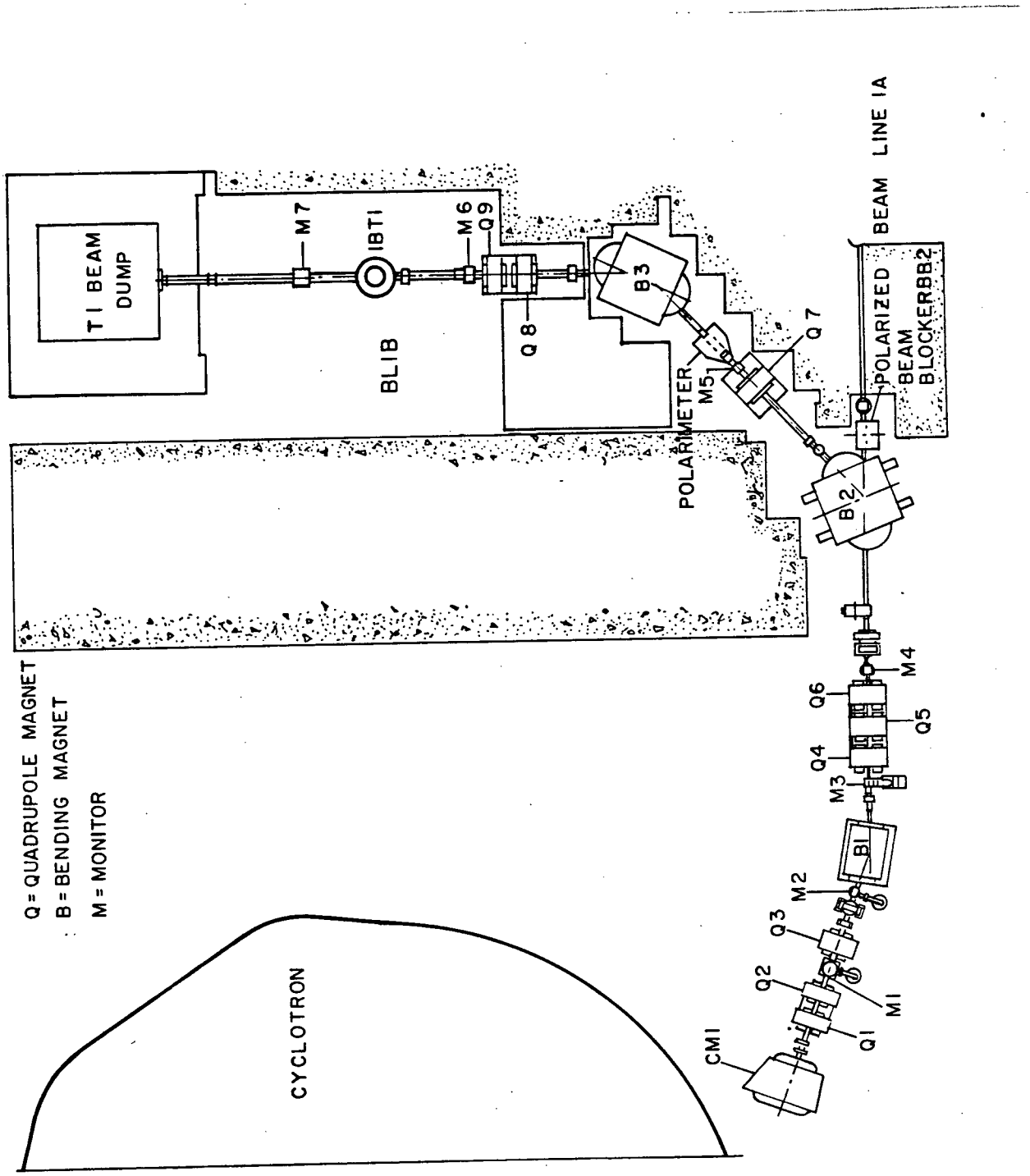

Figure 3.1: Layout of beamline 1B

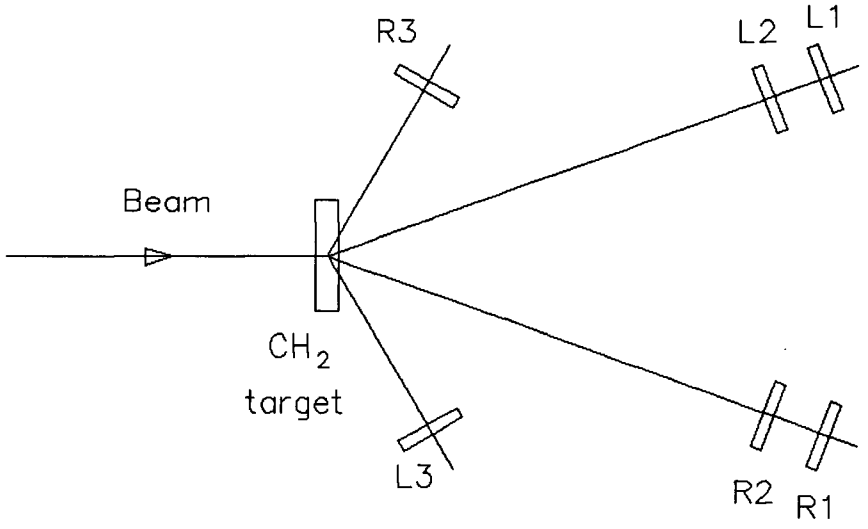

Figure 3.2: Polarimeter set up

the beam burst period. This was to ensure that the accidental protons came from different beam bursts.

The beam polarization is given by

$$\text{beam polarization} = \frac{1}{A}\,\frac{(L - L_{acc}) - (R - R_{acc})}{(L - L_{acc}) + (R - R_{acc})} \tag{3.1}$$

where $L(R)$ - total number of$L1 \cdot L2 \cdot L3$ $(R1 \cdot R2 \cdot R3)$ coincidences

L_{acc} (R_{acc}) - total number of $L1 \cdot L2 \cdot L3_D$ $(R1 \cdot R2 \cdot R3_D)$ coincidences with D = delayed

A - analysing power of the polarimeter

In order to be able to measure the beam current, the polarimeter was calibrated by stopping the beam in a Faraday Cup. The charge collected by the cup was a direct, absolute measure of the number of protons incident upon it. This was done a few months before the final run. The number of protons incident on the target is linearly proportional to the counts in the polarimeter. The relationship

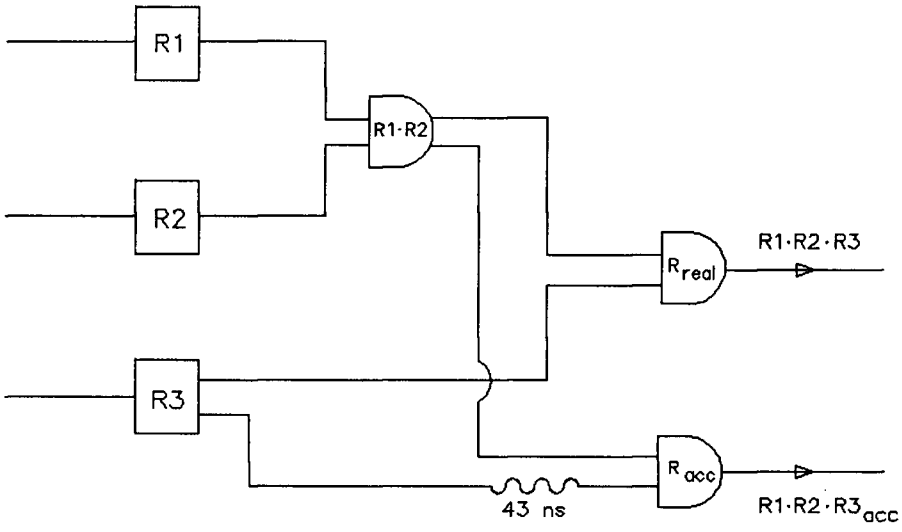

Figure 3.3: Polarimeter electronics

was found to be

$$N_P = \frac{0.625 \times 10^{10}}{K} N_{LR} \tag{3.2}$$

where N_P - number of incident protons

N_{LR} - total number of left and right counts of the polarimeter

K - calibration factor

The results of the calibration (K as a function of proton energy) are shown in Figure 3.4. The calibration was performed for most proton energies of the experiment, but unfortunately the beam was not stable at 320 MeV, hence the calibration for this energy was determined by fitting a line to the other data points. Although a straight line could have described the data adequately, a line shape close to that of *pp* elastic scattering was used as the fitting function.

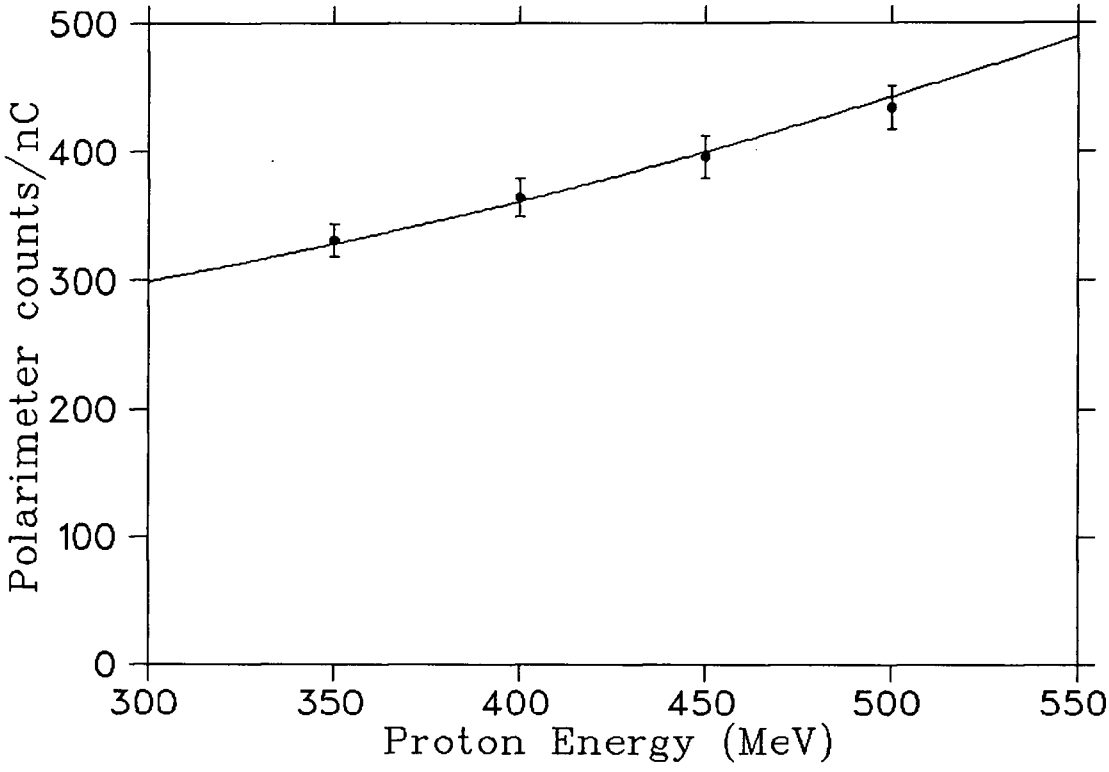

Figure 3.4: Polarimeter calibration

3.2.2 Ion Chamber

The ion chamber used in this experiment contained argon gas. The proton beam, passing through the ion chamber, ionises the gas and the resulting charge is collected by means of high voltage planes. The voltage was maintained at -500 V and the resulting current was measured using a current digitizer. The ion chamber was also calibrated using the Faraday cup along with the polarimeter.

In the energy region of this experiment, the argon ion chamber has a fairly high gain and hence is a better beam intensity monitor than the polarimeter. Unfortunately, we could not properly stabilize the position of the ion chamber throughout the run. Hence the ion chamber had to be reduced to a secondary monitor (along

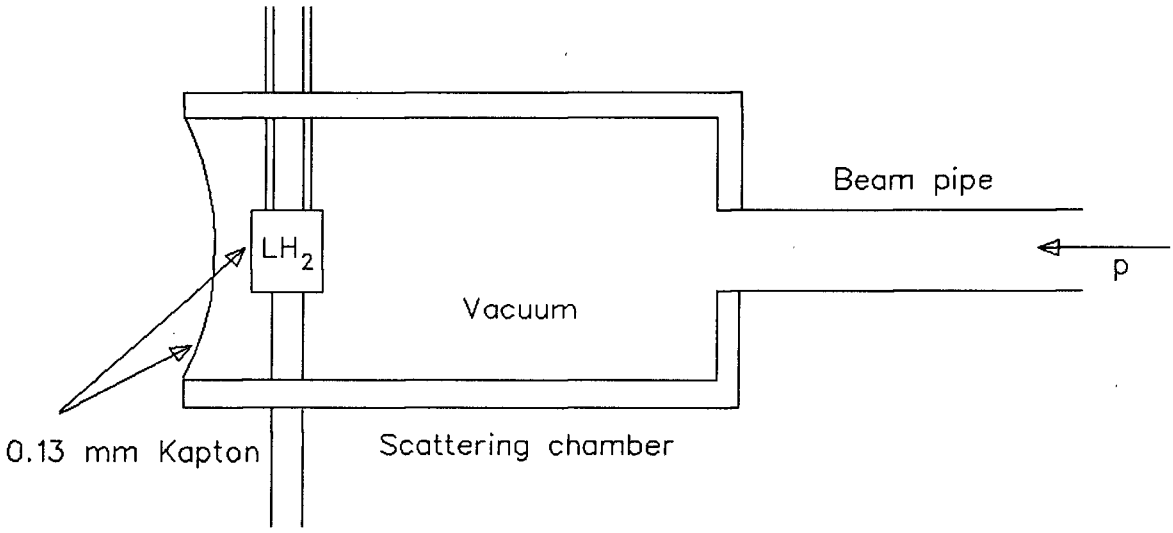

Figure 3.5: Schematic of the liquid hydrogen target

with the beam telescope) and the polarimeter remained the primary beam monitor.

3.3 The Liquid Hydrogen Target

A schematic of the liquid hydrogen target and the scattering chamber is depicted in Figure 3.5. The target flask was cylindrical and measured 5 cm diameter x 5 cm high. These dimensions were selected such that the energy loss of the incident protons in the target be minimal while still giving a reasonable event rate. At 500 MeV, the energy loss to the centre of the target was about one MeV. The walls of the flask were made of 0.13 mm thick Kapton.

The flask was contained in an evacuated scattering chamber. The chamber had a large window made of 0.13 mm thick Kapton. This large window gave the flexibility of detecting γ-rays upto about 150^0 in the laboratory. It was essential that the walls of the flask and the windows of the scattering chamber be very thin

in order to reduce the background π^0s produced by the carbon nuclei in Kapton. In the energy region of interest to us, the π^0production cross section varies from 3 μb at 300 MeV through 15 μ b at 350 MeV to 700 μb at 500 MeV. The π^0cross section on carbon is quite large at these energies (1.7 mb at 340 MeV and 3.7 mb at 437 MeV) so that the thin walls of the flask can contribute a significant amount.

3.4 The π^0 Spectrometer

The π^0 spectrometer used in this experiment consisted of two large NaI crystals TINA and MINA and 2 plastic scintillators (Figure 3.6). TINA, which stands for TRIUMF Iodide of NAtrium, measures 46 cm diameter x 51 cm in length and MINA, which stands for Montreal Iodide of NAtrium measures 36 cm diameter x 36 cm in length. The π^0s were studied by detecting the 2 decay γ rays in the 2 arms of the spectrometer. These deep NaI crystals have effectively 100% efficiency for detecting γ-rays. The 2 plastic scintillators which covered the entire front faces of TINA and MINA, rejected all charged particles. In order to improve the energy resolution of the NaI crystals, TINA and MINA were collimated with 30 cm and 25 cm diameter collimators respectively. The collimators were made of 20 cm thick iron, thick enough to stop scattered protons from reaching the crystals. With these collimators they had energy resolutions of about 8.5% FWHM for 100 MeV γ-rays. Each crystal was viewed by seven 5" "teacup" phototubes type RCA 583006E. The sum of their anode pulses produced a pulse of 60 ns rise time.

In the experiment, TINA and MINA were kept at large distances of about 125 cm from the target, at the expense of solid angle, in order to be able to distinguish between the γ s and the large number of background neutrons, using the time of flight method. The efficiency of detecting π^0s by the spectrometer was determined by the Monte Carlo method.

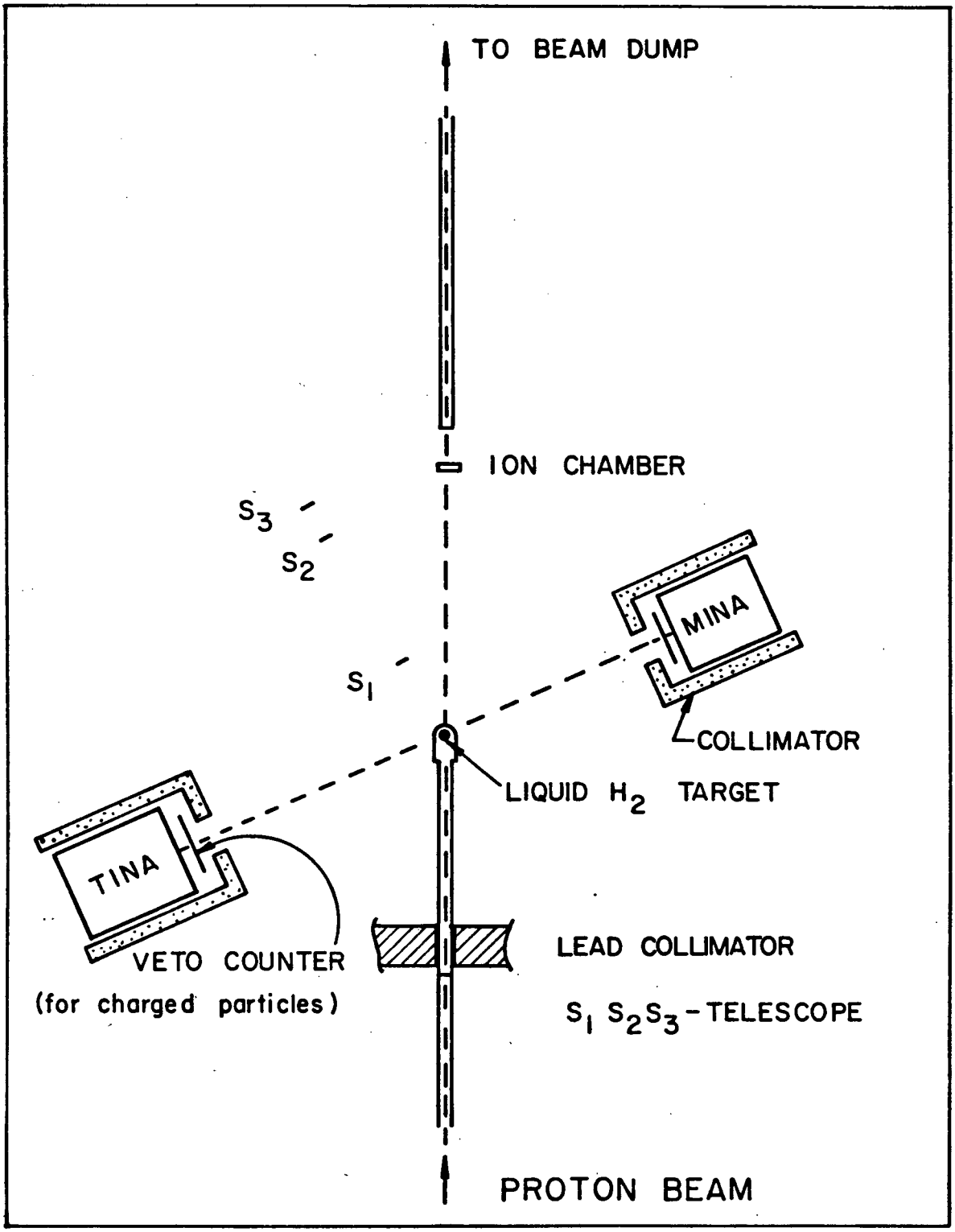

Figure 3.6: Schematic of the experimental set up

At the entrance of the beam into the experimental area, at the end of the beam pipe was a 0.02mm stainless steel window. A 60 cm thick lead wall protected the spectrometer from background neutrons, γ s and π^0s produced at this window.

3.5 The Experimental Method

The main features of the experimental set-up are depicted in figure 3.6. The reaction $p+p \rightarrow p+p+\pi^0$ was studied by bombarding protons on a liquid hydrogen target and detecting in coincidence the 2 γ-rays from the decay of the π^0 in the 2 armed π^0 spectrometer. The timing of the electronics for the coincidence was done using pp elastic scattering. The 2 arms of the spectrometer were kept at 41.5^0 , with both TINA and MINA at equal distances from the target. The angle was fairly precisely defined by a 2.5 cm x 2.5 cm plastic scintillator in front of TINA. At 500 MeV the scattered and the recoil protons would be at these equal angles. Since they also have equal energy (250 MeV) the two protons would arrive at TINA and MINA simultaneously. The energy of these protons were used to estimate the on line calibration of the two detectors. (At high energies there is very little difference between the pulse height for protons and γ-rays of equal energy).

The following information was recorded on tape for each event using a PDP 11/34 computer:

- Pulse heights of individual tubes of of the spectrometer as well as the summed energies of TINA and MINA. The individual pulse heights were later used to balance the phototubes in order to obtain a better energy resolution
- Time of flight of the neutral particles relative to the RF signal of the cyclotron. This was necessary to check the neutron background.
- The polarisation of the incident beam.

Table 3.1: Geometries used in the experiment

Energy (MeV)	Geometry
500	40^0-40^0, 60^0- 60^0, 70^0- 70^0, 80^0- 80^0, 90^0- 90^0 40^0- 140^0, 60^0- 120^0, 80^0- 100^0
450	40^0-40^0, 60^0- 60^0, 90^0- 90^0 40^0- 140^0, 60^0- 120^0, 80^0- 100^0
400	40^0-40^0, 60^0- 60^0, 90^0- 90^0 40^0- 140^0, 60^0- 120^0, 80^0- 100^0
350	90^0-90^0, 80^0- 100^0, 60^0- 120^0
320	90^0-90^0

The experiment was run at proton energies of 320, 350, 403, 450 and 497 MeV. Various combinations of angles were used : several measurements with the detectors at $180^0$to each other (40^0- 140^0, 60^0- 120^0,80^0- 100^0) and others at symmetric angles (40^0- 40^0, 60^0- 60^0, 70^0- 70^0, 80^0- 80^0, 90^0- 90^0), where the two angles refer to the laboratory angles of TINA and MINA respectively. Table 3.1 lists the geometries used for each proton energy. The kinematics of the reaction $pp \rightarrow pp\pi^0$ at 496 MeV are shown in Figure 3.7. The region between the two dotted lines was covered in this investigation. In all 180^0 geometries TINA was always kept at backward angles, mainly to protect it from large fluxes of particles, it being the better and the larger of the 2 crystals. Data was accumulated in short runs and at the end of each full target run, an empty target run was carried out to subtract the background π^0s produced from the walls of the target flask.

The beam current was monitored using the polarimeter upstream, the ion chamber downstream as well as a telescope at 30^0, consisting of 3 plastic scintillators

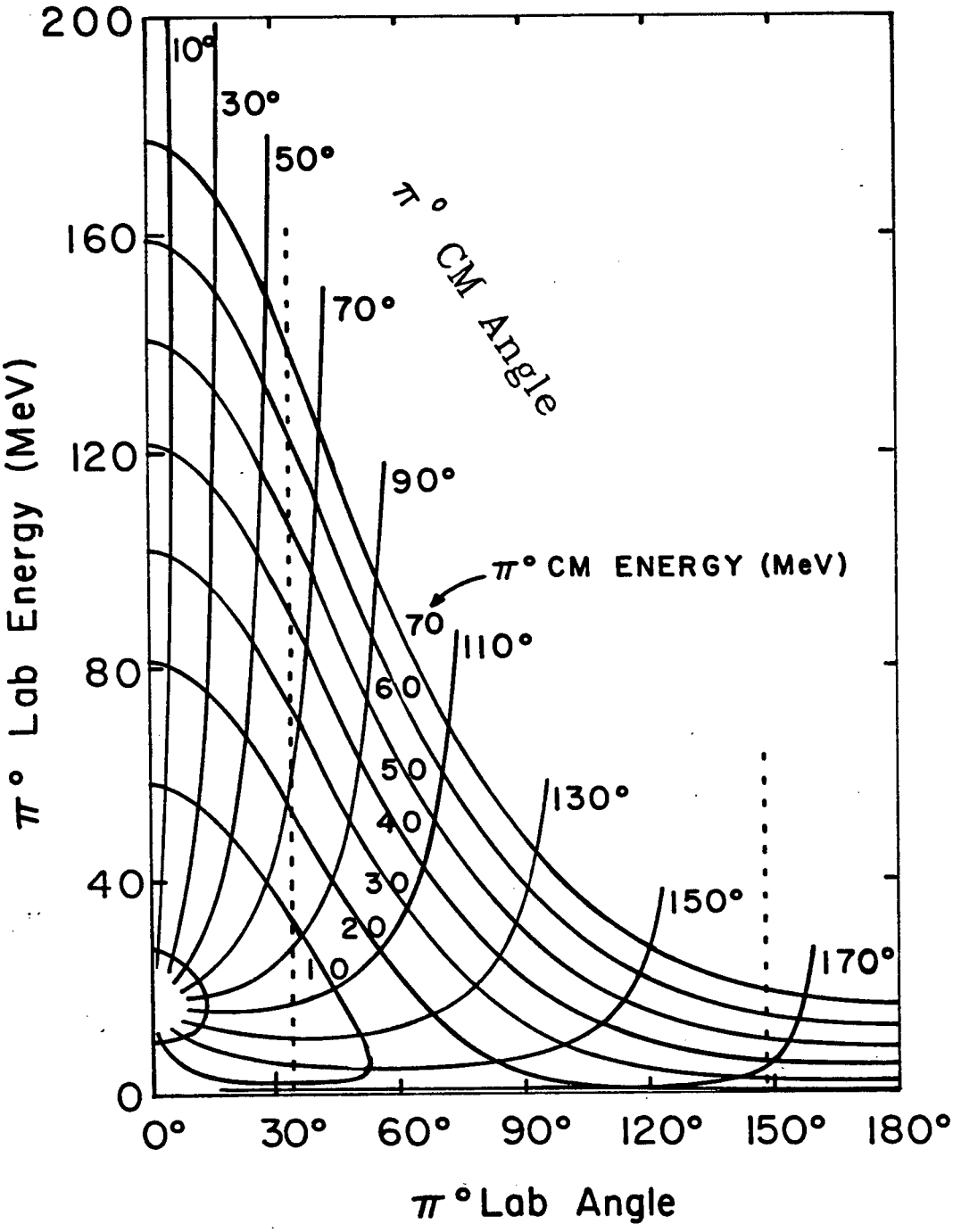

Figure 3.7: Kinematics of the reaction $p + p \rightarrow p + p + \pi^0$ at 496 MeV.

which detected all scattered charged particles (but mainly elastic protons). The beam current for each run depended on the proton energy and the geometry of the spectrometer. The main criteria used to decide on the beam current was the flux of particles on MINA (or on both TINA and MINA at symmetric geometries). This meant that the beam current was increased as MINA was moved to larger angles or as the beam energy was decreased. Typicaly, the current was varied from about 20 pA at 500 MeV, 40^0- 140^0 geometry to about 250 pA at 320 MeV for the 90^0- 90^0 geometry.

3.6 Data Acquisition

Altogether 21 signals were produced by the phototubes attached to the various detectors: 7 signals from each of TINA and MINA, 6 signals from the 3 scintillator telescope counters and the 2 charge vetoes, and one signal from the ion chamber. There were also 6 other signals produced by the polarimeter scintillators (see section 3.2.1). These signals were transmitted to the M9 counting room where the data acquisition electronics and the computer were located. In addition 5 signals were received directly from the master control room; 4 of them refer to the spin of the incident proton (up, down, off, busy) and the fifth is the RF signal.

A schematic diagram of the electronics used in this experiment is shown in Figure 3.8. The data acquisition was done by the task DA which managed the reading of the CAMAC (Computer Automated Measurement and Control) crate, the buffering of events and the writing of the assembled buffers, on magnetic tape. The data acquisition system proceeded in 3 steps:

1. Identification of an event

2. Recording of the data on magnetic tape

3. On line processing of the data.

All TINA (MINA) signals were split into 2 portions (80% and 20% by amplitude) using a passive splitter. The larger portions were amplified $\times 6$ (using a combination of a LRS 612A 10x amplifier and an attenuator) and fed into an Analogue to Digital Converter (ADC). The ADC units used were the LRS CAMAC Model 2259A. This is a high resolution (0.1%), multi-input (12-fold) peak sensing ADC, with a dynamic range of 1024 channels. The seven smaller portions were fed into a mixer, where they were summed to form a single pulse, which was clipped to $\sim$ 250 ns by reflection in a delay cable. This clipped signal was sent to an ADC and to an ORTEC 934 Constant Fraction Discriminator (CFD), both through fast 10x amplifiers. The CFD is a quad discriminator which has a double pulse resolution $<$ 10 ns. It splits the input signal into 2, delays one portion, and subtracts that from a constant fraction of the undelayed signal. The resulting signal has a baseline cross over independent of the input signal amplitude. This zero-crossing line is used to provide a precisely timed logic pulse. If the CFD output is not vetoed by a charge particle signal from the charged veto of TINA (MINA), the arrival of a neutral particle in TINA (MINA) is identified. A coincidence between 2 neutral events in the 2 arms of the spectrometer (TINA $\cdot$ $\overline{TV}$ $\cdot$ MINA $\cdot$ $\overline{MV}$) formed the trigger for a π^0 (neutral) event.

The event definition logic was used to:

- generate a LAM (Look At Me) signal by the CAMAC module to start the PDP 11/34 data acquisition computer cycle.

- open 500 ns gates for the ADC CAMAC modules. The ADCs recorded the amplitude of the NaI anode pulses, as a reading of the kinetic energy deposited in the crystal.

- start the clocks of the LRS 2228A Time to Digital Converter (TDC) CAMAC modules. This is an octal TDC with an 11 bit (2048 channel) resolution. This

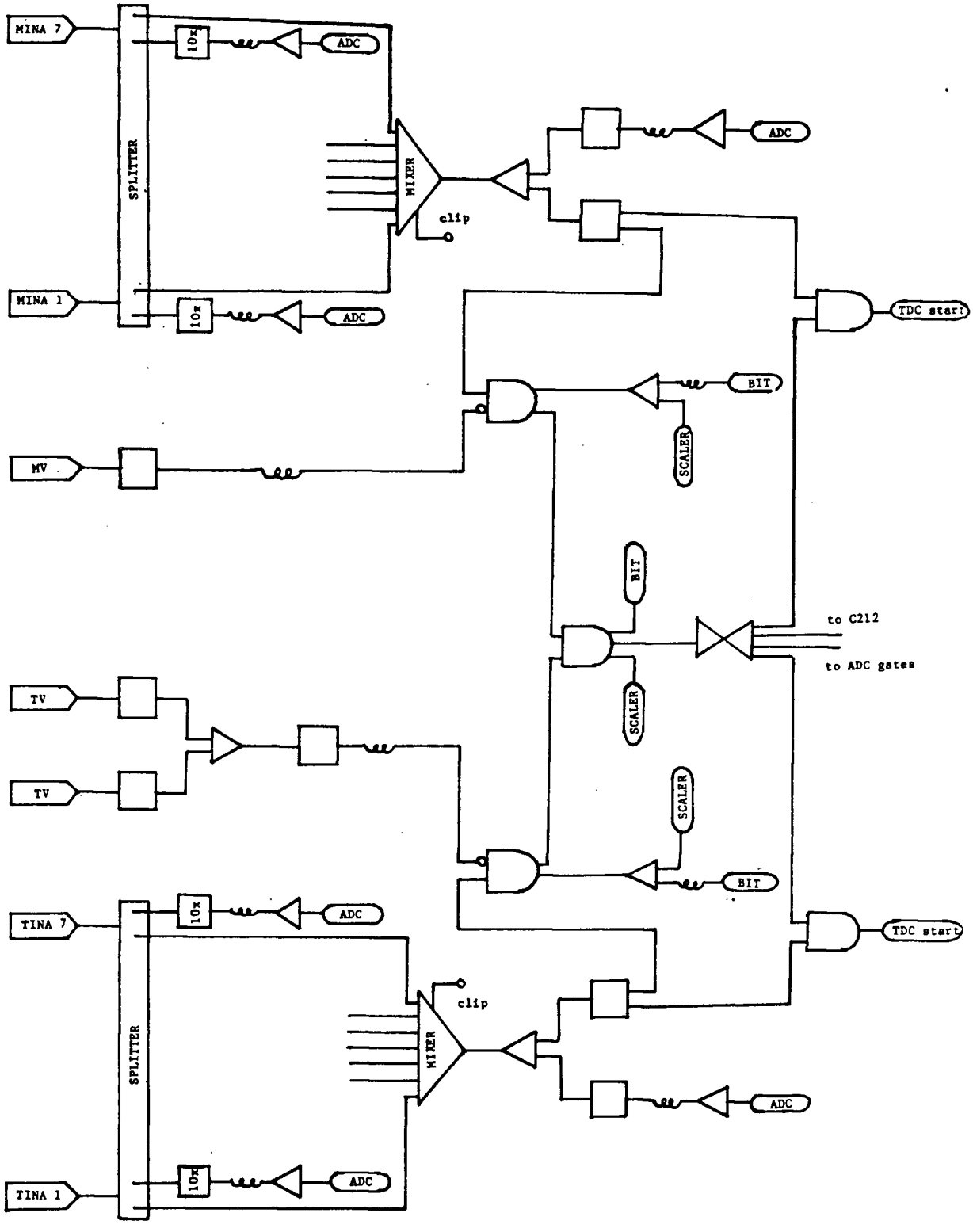

Figure 3.8: Schematic of the Electronic logic

measures the time from the leading edge of the common start pulse to the leading edge of the individual stop pulses. It has 100, 200 and 500 ns full scale time ranges and provides 50, 100 and 250 ps/channel resolution respectively. During the experiment all TDCs were set at the 100 ns range. These clocks were started by the TINA and MINA CFD signals and stopped by the RF signal of the cyclotron. The time measured by the TDCs correspond to the time-of-flight of the neutral particles to TINA and MINA.

- set bits in the C212 coincidence buffer register to record the arrival of neutral particles in TINA and MINA.

- set bits in the LRS 2341A 16 fold logical register to record the spin of the incident proton.

- open a 1 ms gate. This was a protection against subsequent events until the computer starts reading the CAMAC crate. While the crate is being read, a signal from the CAMAC module, NIM Driver provides the inhibit. Once the entire crate has been read, the modules are cleared, the inhibit signal disappears and the system is ready for the next event.

The output of the polarimeter electronics (L, R, (L+R), $(L+R)_{acc}$), and the signals from the ion chamber and the telescope were gated with the spin of the proton, recorded on CAMAC scalers and written on tape. These were later used to obtain the beam polarization, normalise data, etc. In addition to the above, a number of other pulses (eg. neutral events in TINA and MINA, neutral coincidences) were recorded on scalers. Altogether there were 29 different scalers. Some of these were monitored on-line, by visual scalers.

While data were being recorded, the task MULTI [79] was used for on line analysis of data. MULTI is a versatile histogramming package, with access to the

DA buffers. A number of histograms and scatterplots were defined to study the progress of the experiment. MULTI had a lower priority as compared with the task DA. Whenever there was an interrupt from CAMAC, data analysis would be suspended until all the modules had been read.

One of the major problems faced during the experiment was the instability of the RF signal. We used this pulse to determine the arrival time of the protons at our target. However due to cyclotron instabilities, protons are sometimes extracted at a different phase with respect to the RF. At times, the the RF signal shifted phase, suddenly forcing the run to be ended. Very often, this shift pushed the measured time outside the range of the TDC. This was checked using the on line analysis and corrected by suitably adjusting the delays in the TDC stop signal, before starting a new run. Also there were times when 2 bunches of protons appeared at 2 different phases of the same RF cycle. Multi channel analysers were set up both in the counting room and in the master control room to continuously monitor the RF signal. Whenever 2 bunches appeared, the data aquisition was stopped until the cyclotron was adjusted, returning to a single bunch.

3.7 Test Run

The test run carried out in September 1985 had an array of lead glass detectors, instead of MINA, in the forward arm of the π^0 spectrometer. It was thought that most of the neutrons created when protons are bombarded on the target, would swamp the forward arm of the spectrometer if it was a NaI detector. The insensitivity of lead glass detectors to neutrons was the major advantage of using this detector. Also lead glass has a better timing resolution. But these advantages were outweighed by the very poor energy resolution ($\sim$ 30%) of lead glass , and the quality of the data turned out to be quite unsatifactory. The use of NaI instead of lead glass in the final run showed a dramatic improvement in the data.

Chapter 4

Data Analysis and Results

The off-line analysis of the data was performed on the VAX 8600 and VAX 780 computers at TRIUMF. The first step in the analysis was to read the data written on magnetic tape by the task DA and set up the initial histograms and scatterplots. This was done using the TRIUMF software package MOLLI [80] with user written subroutines. The histograms and scatterplots produced by MOLLI were further examined and analysed using the program REPLAY. The analysis of data consisted of the five main phases listed below:

- Selecting π^0 events of interest by removing the background π^0, neutron and random events. This was done by imposing "cuts" on the data and doing background subtractions. Hereafter the word "cut" refers to a condition imposed on the data to select events.
- Determining the energy calibration and resolution of TINA and MINA.
- Determining the efficiency of the π^0 spectrometer.
- Fitting the π^0 energy spectra to obtain the total and differential cross sections.
- Calculating the analysing powers.

The experiment was run at five different incident proton energies. The energies of the protons were slightly less when they had interacted with the target protons because of energy losses in the liquid hydrogen, the wall of the target flask and the

stainless steel window of the beam pipe. These energy losses were minimal, being only about 1 MeV.

4.1 Sources of Background

Since the cross section for the reaction studied was quite low, considerable attention had to be given to possible sources of background. The neutral particles detected by TINA and MINA consist of neutrons and photons. The events that are of interest to us, the π^0 events from the reaction $p + p \rightarrow p + p + \pi^0$, produce 2 photons in coincidence in TINA and MINA. This coincidence condition imposed in hardware during the experiment ensured that the very large background of single neutrons and photons were eliminated. But in addition to the above two photon coincidences, there are other neutral coincidences in the spectrometer, which constitute the background events. These backgrounds arise from:

- γ - γ coincidences from π^0 events produced in the target flask by the following reactions:

  $$p + \text{“}p\text{”} \rightarrow p + p + \pi^0$$

  where the target proton is bound in a nucleus in the target walls or air behind the target.

  $$p + \text{“}n\text{”} \rightarrow p + n + \pi^0$$

  $$p + \text{“}n\text{”} \rightarrow d + \pi^0$$

  where the neutron is bound in any nucleus. Unfortunately the cross-section for these reactions is much larger than for p-p collisions. There are also much rarer reactions such as :-

  $$p + {}^{12}C \rightarrow {}^{13}N + \pi^0$$

  $$p + {}^{12}C \rightarrow {}^{13}C + \pi^+ + \pi^0$$

All these π^0 x mesons are indistinguishable from the "real" neutral pions, and this background can be removed only by subtracting an empty target run from a full target run.

- n - γ events from the reaction

$$p + n \rightarrow p + n + \pi^0$$

where the neutron and a γ from the decay of the π^0 are detected by the spectrometer.

- n - n events from complex nuclear reactions (mainly in carbon)
Most of the neutron related background can be removed by imposing a cut on the time of flight of the neutral particles.

4.1.1 The Time of Flight (TOF) "cut"

Figure 4.1 shows typical TOF spectra of the neutral particles. The photons have a TOF of $\sim$ 4.1 ns from the target to the detectors, whereas the TOF of the neutrons is a function of their kinetic energy, for example a 140 MeV neutron will take twice as long (8.2 ns). The two peaks seen for both neutrons and gammas (instead of one each) in the spectra was a result of vetoing every other RF pulse. This ensures that we see the entire RF spectrum and also gives us a way of calibrating the TDCs. The distance between the two γ (neutron) peaks is the RF period of the cyclotron, 43 ns. Though the calibration was not necessary for the analysis, it was very useful during the experiment to determine the delays necessary in centreing the RF spectrum, whenever there was a change in the RF phase.

Figure 4.1(a) corresponds to the 180^0 geometry with both TINA and MINA at 90^0, and in Figure 4.1(b) both detectors were at forward angles. Since most of the background neutrons, tend to travel forward in the laboratory, it can be clearly

seen that the rate of neutron related events increase as the arms of the spectrometer are moved to forward angles.

A "cut" was imposed from the RF spectra to reject the neutron events and select only the γ related events. This was done by setting windows on the time of flight of γ events. In order to improve the efficiency of the "cuts", a function was fitted to all the RF spectra using the CERN function minimisation program MINUIT [81]. The fitting function consisted of gaussian terms for the γ peaks and an asymmetric function for the neutron peaks. The function had the form:

$$f(t) = A_1 exp\left(\frac{t-B_1}{C_1}\right) \cdot \left[1 - erf\left(\frac{t-E_1}{D_1}\right)\right] + A_2 exp\left[-0.5\left(\frac{t-B_2}{C_2}\right)^2\right]$$
$$+A_1 exp\left(\frac{t-B_1-T}{C_1}\right) \cdot \left[1 - erf\left(\frac{t-E_1-T}{D_1}\right)\right]$$
$$+ A_2 exp\left[-0.5\left(\frac{t-B_2-T}{C_2}\right)^2\right] + F \qquad (4.1)$$

where A_1, B_1, C_1, D_1, E_1, A_2, B_2, C_2, F and T are parameters. The parameter T refers to the period of the RF signal. This function fitted the RF spectra very well.

There were two types of TOF cuts in the analysis, one to extract the total and differential cross sections and the other for the analysing powers. For the cross section it was essential that no π^0 events be lost due to the cut. A $\pm\ 3\sigma$ (where $\sigma = C_2$ is the standard deviation) window on the γ peaks selected all γ related events. For a few runs, where the RF was a bit unstable the window had to be increased slightly so as not to lose any π^0 events. The efficiency of the RF cut was always above 95%level. The inefficiencies were caused by the time walk of the RF signal. Suitable corrections were made to account for this (see section 4.1.2). As seen in Figure 4.1(b), the high energy tail of the neutron peak overlaps a fair amount with the γ peak. This is mostly true for the forward symmetric geometries. Since the polarization of these overlap neutron events could influence the analysing

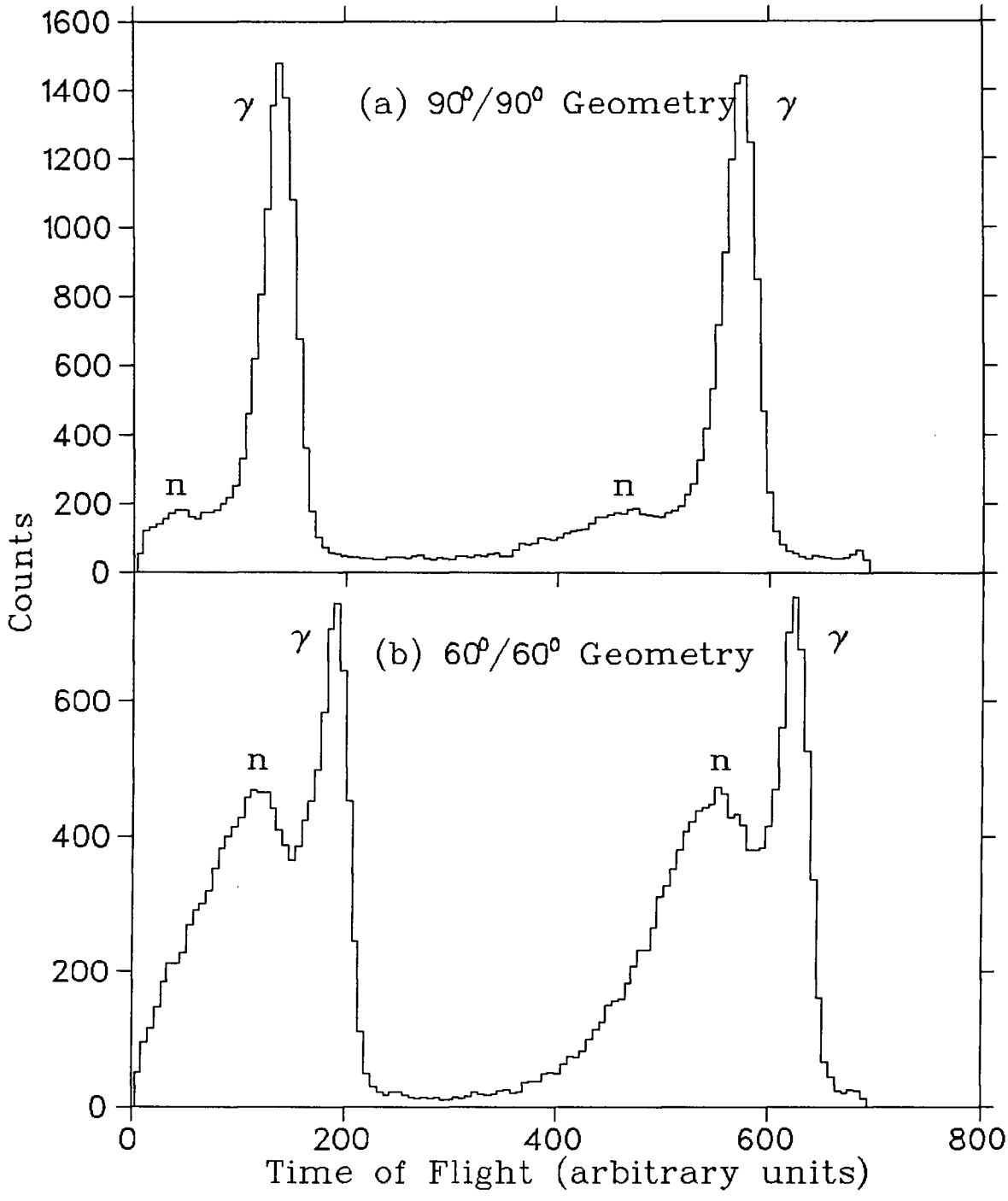

Figure 4.1: Time of flight of neutral particles to TINA for (a) 180^0 geometry and (b) forward symmetric geometry.

powers, a narrower window ($\pm$ 2σ) was placed on the γ peaks when selecting the π^0 events for the analysing powers.

4.1.2 The π^0 Mass Cut

When a π^0 decays into two photons of energy E_1 and E_2, from kinematics it can be shown that

$$E_1 \cdot E_2 = \frac{m^2_{\pi^0}}{4 \cdot sin^2 \frac{\psi}{2}} \tag{4.2}$$

where ψ is the opening angle between the two γ rays. This is very important as it means that $E_1 \cdot E_2$ is independent of the π^0 energy.

For a given geometry of the π^0 spectrometer (ψ = constant) this represents a hyperbola. With most of the neutrons removed using the TOF cut, a two dimensional plot of energy deposited in MINA against energy deposited in TINA (Figure 4.2) shows a very clear band due to the π^0 production. These pions show up as a peak in a spectrum of $E_T \cdot E_M$ (Figure 4.3(a)). The width of the π^0 band depends on the energy and the angular resolutions of TINA and MINA. The position of the band depends on the mass of π^0 and the angle between the two detectors. The background seen in Figure 4.2 and the low energy tail of Figure 4.3(a) correspond to the background events underneath the γ peaks of Figure 4.1.

The efficiency of the TOF cut was checked by looking at the complementary plot of Figure 4.3(a), i.e. by looking at the events discarded by the TOF cut. This is shown in Figure 4.3(b). In a few runs a small peak showed up in the position of the π^0 mass, showing evidence of a time walk of the RF signal. For these runs the TOF cut was slightly loosened until this secondary peak was below the 5% level. This was done only for the cross section analysis.

In order to impose a cut on the π^0 mass to remove the random background, a

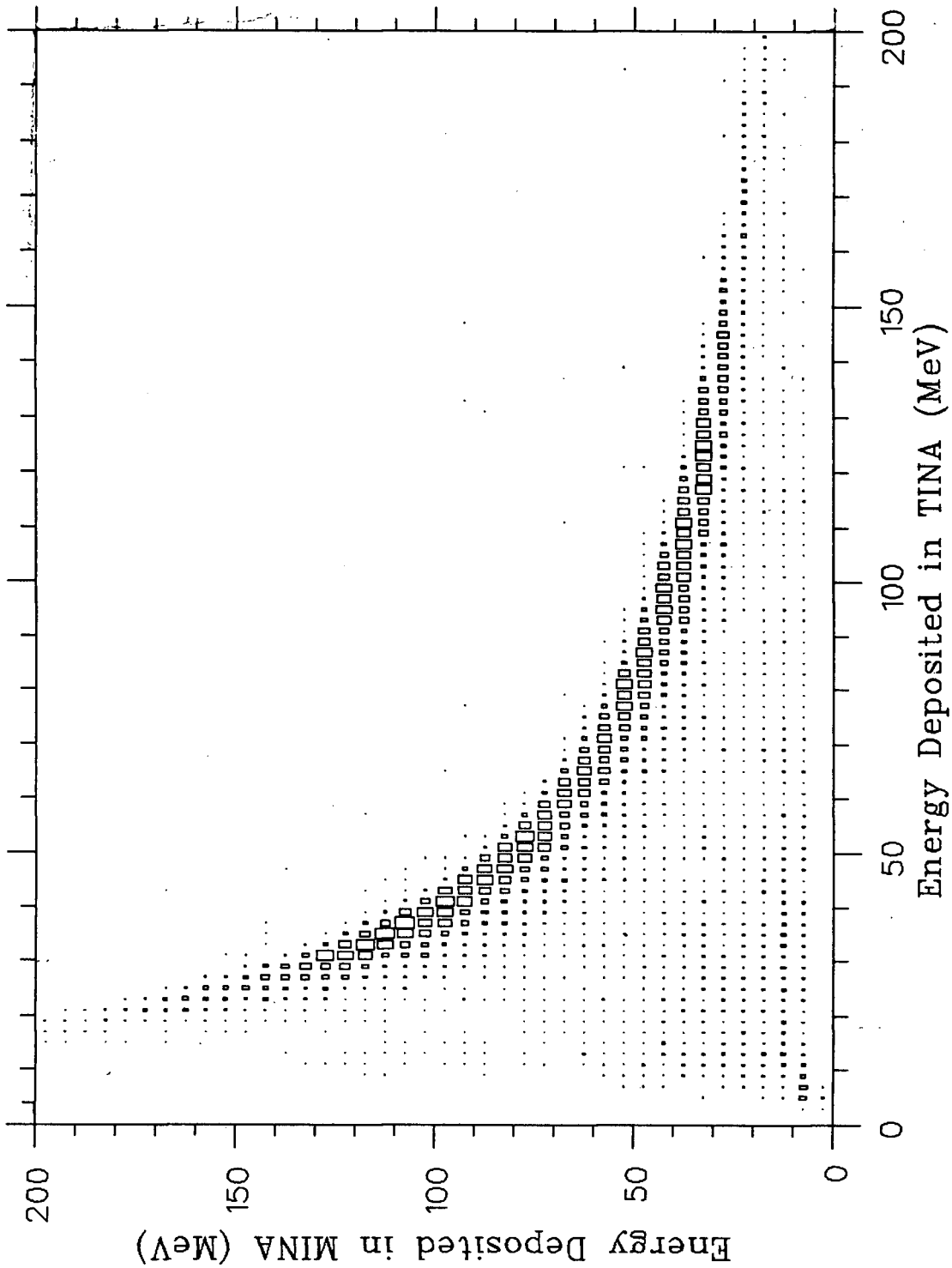

Figure 4.2: Two dimensional plot of energy deposited in MINA against energy deposited in TINA. The clear band corresponds to π^0 production

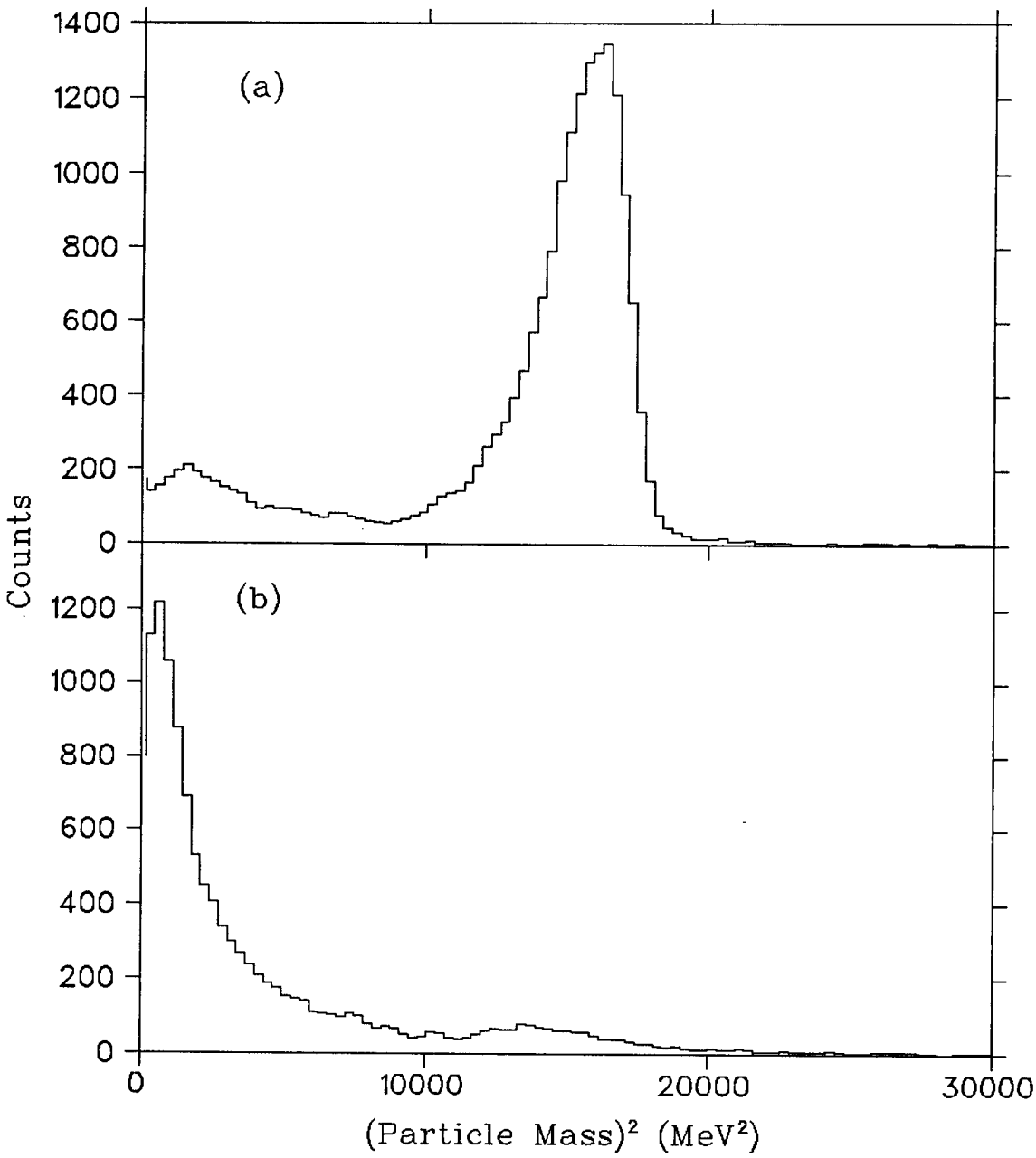

Figure 4.3: The spectrum of ETINA.EMINA (a) for events inside the TOF window. The peak corresponds to π^0 production. (b) for events outside the TOF widow

function was fitted to the mass spectra using MINUIT. The function used was

$$f(x) = A \cdot exp\left[\left(\frac{x-B}{C}\right)\right] \cdot \left[1 - erf\left(\frac{x-B}{D}\right)\right] + F \cdot exp[-(x+H)^G] \qquad (4.3)$$

where the first term fitted the π^0 peak and the second is a background term. A window was set on the mass spectra to separate the π^0 events from the background events. This window had a lower limit at the point of intersection between the background and the low energy tail of the peak. The upper limit was a similar point in the high energy tail or at the point where the number of counts reached one, whichever came first. This window effectively removed all the background events. The background underneath the π^0 mass peak was estimated to be less than 2%.

In the analysis of the cross section data, the number of pions lost due to the TOF cut was estimated by fitting a function to the complementary mass spectra. This function had the same form as the one used to fit the mass spectra. These estimates, were later used to correct the π^0 energy spectra.

4.1.3 Empty Target Subtraction

The two cuts mentioned above ensure that the backgrounds related to the n-γ, n-n events and random coincidences are removed. These leave behind the much larger background of neutral pions from substances other than the liquid hydrogen of the target. At each geometry of the spectrometer several runs were recorded with the target full and target empty. Here the target full refers to the target flask filled with liquid hydrogen. When the target was empty it contained hydrogen gas at one atmosphere. In the analysis, after applying the first two cuts, normalised empty target runs were subtracted from the corresponding full target runs. This ensured the removal of this π^0 background, and produced the final spectra to be used later for fitting and other calculations. Typical background subtracted γ-ray

energy spectra are shown in Figure 4.4.

4.2 Energy Calibration

For pion beam experiments at TRIUMF the normal practice in calibrating TINA and MINA as photon detectors is to stop a π^- beam in H_2 or LiH and to use the energy of the monoenergetic γ-ray from from the radiative capture reaction $\pi^- + p \rightarrow n + \gamma$ and the edges of the "π^0 box" from the charge exchange reaction $\pi^- + p \rightarrow \pi^0 + n$. Unfortunately these γ-rays were not available in this experiment, but as it turned out, no such calibration runs were necessary as the experiment was self calibrating. The maximum energy of the photons produced by the decay of the π^0 from $p + p \rightarrow p + p + \pi^0$, at each position of TINA and MINA were used in the calibration.

When protons with a Lorentz factor γ, are scattered on hydrogen, the maximum laboratory energy of the π^0 mesons created is given by [82]

$$E_{\pi^0}(\theta) = \gamma^{CM} \cdot (E_{\pi^0}^{CM} + \beta_p^{CM} \cdot P_{\pi^0}^{CM} \cdot cos\theta^{CM}) \tag{4.4}$$

where

- $$E_{\pi^0}^{CM} = \frac{(m_{\pi 0}^2/m_p) + 2(\gamma - 1) \cdot m_p}{2\sqrt{2(1+\gamma)}}$$

  is the maximum π^0 energy in the centre of mass.

- $$\gamma^{CM} = \frac{\sqrt{\gamma + 1}}{2}$$

- $P_{\pi^0}^{CM}$ is the maximum momentum of the π^0 in the centre of mass.

- β and m represent the velocity and mass of the particle referred to in the subscript.

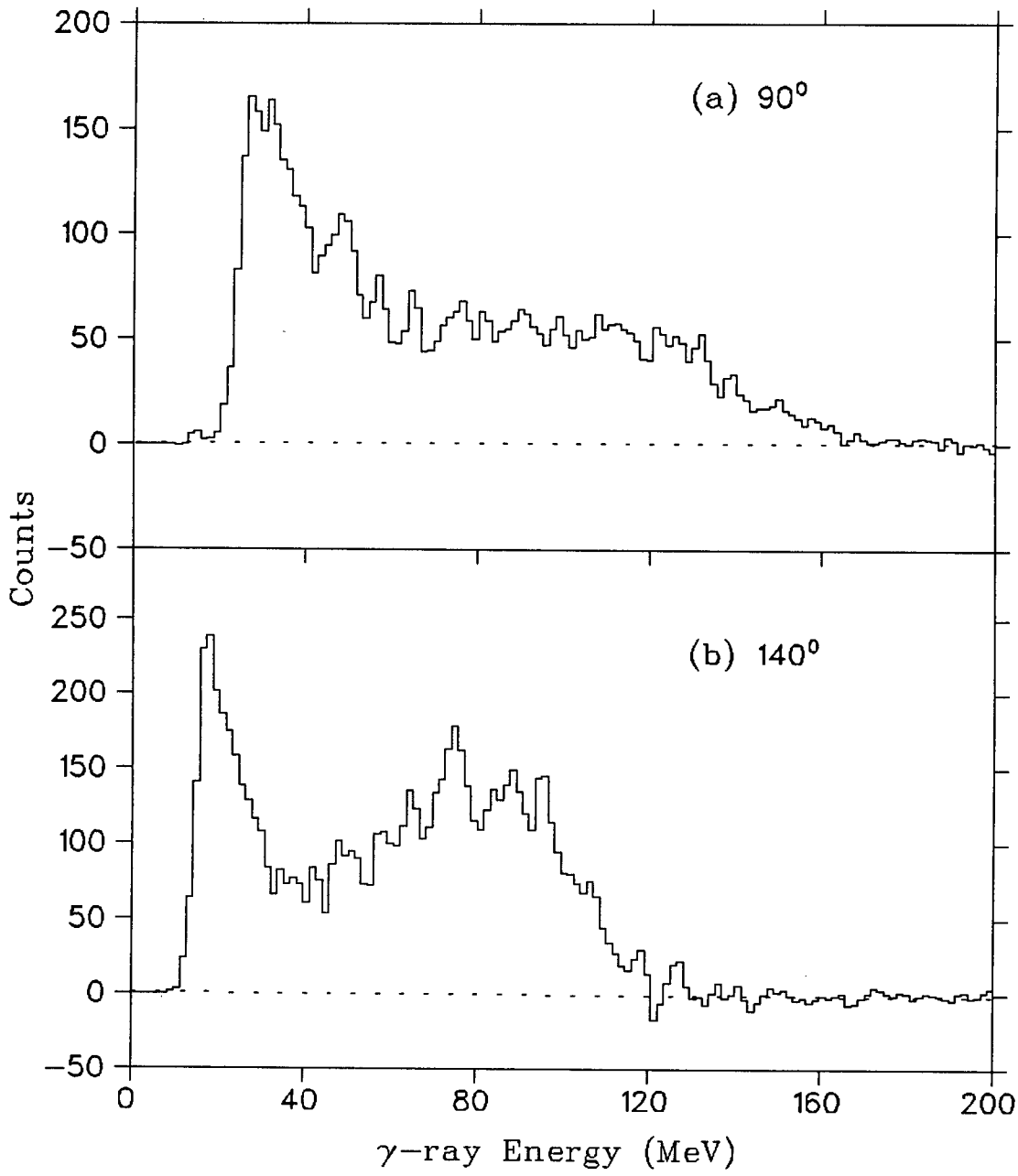

Figure 4.4: γ-ray energy spectra in TINA from the decay of π^0 mesons at (a) $90^0$and (b) 140^0. Incident proton energy is 496 MeV

The laboratory and centre of mass angles of the π^0 are related by

$$tan\theta = \frac{sin\theta^{CM}}{\gamma^{CM} \cdot \left(cos\theta^{CM} + \frac{\beta_p^{CM}}{\beta_{\pi^0}^{CM}} \right)} \tag{4.5}$$

These maximum energy pions when decaying at 180^0, provide the maximum energy photons observed in the laboratory. The maximum energy of photons in the laboratory is calculated from

$$E_\gamma^{max} = \frac{m_{\pi^0}}{2} \cdot \left[\gamma_{\pi^0} + \sqrt{\gamma_{\pi^0}^2 - 1} \right] \tag{4.6}$$

Table 4.1 shows the maximum energy of the pions and photons for each of the angles in this experiment. Only the 180^0 geometry was used for the calibration as it defines the direction of the π^0 fairly precisely. The cut-off points of the experimental spectra were determined by fitting a function to the high energy part of the γ spectra.

In addition to the above, information from pp elastic scattering was also used for additional calibrations. At low energies (< 20 MeV) the light produced in a NaI from a proton is less than the equivalent energy from an electron or γ-ray. At higher energies the difference is minimal however. Since the angles of TINA and MINA were well defined, so were the full energy elastic peaks of the scattered protons. Straight line fits were performed to determine the energy calibration parameter K defined by

$$E = K \cdot (V_{ADC} - pds) \tag{4.7}$$

where

- E is the value of the energy recorded by the ADC.
- V_{ADC} is the digitised value produced by the ADC.
- pds is the pedestal in the ADC.

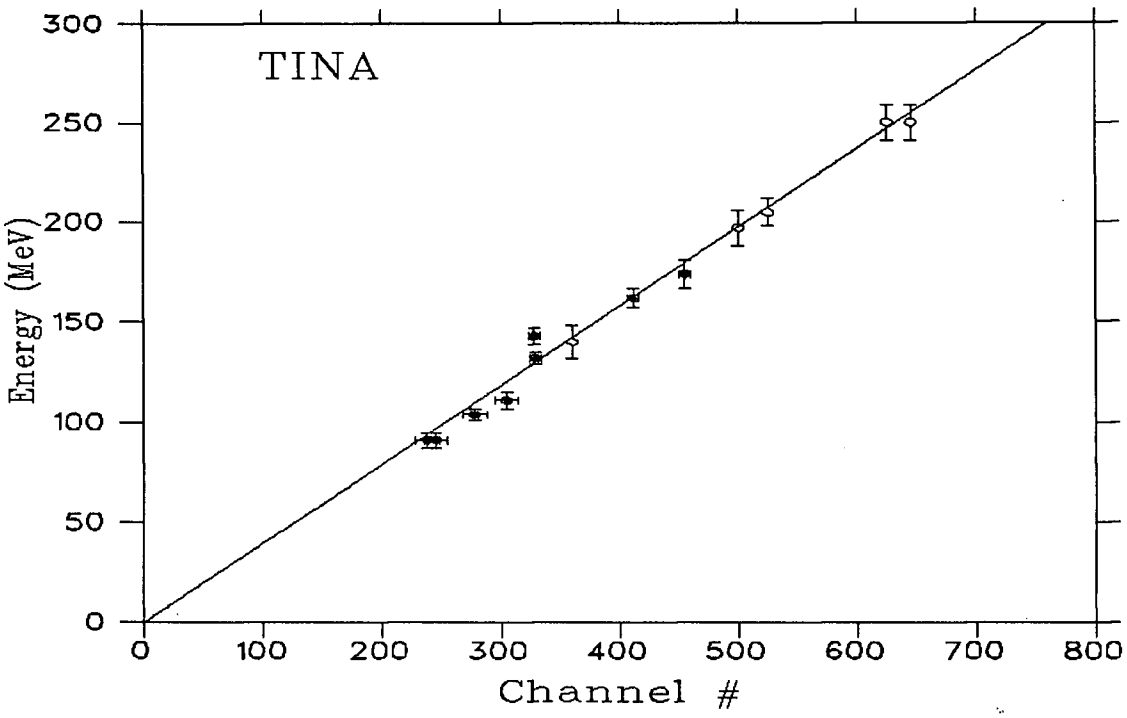

Figure 4.5: Energy calibration of TINA. Closed circles are from γ-spectra and the open circles are from proton scattering.

It was noticed that the gains of the phototubes had shifted slightly during the second half of the run. Hence two sets of calibrations were obtained for the 2 parts of the run. Figures 4.5 and 4.6 show the TINA and MINA calibration for the first part of the run. As seen in the figures even within each set slight gain shifts in the phototubes occurred. This was caused mainly by the large fluxes of charged particles. Suitable corrections were made during the fitting of data to account for this.

4.3 Energy Resolution and Response Function

Although when a monoenergetic γ-ray deposits its energy in a large NaI crystal, one would theoretically expect to see a very sharp line, the measured response functions contain the "blurring" effects due to the finite energy resolution of the

Table 4.1: Maximum laboratory energies of π^0 mesons and photons.

Proton Energy (MeV)	Lab Angle	Maximum π^0 Energy (MeV)	Maximum γ Energy (MeV)
500	40^0	157.4	275.9
	60^0	114.4	229.5
	90^0	66.3	175.2
	120^0	40.5	143.8
	140^0	31.8	132.4
450	40^0	125.5	241.6
	60^0	90.0	202.5
	90^0	50.4	156.2
	120^0	29.7	129.5
	140^0	22.9	119.8
400	40^0	92.8	205.6
	60^0	64.8	173.5
	90^0	33.9	135.2
	120^0	18.6	113.4
	140^0	13.8	105.7
350	60^0	38.1	140.7
	90^0	16.6	110.3
	120^0	7.6	94.1
320	90^0	5.9	90.6

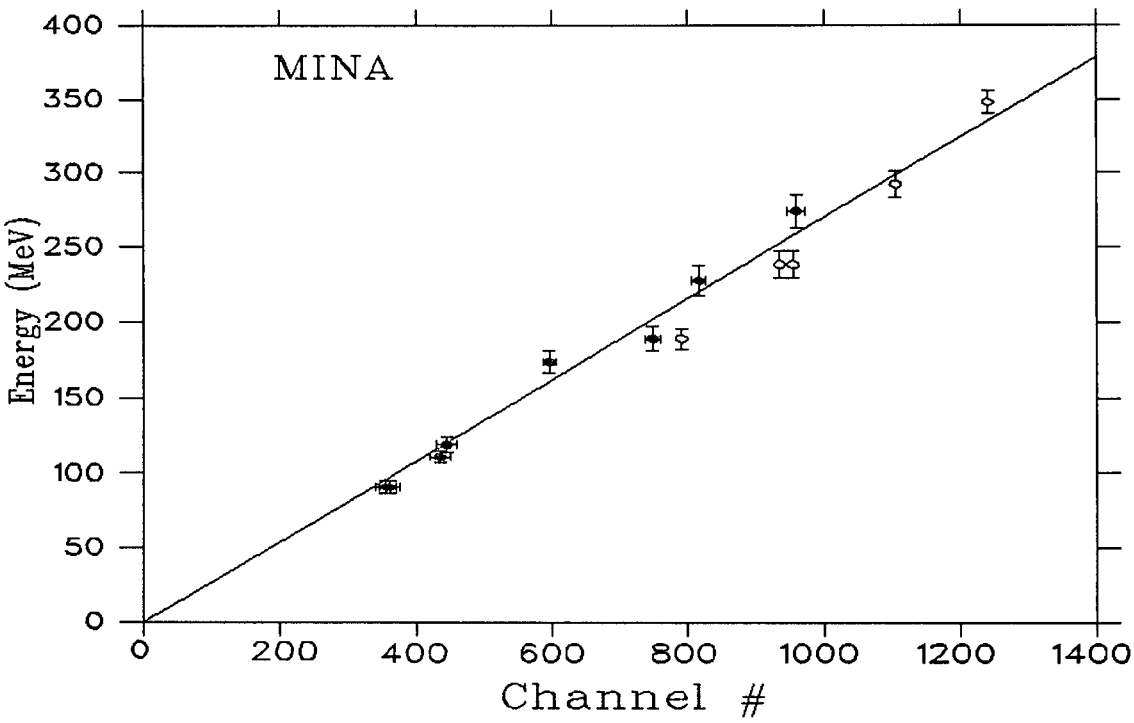

Figure 4.6: Energy calibration of MINA. Closed circles are from γ-spectra and the open circles are from proton scattering.

detector. Among other things, the resolution of the detector contains contributions due to variations in the detector response over its active volume, escape of the electron and γ-ray shower from the crystal due to its finite volume, and electronic noise and drifts in operating parameters of the phototubes during the measurement.

The response of TINA and MINA to a mono-energetic γ-ray can be fairly well described by the empirical function [83]

$$P(E_\gamma, A, B, C, D) = A \cdot exp\left(\frac{E_\gamma - B}{D}\right) \cdot \left[1 - erf\left(\frac{E_\gamma - B}{C}\right)\right] \qquad (4.8)$$

where A is the amplitude, B is the peak position and C and D are the half widths related to high and low energy tails of the full energy peak respectively.

The parameters C and D which determine the energy resolution, are energy dependent. Their energy dependence was determined from Monte Carlo simulations using the EGS code [84]. This code was used to obtain the theoretical energy

spectrum of mono-energetic photons incident on the detector. To account for any non-uniformities in the detector, the theoretical spectrum was folded using a gaussian smoothing function. This gave the "experimental" spectrum of the incident mono-energetic photons. The empirical function 4.7 was fitted to the "experimental" spectrum to determine the values of C and D. This was repeated for a number of energies and the function $C[D] = aE^b$ was fitted to the resulting values of C [D]. The energy dependence was obtained as

$$C = C_0 \cdot E_\gamma^{0.8} \quad \text{and} \quad D = D_0 \cdot E_\gamma^{0.6}$$

where C_0 and D_0 are parameters that define the resolution of the detector at a given energy. This is in agreement with experimental observations [85].

The normal practice in measuring the photon energy resolution of TINA (MINA) is to use the mono-energetic γ-ray from the radiative capture of stopped pions on protons and measure the full width at half maximum (FWHM) of the full energy peak. The resolution is defined as

$$R = \frac{FWHM}{H_0}$$

where H_0 is the mean pulse height corresponding to the same peak.

In this experiment, since mono-energetic γ-rays were not available, the Monte Carlo simulation method was used to estimate the resolution of TINA and MINA. A Monte Carlo program was written to reproduce the experimental $E_T \cdot E_M$ spectrum (Figure 4.3) . The program proceeds as follows:

- Since the $E_T \cdot E_M$ spectrum is independent of the π^0 kinetic energy, the pro-

gram randomly selects a π^0 energy within the physically allowed region.

- The π^0 decays into 2 photons with an opening angle of 180^0. The energies of the photons are calculated.

- The program picks randomly from a distribution function experimentally measured energies for the two photons E_T and E_M. The distribution function was the response function of NaI with the given C_0 and D_0. Since it is not necessary to know the energy resolutions very precisely for the analysis, a similar resolution was assumed for both TINA and MINA in order to simplify the procedure. This is a fair assumption because, although TINA is a larger crystal than MINA, the smaller collimator on MINA compensates this effect.

- A histogram of $E_T \cdot E_M$ spectrum is plotted.

The program was run a number of times varying C_0 and D_0 until the experimental spectrum was reproduced. The best values of C_0 and D_0 were $C_0 = 0.075$ and $D_0 = 0.39$, which corresponded to an energy resolution of $\sim$ 8.8 % at 100 MeV for both TINA and MINA.

The spectrometer measures the energy of the π^0 as the sum of the energies deposited in TINA and MINA. Since the response of TINA and MINA is a distribution, it was difficult to describe the response function of the spectrometer to π^0 mesons, using an analytical function. Hence a Monte Carlo simulation was done to determine the response of the spectrometer. Figure 4.7 shows the results of the simulation for a π^0 at rest and with 100 MeV kinetic energy.

4.4 The π^0 Detection Efficiency

When a neutral pion is created in the target it lives about 10^{-16} s, decaying into two oppositely directed photons in its own rest frame, each of which has an energy

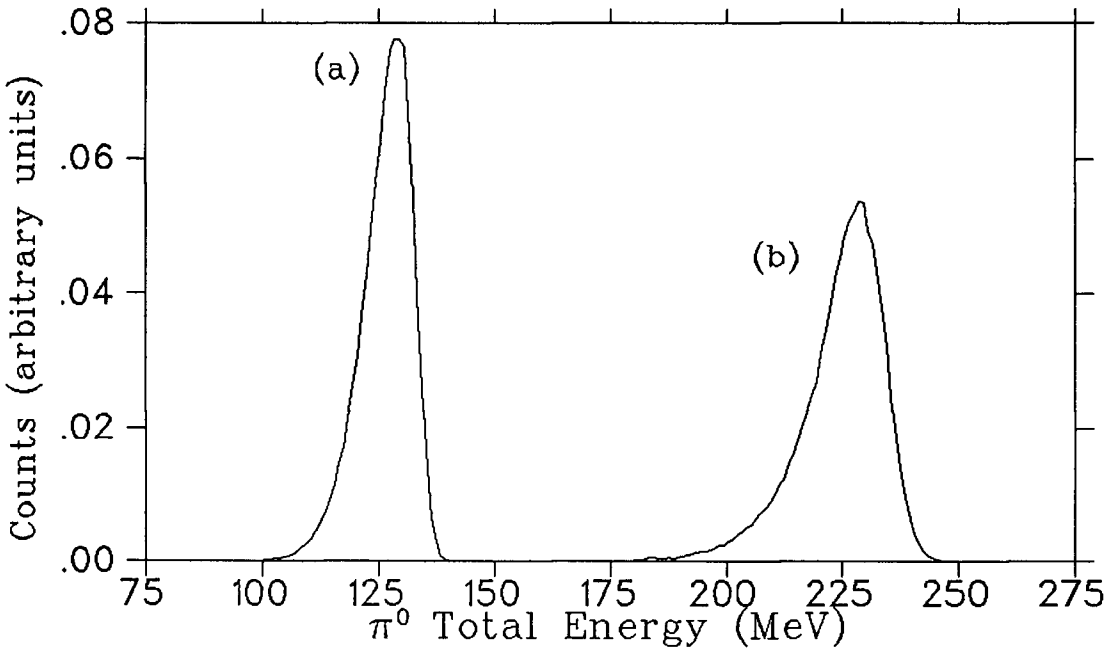

Figure 4.7: Response of the spectrometer to (a) a π^0 at rest and (b) a π^0 with a kinetic energy of 100 MeV

equal to half the pion rest mass. When viewed from a frame other than the pion rest frame, these photons appear with Doppler-shifted energies and with the 180^0 angle of emission altered by the Lorentz transformation. The spectrometer detects the neutral pions by detecting these photons. The following factors determine the efficiency of detecting a π^0.

1. The geometrical acceptance of TINA and MINA. This defines the solid angle available for detecting the individual γ-rays by the detectors.

2. The angle between the 2 arms of the spectrometer. The probability of observing the 2 photons in the laboratory with an opening angle between ψ and $\psi + d\psi$ is given by [86]

$$P(\psi) = \frac{1}{4\beta\gamma} \cdot \frac{cos\frac{\psi}{2}\, d\psi}{sin^2\,\frac{\psi}{2}\sqrt{\gamma^2 sin^2\,\frac{\psi}{2} - 1}} \tag{4.9}$$

   where γ and β are the usual relativistic constants of the π^0. This distribution is illustrated in Figure 4.8. As seen in the figure, the probability decreases with the increase of the angle between the two detectors.

3. The energy of the π^0, since the opening angle distribution is a function of the π^0 energy (Figure 4.8).

4. The efficiency of detecting photons by NaI. This is effectively 100 % if a γ-ray enters the aperture of the collimator.

The determination of the overall detection efficiency of the spectrometer was accomplished using the Monte Carlo method in the following manner. The only assumption made in the program was that the pions created in the reaction $p+p \rightarrow p+p+\pi^0$ have an isotropic angular distribution in the centre of mass. In the energy region of this experiment this is nearly so (see [15] and chapter 5). In the program

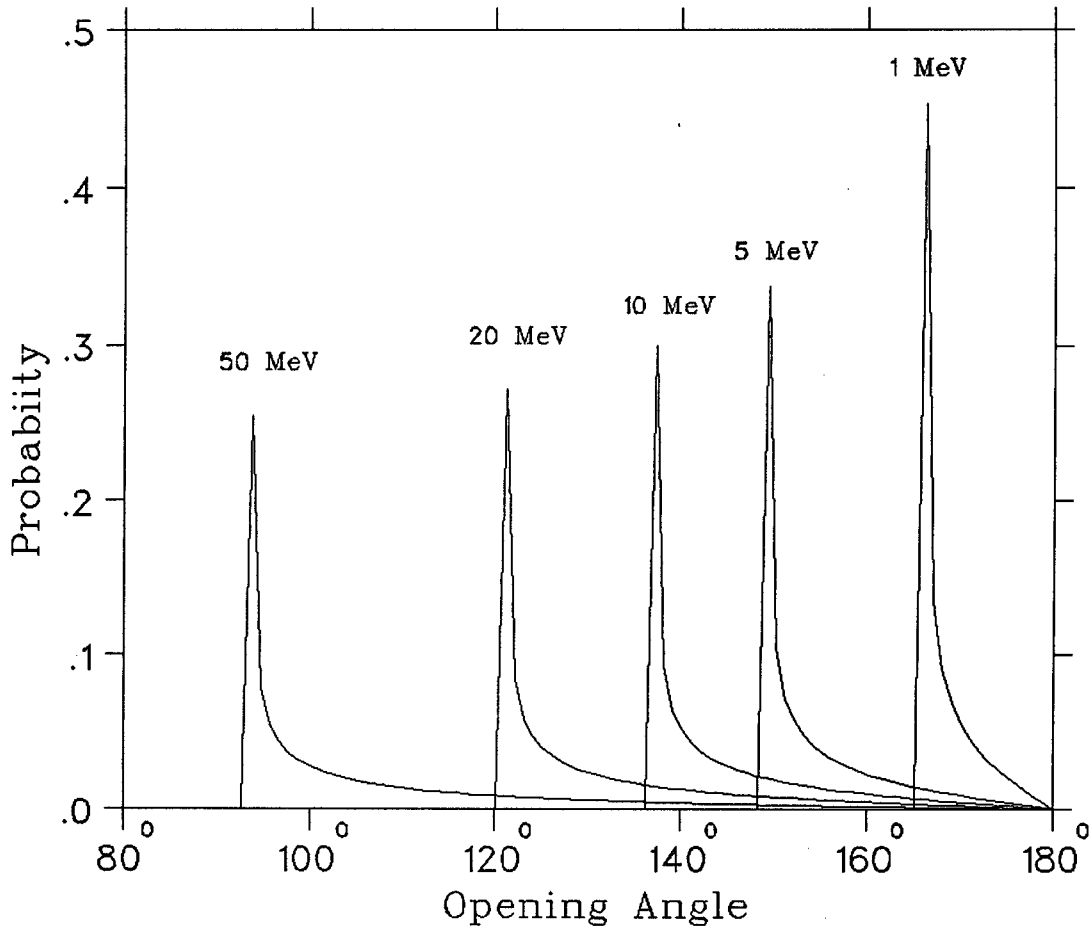

Figure 4.8: Distributions of the opening angle for the decay of a π^0, as a function of π^0 kinetic energy.

- π^0 mesons of given energy are generated isotropically in the centre of mass.
- The energy and angles of the π^0 are transformed from centre of mass to the laboratory frame.
- The position of the π^0 decay in the target is determined randomly.
- The π^0 is forced to decay into two photons with an opening angle given by the distribution of equation 4.8.
- The directions of motion and the energies of the two photons are calculated and it is checked if they hit both TINA and MINA.

The results of the Monte Carlo program were checked against the analytical calculations using the method of intersecting cones [87] for a point target, and the agreement was very good. Figure 4.9 shows the π^0 detection efficiency as a function of the π^0 kinetic energy. The efficiencies shown are for TINA and MINA at distances 120.8 cm and 125.5 cm respectively from the target. The collimators in front of TINA and MINA were of diameters 30 cm and 25 cm. The line is a fit to the Monte Carlo data points. In the course of the experiment, when the angles were changed, difficulties were experienced in keeping the distance of MINA from the target unchanged. The variance of this distance was always within 4 cm (but measured to $\sim$ 1 cm), which corresponds to a maximum of a 5% change in the efficiency. Instead of running the Monte Carlo program with all these distances, suitable corrections were made during the fitting process to account for this small variation in the efficiency.

4.5 π^0 Energy Spectra for Cross Section Analysis

The π^0 energy spectra were produced by defining the energy of the π^0 as the sum of the energies deposited in TINA and MINA. Since only the 180^0geometry

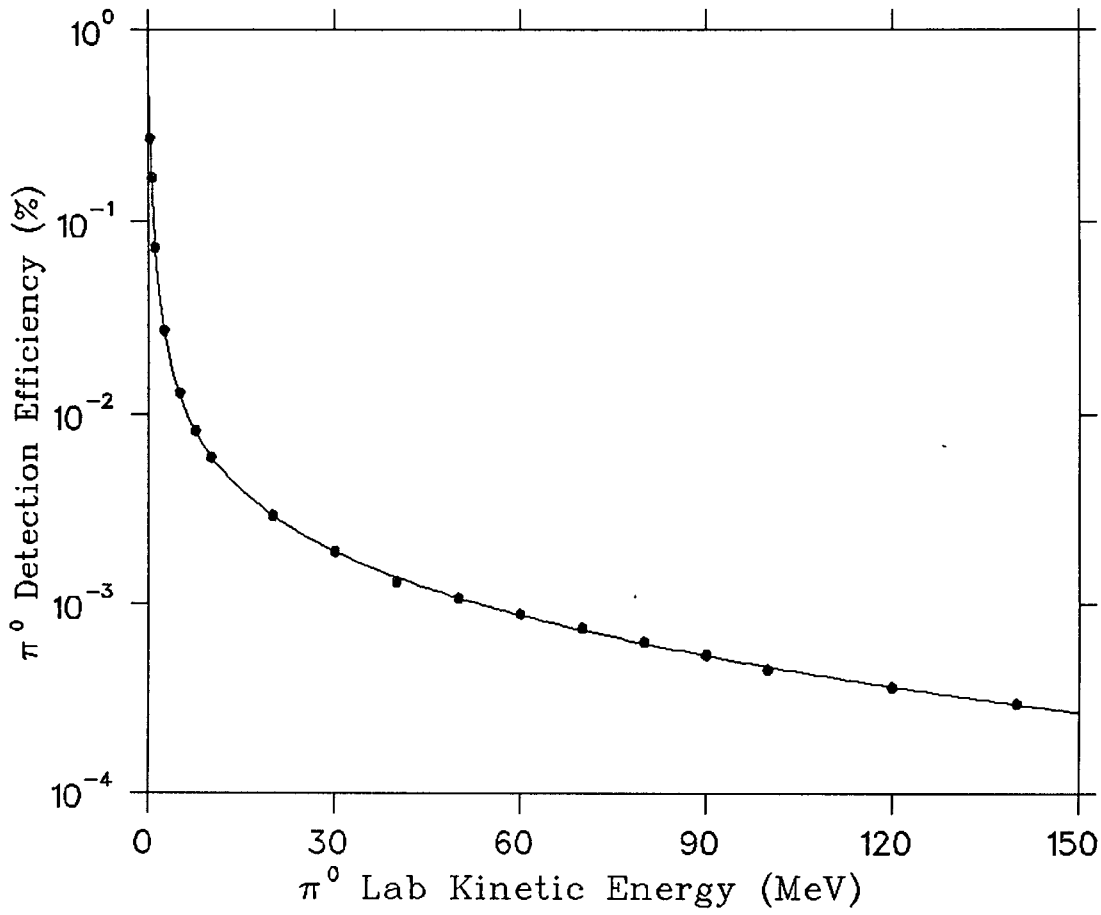

Figure 4.9: The π^0 detection efficiency (geometrical) as a function of the π^0 kinetic energy. Data points are results from Monte Carlo simulation and the solid line is a fit to the data.

data were used for cross section analysis, the direction of the π^0 was either the direction of TINA or MINA, whichever had the higher energy deposited. Since the number of incident protons with spin up and down were not identical, and also since the polarisation of the beam for the two spin states was slightly different, in order to obtain the unpolarised cross sections, the data were normalised as follows to produce the π^0 energy spectra.

If a polarised proton beam is incident upon an unpolarised target, the differential cross section $\frac{d\sigma}{d\Omega}$ can be written as

$$\frac{d\sigma}{d\Omega} = \frac{d\sigma_0}{d\Omega} + \overline{P} \cdot \overline{n} \frac{d\sigma_1}{d\Omega} \tag{4.10}$$

where

- $\frac{d\sigma_0}{d\Omega}$ is the unpolarised differential cross section
- $\frac{d\sigma_1}{d\Omega}$ is the polarised differential cross section
- $\overline{P}$ is the polarisation of the incident proton beam
- $\overline{n}$ is a unit vector normal to the scattering plane, in the direction $\overline{k}_i \times \overline{k}_f$.

From 4.10 the differential cross sections for spin up and down states can be written as

$$\frac{d\sigma^+}{d\Omega} = \frac{d\sigma_0}{d\Omega} + P^+ \frac{d\sigma_1}{d\Omega} \tag{4.11}$$

$$\frac{d\sigma^-}{d\Omega} = \frac{d\sigma_0}{d\Omega} - P^- \frac{d\sigma_1}{d\Omega} \tag{4.12}$$

where P^+ (P^-) is the average beam polarisation for spin UP (DOWN) state during a run. Equation 4.11 and 4.12 give

$$\frac{d\sigma_0}{d\Omega} = \frac{1}{2}\left[\frac{d\sigma^+}{d\Omega} + \frac{d\sigma^-}{d\Omega} - \left(\frac{P^+ - P^-}{P^+ + P^-}\right)\left(\frac{d\sigma^+}{d\Omega} - \frac{d\sigma^-}{d\Omega}\right)\right] \tag{4.13}$$

Hence the total cross section can be written as

$$\sigma_0 = \frac{1}{2}\left[\sigma^+ + \sigma^- - \left(\frac{P^+ - P^-}{P^+ + P^-}\right)(\sigma^+ - \sigma^-)\right] \tag{4.14}$$

$$\begin{aligned} &\sim \sigma^+ \cdot \frac{P^-}{P^+} + \sigma^- \\ &\sim \frac{N^+_{\pi^0}}{N^+_{LR}} \cdot \frac{P^-}{P^+} + \frac{N^-_{\pi^0}}{N^-_{LR}} \\ &\sim N^+_{\pi^0} \cdot \frac{N^-_{LR}}{N^+_{LR}} \cdot \frac{P^-}{P^+} + N^-_{\pi^0} \end{aligned} \tag{4.15}$$

where

- $N^+_{\pi^0}$ ($N^-_{\pi^0}$) is the number of pions with spin UP (DOWN)
- N^+_{LR} (N^-_{LR}) is the number of incident protons with spin UP (DOWN)

The spectra with spin UP, which had the higher number of counts, were normalised by the factor $\frac{N^-_{LR}}{N^+_{LR}} \cdot \frac{P^-}{P^+}$. The number of incident protons were also normalised accordingly.

4.6 Fitting the π^0 Energy Spectra

After producing the π^0 energy spectra for each run as mentioned above runs with low statistics were combined to increase the statistics of the spectra. Table 4.2 lists the information on the π^0 energy spectra used for the fits.

When protons are bombarded by protons, the energy distribution of the π^0 mesons created depends on the final states of the scattered protons and the π^0 (see chapter 1). The relative angular momentum of the nucleons and the pion serve as a convenient classification. For the three categories that are of interest in the energy region of this experiment the center of mass energy distributions have the form

$$\left(\frac{d\sigma_{11}}{dT}\right)_{Ss} \propto \eta \frac{(T_0 - T)^{\frac{1}{2}}}{T_0 - T - B'} \tag{4.16}$$

Table 4.2: Statistics of π^0 spectra.

Proton Energy (MeV)	Lab Angle	Number of π^0 events	Total number of π^0 events
496	40^0	5013	
	60^0	4758	
	80^0	3495	
	90^0	23114	
	100^0	3364	
	120^0	3535	
	140^0	4096	
			47375
450	40^0	6413	
	60^0	8010	
	80^0	9445	
	90^0	22334	
	100^0	8417	
	120^0	5820	
	140^0	3948	
			64387
402	40^0	6349	
	60^0	7874	
	80^0	6018	
	90^0	11910	
	100^0	5600	
	120^0	4513	
	140^0	2601	
			44865
349	60^0	3196	
	80^0	5445	
	90^0	8252	
	100^0	3716	
	120^0	797	
			17413
319	90^0	10139	
			10139

$$\left(\frac{d\sigma_{11}}{dT}\right)_{Ps} \propto \eta(T_0 - T)^{\frac{3}{2}} \tag{4.17}$$

$$\left(\frac{d\sigma_{11}}{dT}\right)_{Pp} \propto \eta^3(T_0 - T)^{\frac{3}{2}} \tag{4.18}$$

where η is the momentum of the π^0 in the center of mass, T_0 is the maximum kinetic energy of the π^0 in the center of mass and B' is the energy of the two nucleons in a virtual $^1S_0$ state which is nearly zero ($\simeq$ 60 keV). Although there is an additional contribution due to the interference between Ps and Pp classes, this was not considered in the fit as this term will be approximately cancelled out when integrated over all angles.

The Ss and Ps class distributions are isotropic in the center of mass whereas the Pp class has an additional $cos^2\theta$ term in the angular distribution. The differential and total cross sections as well as the angular distribution parameter were determined by fitting the above distributions to the experimental spectra. The fitting procedure consisted of a combination of the Monte Carlo method and a χ^2 minimisation.

The first step in the fitting was to create "theoretical" laboratory energy spectra for each of the above three centre of mass distributions. This was done using the Monte Carlo method. For each distribution π^0 mesons were randomly generated isotropically in the centre of mass. For the Pp class in addition to the isotropic distribution a $\cos^2\theta$ angular distribution was added. The energy and the direction of the mesons were transformed from the centre of mass frame to the laboratory frame and the energy spectra at the experimental laboratory angles were determined. These laboratory spectra had to be corrected for the detection efficiency and the response function of the spectrometer. These were accomplished by multiplying the spectra by the detection efficiency and then folding the resulting spectra with the response function of the spectrometer. This produced four "theoretical" energy spectra for each laboratory angle at a given proton energy.

The next step was to fit the "theoretical" energy spectra along with background terms to the experimental energy spectra, using MINUIT. Altogether two types of fits were performed. The first was a simultaneous fit of all angles at a given proton energy. Figure 3.7 shows how the laboratory energy spectra are related to the centre of mass ones. Each laboratory angle covers a unique area of a θ_{CM} vs. E_{CM} plot. Therefore in order to get an overall picture of the centre of mass and to obtain the angular distribution of the differential cross section, it was essential to fit all the spectra simultaneously. Furthermore an added advantage in fitting all angles simultaneously is that the interference terms will average out approximately.

The fitting function had the form:

$$f_i(E) = \sum_{j=1}^{4} A_j g_{ij}(E + C_i) + \frac{BG_i(E)}{E^3} \tag{4.19}$$

where

- i refers to a particular spectrum.
- g_{ij}, j=1,2,3 are the "theoretical" spectra in the laboratory system corresponding to the isotropic centre of mass energy spectra of Ss, Ps and Pp classes for the i^{th} experimental spectrum.
- g_{i4} is the "theoretical" laboratory energy spectrum of the Pp class with a $\cos^2\theta$ angular distribution. All the g_{ij} spectra were normalised to the total counts of the polarimeter(N_{LR}). Since the detection efficiencies were calculated for only one distance of MINA, suitable corrections were made in the normalisation to account for any deviation from the above value. This correction amounted to a maximum of 5%.
- A_{ij}, j=1,2,3,4 are the amplitudes associated with each "theoretical" spectrum.

- C_{ij} are parameters to make adjustments in the energy calibration. These parameters always turned out to be very small (<3MeV).

- The term $\frac{BG_i(E)}{E^3}$ was a background term. Various different forms were tried for the background, but this produced the best χ^2. The cross sections obtained were not sensitive to the shape of the background term.

  The χ^2 was defined as:

$$\chi^2 = \sum_{i=1}^{n} \sum_{k=1}^{N_i} \left(\frac{h_i(k) - f_i(k)}{\Delta_i(k)} \right)^2 \tag{4.20}$$

where

- $h_i(k)$ is the number of counts in the k^{th} bin of the i^{th} experimental energy spectrum.

- $\Delta_i(k)$ is the statistical error associated with $h_i(k)$. N_i is the maximum number of bins in i^{th} experimental spectrum.

For each proton energy, the number of spectra, number of parameters, number of data points and the values of χ^2 are listed in Table 4.3 where χ^2_ν is the χ^2 per degree of freedom. The parameter values obtained from the fit are listed in Table 4.4. The errors quoted are those calculated by the MINOS routine of MINUIT. This routine finds the true confidence interval (errors) on the parameters of the fit by examining the exact behaviour of the χ^2 function. In all analysis presented here, 1σ errors (68% confidence limit) have been used. Typical fits to the data are shown in Figure 4.10

The second type of fit, a global fit which contained spectra at all measured angles and energies was performed to study the energy dependence of the contributions from each class reactions towards the total cross section. This will be discussed in section 4.7.

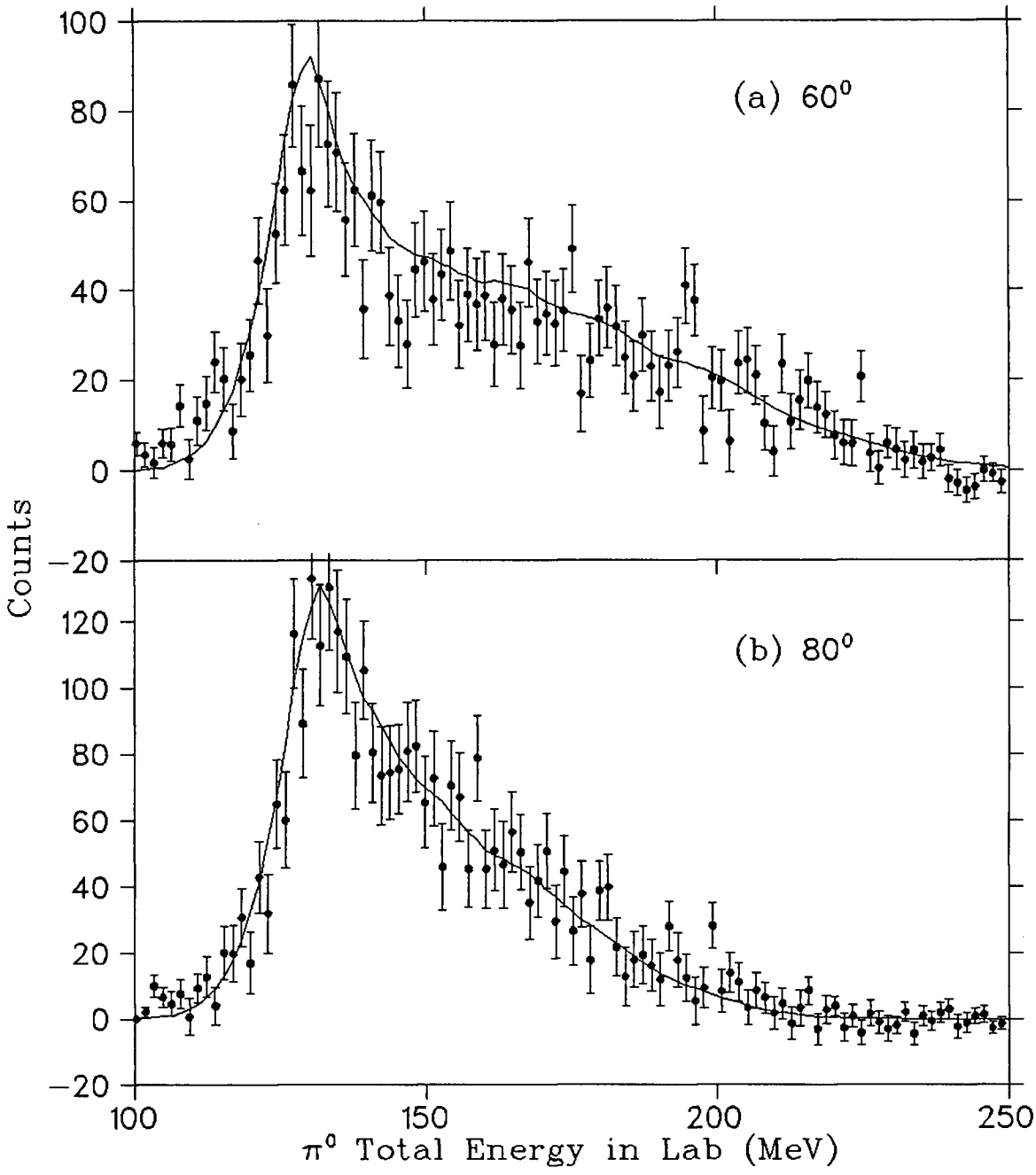

Figure 4.10: The observed π^0 energy spectra at (a) 60^0 (b) 80^0 laboratory angles for 496 MeV incident proton energy. Note that the spectrometer efficiency is far greater for low energy π^0s. The solid line is the fit to the data.

Table 4.3: Statistics of the fits to individual energies.

Proton Energy (MeV)	Angles	Number of spectra	Number of parameters	Number of data points	χ^2	χ^2_ν
496	40^0,60^0,80^0, 90^0,100^0, 120^0,140^0	12	28	1764	1668	0.96
450	40^0,60^0,80^0, 90^0,100^0, 120^0,140^0	16	36	2080	2058	1.01
402	40^0,60^0,80^0, 90^0,100^0, 120^0,140^0	14	32	1596	1647	1.05
349	60^0,80^0,90^0 100^0,120^0	10	24	800	756	0.97
319	90^0	6	16	376	314	0.88

Table 4.4: Parameter values from the fits to individual energies.

Proton Energy (MeV)	A_1	A_2	A_3	A_4
496	96.0 ± 55.0	0.0 $\pm^{2.1}_{0.0}$	1727 ± 48	197.2±20.6
450	0.0 $\pm^{2.6}_{0.0}$	0.0 $\pm^{8.3}_{0.0}$	857 ± 18	123.5 ± 8.8
402	0.0 $\pm^{0.6}_{0.0}$	38.7 ± 4.9	183.3 ± 6.8	35.8±2.6
349	16.2 ± 4.3	19.2 ±11.3	31.7 ± 13.0	3.7 ± 2.7
319	9.4 ± 1.8	21.9 $\pm^{5.5}_{21.9}$	0.0 $\pm^{12.0}_{0.0}$	0.3 $\pm^{5.0}_{0.3}$

4.7 Total and Differential Cross Sections

When fitting, all the "theoretical" spectra were individually normalised to the total number of polarimeter counts N_{LR} of the experimental spectra. This means that if A_i (i=1,2,3,4) are the fitted parameters then $A_i N_{LR}$ is the total number of π^0 mesons needed in the centre of mass to produce the experimental spectra. Hence the differential cross section can be expressed in the form:

$$\left(\frac{d\sigma}{d\Omega}\right)_{CM} = \frac{N_{LR}}{4\pi \cdot N_P \cdot N_H}\left[\sum_{i=1}^{3} A_i + A_4 cos^2\theta\right] \tag{4.21}$$

where

- $N_P = \frac{0.625 \times 10^{10}}{K} \cdot N_{LR}$ is the total number of incident protons.

  K is the polarimeter calibration factor (see section 3.2.1).

- $N_H = \frac{A\rho t}{m}$ is the number of protons in the target with $A = 6.022 \times 10^{23}$ is Avogadro's number.

  $\rho = 0.0708 g/cm^3$ is the density of liquid hydrogen at 20.27 K.

  $m = 1.0078$ is the atomic mass of hydrogen.

  $t = 5cm$ is the thickness of the target.

Hence:

$$\left(\frac{d\sigma}{d\Omega}\right)_{CM} = \frac{K \times 0.8 \times 10^{-6}}{4\pi}\left[\sum_{i=1}^{3} A_i + A_4 cos^2\theta\right] mb/sr \tag{4.22}$$

The angular distribution of $p + p \rightarrow p + p + \pi^0$ reaction in the centre of mass system can be expanded as a series of Legendre polynomials:

$$\left(\frac{d\sigma}{d\Omega}\right)_{CM} = \sum_{l=0}^{n} a_l P_l(cos\theta) \tag{4.23}$$

Since the two protons are indistinguishable in the centre of mass frame all pion angular distributions must have symmetry about a plane perpendicular to the line

joining the incoming protons. Thus the observations (in the CM system) at θ must be equivalent to those at 180-θ, therefore in the above expansion of the angular distribution only even powers of $cos\theta$ can appear. Also, there is experimental evidence [17] that powers of four and above are not required to describe the angular distribution in the energy region of this experiment. Hence the above equation can be written as:

$$\left(\frac{d\sigma}{d\Omega}\right)_{CM} = a_0 + 6a_2(cos^2\theta - \frac{1}{3}) \tag{4.24}$$

Equation 4.21 can be written as:

$$\left(\frac{d\sigma}{d\Omega}\right)_{CM} = \frac{K \times 0.8 \times 10^{-6}}{4\pi}\left[\sum_{i=1}^{3} A_i + \frac{A_4}{3} + A_4(cos^2\theta - \frac{1}{3})\right] mb/sr \tag{4.25}$$

From 4.23 and 4.24:

$$a_0 = \frac{0.8 \times 10^{-6} \times K}{4\pi}\left[\sum_{i=1}^{3} A_i + \frac{A_4}{3}\right] mb/sr \tag{4.26}$$

The total cross section is calculated from:

$$\sigma_T = 4\pi a_0 \tag{4.27}$$

Hence:

$$\sigma_T = 0.8 \times 10^{-6} \times K\left[\sum_{i=1}^{3} A_i + \frac{A_4}{3}\right] mb \tag{4.28}$$

It is normal practice [15] to express the differential cross section as

$$\left(\frac{d\sigma}{d\Omega}\right)_{CM} = a(\frac{1}{3} + b_{\pi^0}cos^2\theta) \tag{4.29}$$

Hence from equations 4.21 and 4.28 the angular distribution parameter b_{π^0} can be calculated by

$$b_{\pi^0} = \frac{A_4}{3\sum_{i=1}^{3} A_i} \tag{4.30}$$

Results of the values obtained for σ_T and b_{π^0} calculated from the above formulae are listed in Table 4.5. The errors quoted for the total cross section are due to

Table 4.5: Values of total cross section and the angular distribution parameter.

Proton Energy (MeV)	σ_T (μb)	b_{π^0}
496	656 ± 34	0.036 ± 0.013
450	285 ± 13	0.048 ± 0.013
402	69 ± 4	0.054 ± 0.015
349	18.1 ± 5.0	0.018 ± 0.016
319	7.8 $\pm^{3.0}_{5.0}$	0.003 ± 0.055

statistics and the uncertainty in the calibration of the polarimeter. For the errors of b an uncertainty due to the choice of the fitting function was added to those of the statistics (see section 4.9).

4.8 Contributions from Ss, Ps and Pp classes to the total cross section

Since the centre of mass energy spectra of Ss, Ps and Pp classes were used to fit the experimental spectra, the amplitudes $A_i (i = 1, 2, 3, 4)$ are directly related to the contributions of each class towards the total cross section. Each of the contributions are given by

$$\sigma_T^{Ss} = A_1 K', \quad \sigma_T^{Ps} = A_2 K' \quad and \quad \sigma_T^{Pp} = (A_3 + \frac{A_4}{3}) K' \tag{4.31}$$

where $K' = 0.8 \times 10^{-6} \times K$.

Tables 4.6 and 4.7 list the contributions of each class to the total cross section.

An attempt was made to study the excitation function of the total cross section

$$\sigma_{11} = B_1 \eta_0^2 + B_2 \eta_0^6 + B_3 \eta_0^8 \tag{4.32}$$

Table 4.6: Contributions from the three classes to σ_T.

Proton Energy (MeV)	σ_T^{Ss} (μb)	σ_T^{Ps} (μb)	σ_T^{Pp} (μb)
496	33.3 ± 19.1	$0.0 \pm^{0.7}_{0.0}$	622 ± 17
450	$0.0 \pm^{0.8}_{0.0}$	$0.0 \pm^{2.6}_{0.0}$	285 ± 6
402	$0.0 \pm^{0.2}_{0.0}$	11.4 ± 1.4	57.5 ± 2.0
349	4.3 ± 1.1	5.1 ± 3.0	8.7 ± 3.5
319	2.3 ± 0.4	$5.4 \pm^{1.4}_{5.4}$	$0.03 \pm^{3.0}_{0.03}$

Table 4.7: Contributions from the three classes to σ_T.

Proton Energy (MeV)	η_0	σ_T^{Ss}/η_0^2	σ_T^{Ps}/η_0^6	σ_T^{Pp}/η_0^8
496	1.333	18.7 ± 10.7	$0.0 \pm^{0.1}_{0.0}$	62.4 ± 1.7
450	1.157	$0.0 \pm^{0.6}_{0.0}$	$0.0 \pm^{1.1}_{0.0}$	88.6 ± 1.8
402	0.957	$0.0 \pm^{0.2}_{0.0}$	14.8 ± 1.8	81.7 ± 2.8
349	0.699	8.8 ± 2.3	43.7 ± 25.7	153 ± 61
319	0.517	8.6 ± 1.5	$283 \pm^{73}_{283}$	$6 \pm^{588}_{6}$

by performing a global fit to all angles and energies simultaneously. For the fitting purposes the term due to the Pp class was separated into its two components due to the two angular distributions. Then the function takes the form

$$\sigma_{11} = B_1\eta_0^2 + B_2\eta_0^6 + B_3\eta_0^8 + \frac{B_4}{3}\eta_0^8 \tag{4.33}$$

where $B_3\eta_0^8$ and $B_4\eta_0^8$ are the contrbutions from the isotropic and $cos^2\theta$ angular distributions of the Pp class. The fitting function and the χ^2 were defined as

$$f_{il}(E) = \sum_{j=1}^{4} A_j g_{ijl}(E + C_{il}) + \frac{BG_{il}(E)}{E^3} \tag{4.34}$$

and

$$\chi^2 = \sum_{l=1}^{m}\sum_{i=1}^{n}\sum_{k=1}^{N_i}\left(\frac{h_{il}(k) - f_{il}(k)}{\Delta_{il}(k)}\right)^2 \tag{4.35}$$

where A, f, g, h, C, BG and Δ all have the same meanings as in equations 4.11 and 4.12. The additional index l accounts for the proton energy.

For this fit the theoretical spectra g_{ijl} were normalised as follows:

Since from equation 4.32 the total cross section for the Ss class is $B_1\eta_{0,l}^2$, for a given proton energy,

$$A_1K' = B_1\eta_{0,l}^2 \quad , \qquad A_1 = B_1 \cdot \frac{\eta_{0,l}^2}{K'}$$

Similarly for other classes

$$A_2 = B_2 \cdot \frac{\eta_{0,l}^6}{K'}, \quad A_3 = B_3 \cdot \frac{\eta_{0,l}^8}{K'} \quad and \quad A_4 = B_4 \cdot \frac{\eta_{0,l}^8}{K'}$$

Hence, the g_{ijl} spectra were first normalised to the total number of polarimeter counts N_{LR} and then multiplying the three classes by $\eta_{0,l}^2$, $\eta_{0,l}^6$ and $\eta_{0,l}^8$ respectively. This fit turned out to be fairly complicated since it contained 96 parameters and ~6000 data points. In order to simplify the fit and to obtain an unambiguous

Table 4.8: Statistics of the global fits.

Energy Region (MeV)	Number of spectra	Number of data points	χ^2	χ^2_ν
319 - 450	46	5980	6155	1.03
319 -402	30	3900	3893	1.00

Table 4.9: Parameter values of the global fits.

Energy Region (MeV)	B_1	B_2	B_3	B_4
319 - 450	15.2 $\pm$ 0.4	11.4 $\pm$ 1.2	69.7 $\pm$ 1.6	14.0 $\pm$ 0.7
319 - 402	15.2 $\pm$ 0.4	22.8 $\pm$ 1.8	51.0 $\pm$ 2.7	18.0 $\pm$ 1.0

result, all the C(energy calibration) and BG(background) parameters were fixed at the values obtained from the earlier fits. This left only the four A_j parameters to be fitted. Since the excitation function is valid only at low energies, the range of which cannot be clearly defined, two fits were performed one for the region 320 to 400 MeV and the other from 320 to 450 MeV. The number of spectra, number of data points used for the fit and the resulting χ^2 values are listed in Table 4.8. The results of the fit are shown in Table 4.9.

An alternative approach for estimating the contributions of the three classes is to fit the excitation function (equation 4.32) directly to the total cross sections alone. This had been the practice in the past. Although this is an easy and quite straight forward method, it lacks the information available in the energy spectra. This method was used in the past because the pion energy spectra were not available. In

order to be able to compare our results consistently with the previous measurements, a fit was performed to only the total cross sections, using the excitation function. The results of this fit along with the global fit are shown below:

From the total cross sections fit: 319 MeV - 450 MeV

$$\sigma_{11} = (15.6 \pm 6.1)\eta_0^2 + (0.0 \pm^{13.4}_{0.0})\eta_0^6 + (79.8 \pm^{5.5}_{9.5})\eta_0^8 \tag{4.36}$$

From the Global fit: 319 MeV - 450 MeV

$$\sigma_{11} = (15.2 \pm 0.4)\eta_0^2 + (11.4 \pm 1.2)\eta_0^6 + (74.4 \pm 1.6)\eta_0^8 \tag{4.37}$$

From Global fit: 319 MeV - 402 MeV

$$\sigma_{11} = (15.2 \pm 0.4)\eta_0^2 + (22.8 \pm 1.8)\eta_0^6 + (57.0 \pm 2.7)\eta_0^8 \tag{4.38}$$

Since the polarimeter calibration has a reproducible uncertainty of about 4%, the effect of this uncertainty on the fits were checked as follows. The calibration directly affects the number of incident protons. Hence all the above fits were redone varying the number of incident protons randomly up to 4%. The resulting values of the parameters were within the errors of the original parameters.

In order to check the sensitivity of the results to the FWHM of the resolution of the spectrometer, the resolution was changed arbitrarily and the data were re-analysed. Use of a 20% better resolution produced a total cross section of about 4% less than the values obtained earlier. Hence a small uncertainty in the resolution of the spectrometer will not affect the final result.

4.9 Fitting π^0 Energy Spectra with General Functions

Instead of fitting the experimental spectra with the centre of mass energy distributions of Ss, Ps and Pp classes given by Gell Mann, an attempt was made to fit the experimental data with a general function. Using the results obtained by

Cence et al. [17] at 735 MeV as a guide, the centre of mass energy distributions were defined by

$$f(T) = A_1 T^{B_1}(T_0 - T)^{C_1} + A_2 T^{B_2}(T_0 - T)^{C_2} \tag{4.39}$$

where T_0 is the maximum kinetic energy of the π^0 in the centre of mass, B_i, C_i are parameters that define the shape of the centre of mass spectrum and A_i are normalisation parameters. The function has two terms, both of them going naturally to zero at lower and higher energies. The lower energy part of the π^0 spectrum is described mainly by the first term and the higher energy part mainly by the second term. Although fitting a general function of this form is difficult to perform, it fitted the experimental spectra quite well and gave total cross sections identical to the ones obtained from the fits discussed earlier. For the parameter b,although the values obtained were very similar, the numbers were about 50-60% different. Hence an additional uncertainty of 50-60% due to the choice of the fitting function was added to the statistical errors of b in determining the total errors quoted in Table 4.5. No global fit was attempted, only spectra from individual energies were fitted. The parameters typically had the values

$$B_1 \sim 1.0, \quad C_1 \sim 1.5$$

$$B_2 \sim 3.0, \quad C_2 \sim 2.0$$

A phase space term was also introduced to the fit, but was rejected by the fitting routine.

4.10 Analysis of the Analysing Power Data

As mentioned earlier, in order ensure that the neutrons do not affect the analysing powers of the π^0 a 2σ cut was imposed on the time of flight of the neutral particles in selecting the photon events in TINA and MINA. Except for this, in

producing the final spectra for analysis of the analysing powers the other cuts and background subtractions were done in the same way as for the cross section data.

In the experiment two types of geometries were used, one with TINA and MINA at 180^0 to each other and the other at symmetric angles. The 180^0 geometry has the advantage that the direction of the π^0 can be clearly defined. Except at very low π^0 energies, the pion detected are those that move either towards TINA or MINA. The symmetrical geometry has the advantage that the left-right asymmetry can be observed in a clear and simple way. When a π^0 decays into two photons, conservation of energy and momentum requires that the higher energy photon has a smaller angle with respect to the π^0 than the low energy photon. Hence the sign of $E_M - E_T$ defines the direction (left or right with respect to the beam) of the π^0. Figure 4.11 shows typical $E_M - E_T$ spectra when the spin of the incident proton was up and down. This clearly shows that more pions are going to the right when the spin is up and to the left when the spin is down.

A major disadvantage of the symmetric geometry is that at these geometries the laboratory angle of the detected π^0 is not single-valued, but is a function of its kinetic energy. This dependence can be calculated from kinematics. In Figure 4.12 is shown a two dimensional Monte Carlo simulated energy spectrum of the π^0 from the reaction $p + p \rightarrow p + p + \pi^0$ assuming an isotropic π^0 angular distribution in the centre of mass. The solid lines show the π^0 lab angle as a function of the π^0 laboratory kinetic energy for the geometries used in this experiment. This plot was used to define the angle of the π^0 for symmetric geometries.

As stated in chapter 3, bits were set in the Camac module C212 coincidence buffer to identify the spin of the incident proton. These were used to produce the π^0 energy spectra separately for the spin up and down states in order to calculate the analysing powers. The analysing power is defined as the ratio of the polarised

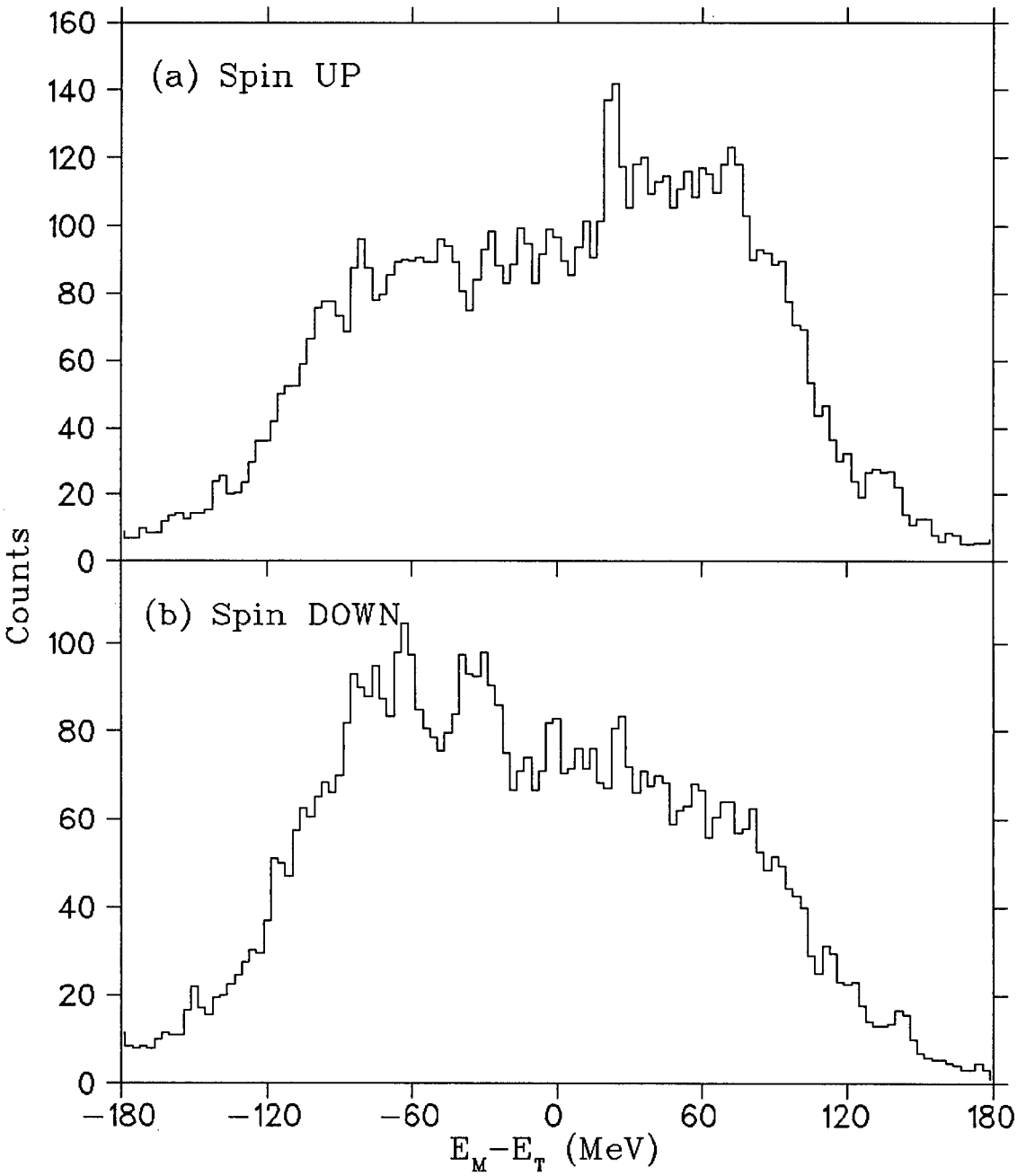

Figure 4.11: The spectrum of the energy difference between 2 γs from the decay of a π^0 when the spin of the proton is (a) UP and (b) DOWN. The direction of the high energy γ defines the direction of the π^0.

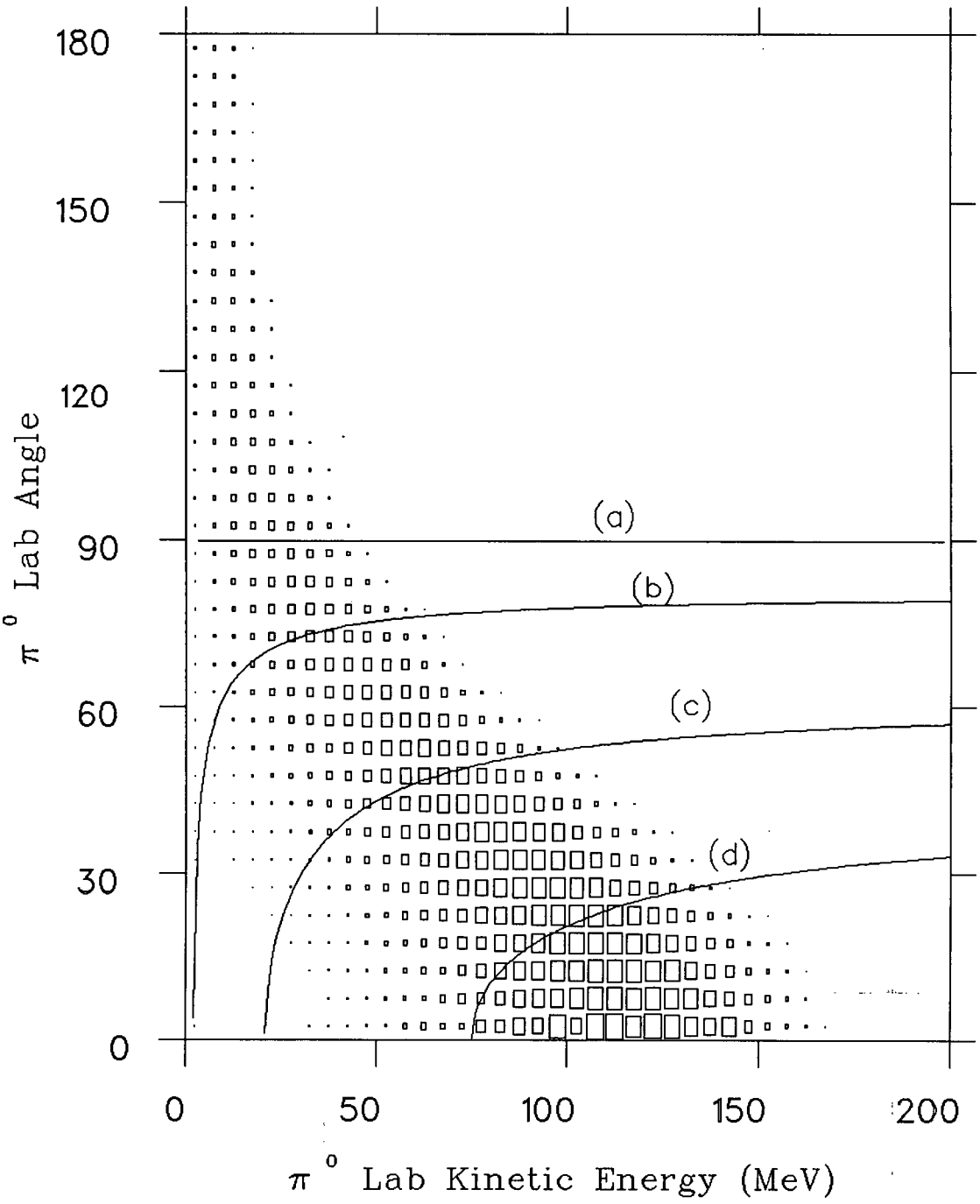

Figure 4.12: Kinematics of the symmetric geometry at 450 MeV. The lines show the relationship between the direction and the energy of the π^0 mesons detected at (a) 90^0 -90^0 (b) 80^0 -80^0 (c) 60^0 -60^0 and (d) 40^0 -40^0 . The density plot is a Monte Carlo simulation of the π^0 angular and energy distributions.

to unpolarised differential cross sections, i.e.

$$A_N(\theta, T_\pi) = \frac{d\sigma_1}{d\Omega} / \frac{d\sigma_0}{d\Omega} \tag{4.40}$$

From equations 4.11, 4.12 and 4.40 it can be shown that

$$A_N(\theta, T_\pi) = \frac{\sigma^+ - \sigma^-}{P^-\sigma^+ + P^+\sigma^-} \tag{4.41}$$

where P^+ and P^- are the beam polarisations for spin up and spin down states respectively, according to Madison convention [88]. These were calculated using the formula 3.1.

The differential cross sections σ^+ and σ^- were defined as

$$\sigma = \frac{N_{\pi^0}}{N_P \cdot N_H \cdot \Delta\Omega \cdot eff} = \frac{N_{\pi^0} \cdot K}{0.625 \times 10^{10} \cdot N_{LR} \cdot N_H \cdot \Delta\Omega \cdot eff} \tag{4.42}$$

Since the number of protons in the target N_H, the solid angle $\Delta\Omega$ and the detection efficiency eff are independent of the spin of the proton, for a given measurement equation 4.41 simplifies to

$$A_N(\theta, T_\pi) = \frac{\frac{N^+_{\pi^0}}{N^+_{LR}} - \frac{N^-_{\pi^0}}{N^-_{LR}}}{P^-\frac{N^+_{\pi^0}}{N^+_{LR}} + P^+\frac{N^-_{\pi^0}}{N^-_{LR}}} \tag{4.43}$$

where $N^{+(-)}_{LR}$ refer to the number of polarimeter counts with spin up(down). The analysing powers obtained are listed in appendix A. The same are plotted in Figures 4.13 to 4.17.

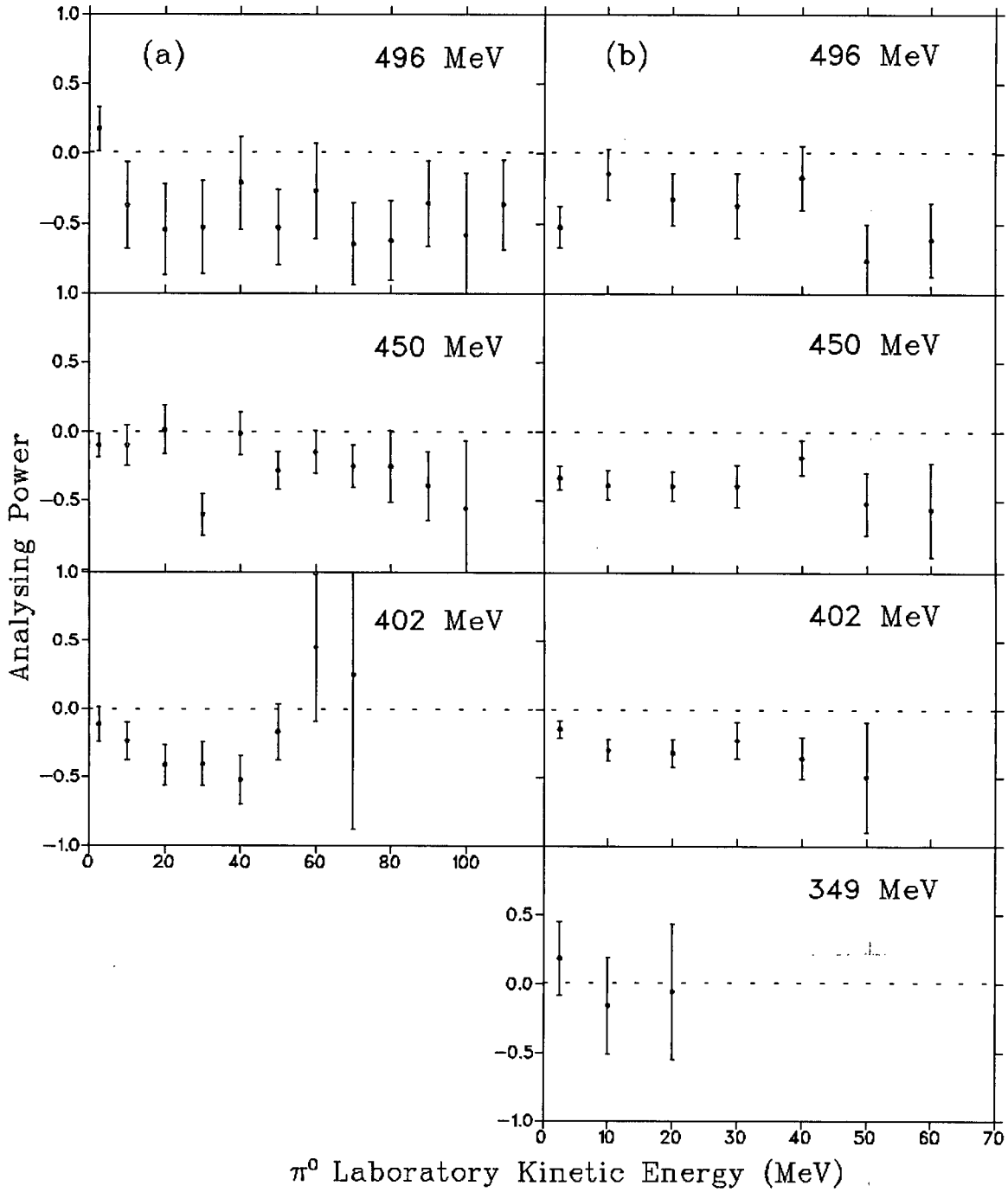

Figure 4.13: Analysing powers at the laboratory angle of (a) 40^0 and (b) 60^0 for incident proton energies of 496 MeV, 450 MeV, 402 MeV and 350 MeV.

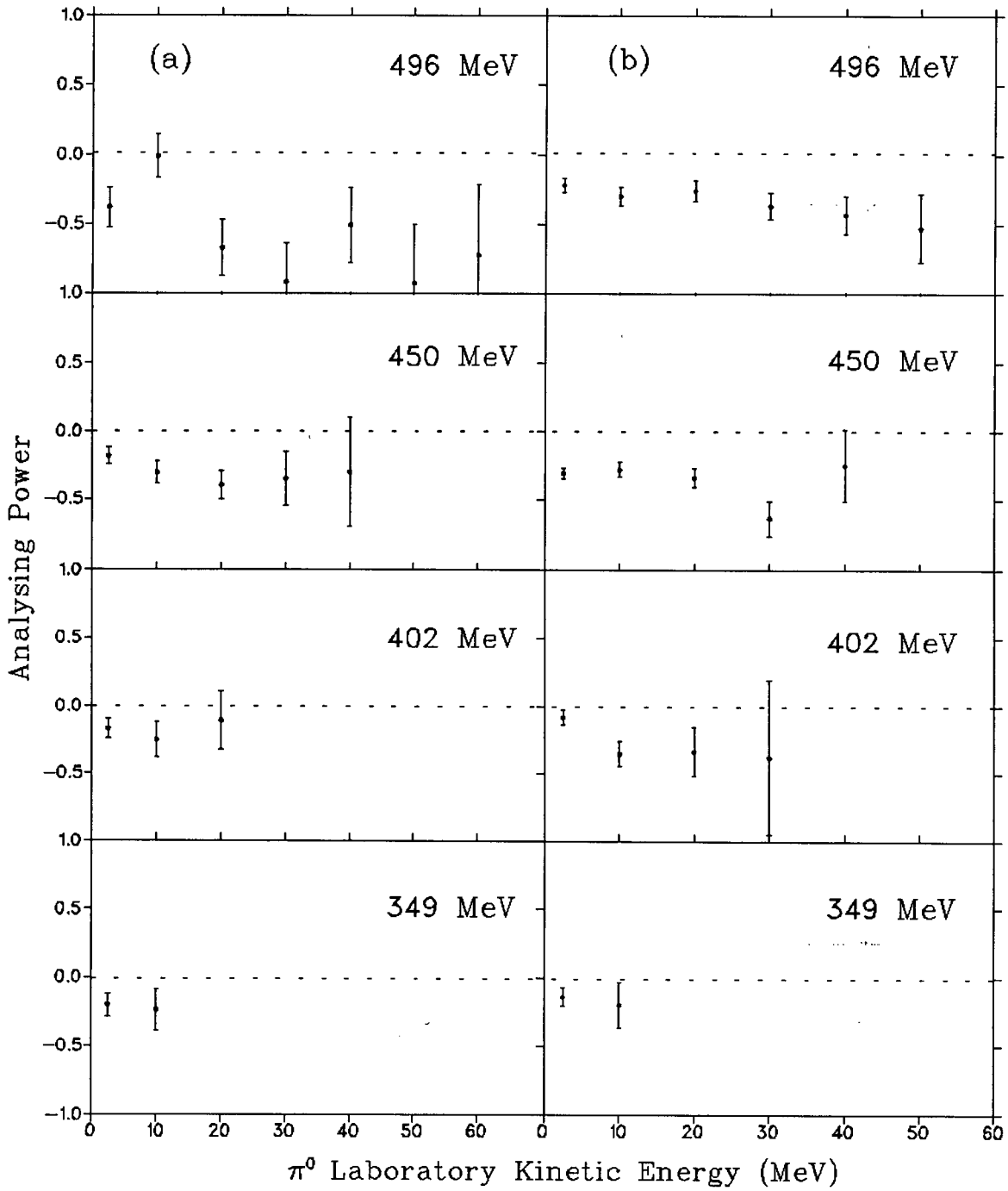

Figure 4.14: Analysing powers at the laboratory angle of (a) 80^0 and (b) 90^0 for incident proton energies of 496 MeV, 450 MeV, 402 MeV and 350 MeV.

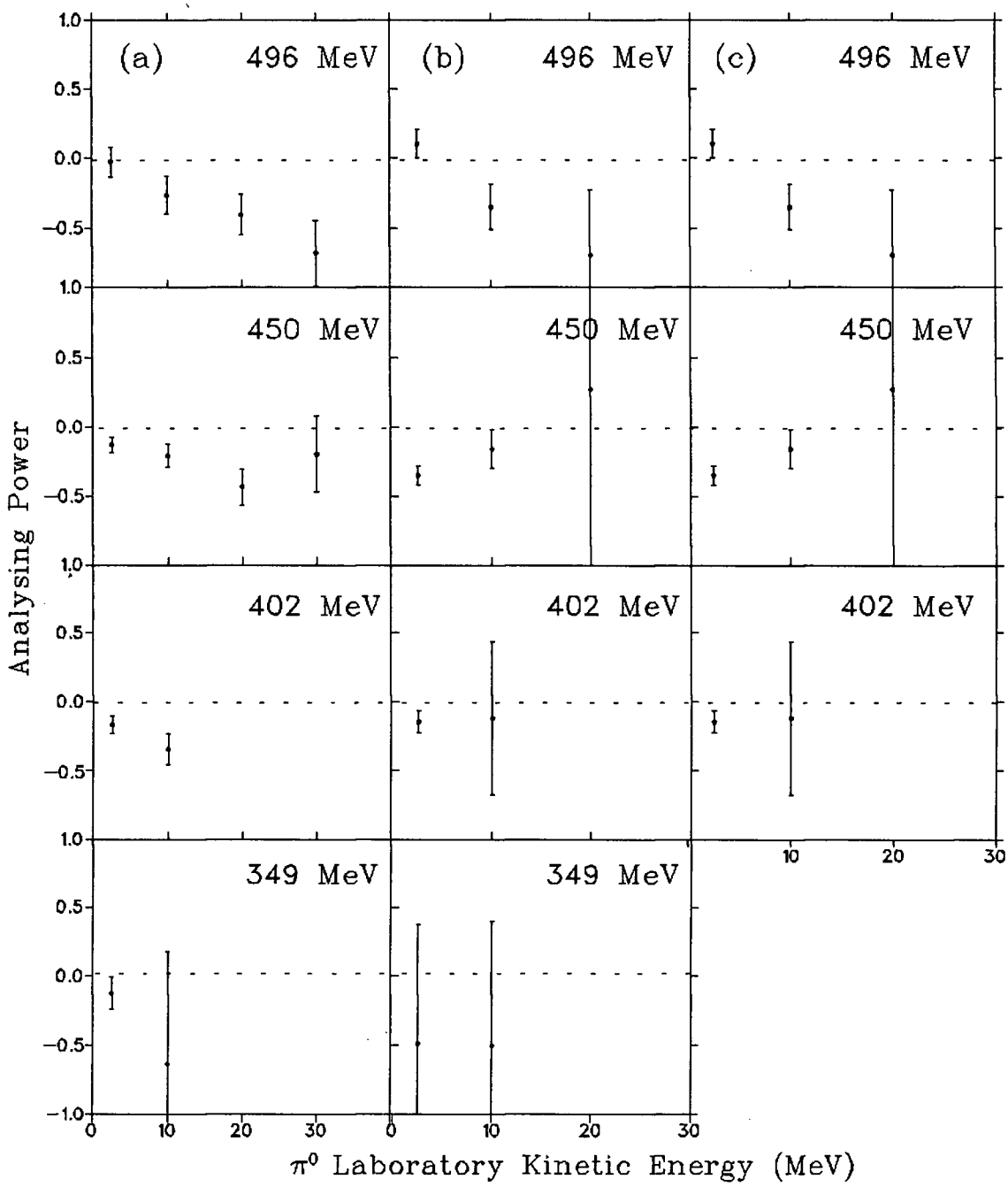

Figure 4.15: Analysing powers at the laboratory angle of (a) 100^0 (b) 120^0 and (c) 140^0 for incident proton energies of 496 MeV, 450 MeV, 402 MeV and 350 MeV.

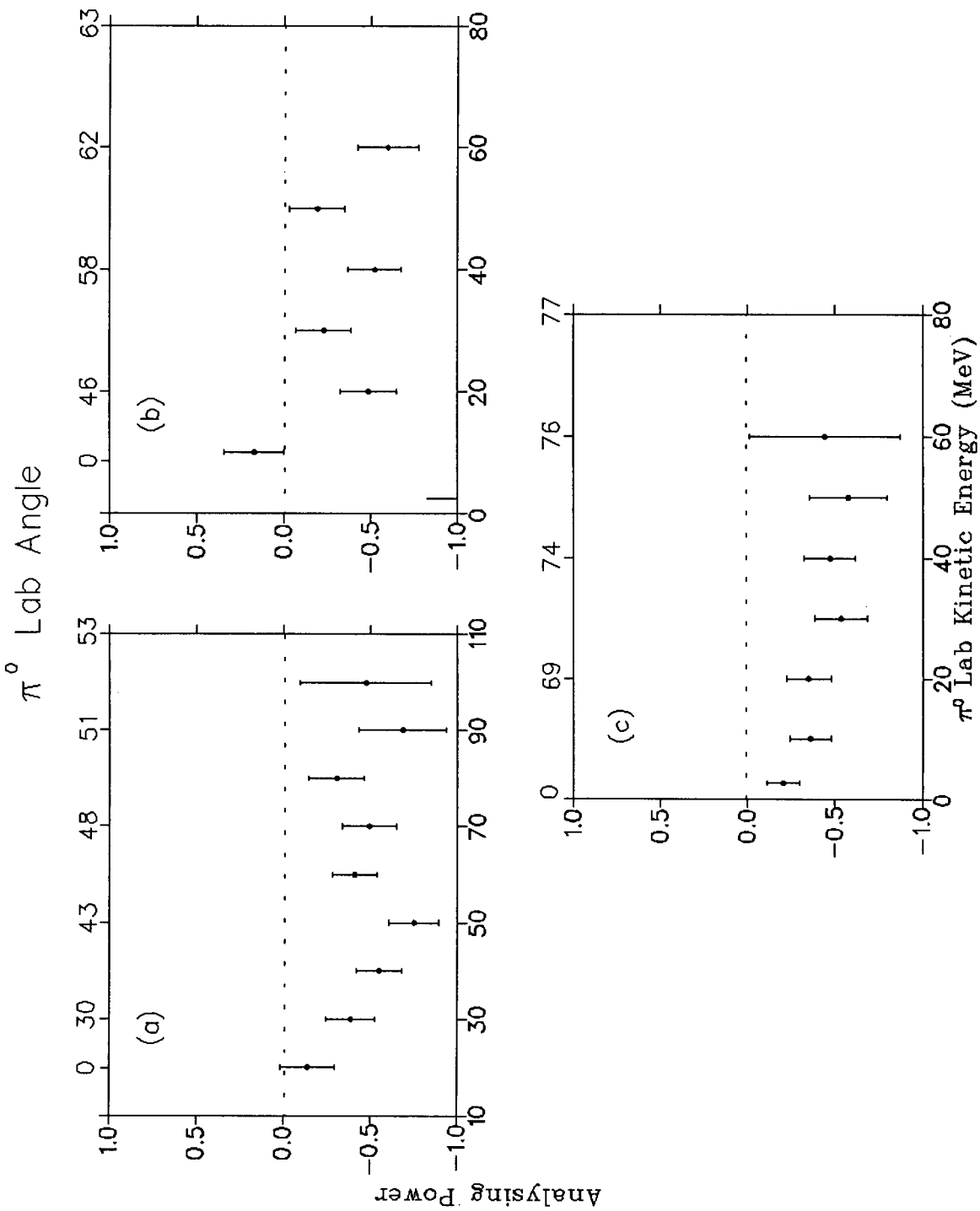

Figure 4.16: Analysing powers from the symmetric geometries at 496 MeV. (a) 60^0-60^0 (b) 70^0-70^0 and (c) 80^0-80^0.

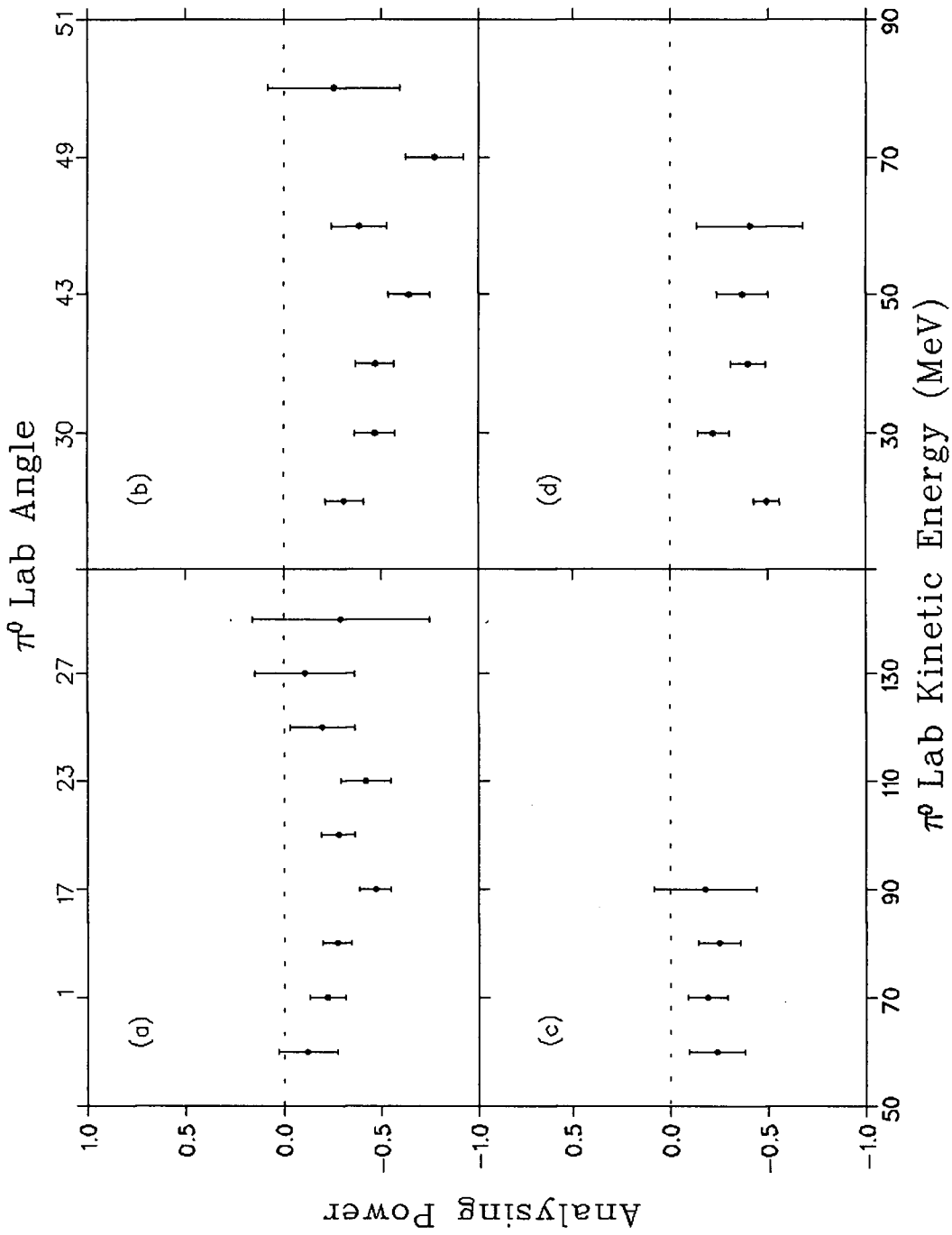

Figure 4.17: Analysing powers from the symmetric geometries at 450 and 402 MeV. (a) 450 MeV : 40^0-40^0(b) 450 MeV : 60^0-60^0(c) 402 MeV : 40^0-40^0(d) 402 MeV : 60^0-60^0.

Chapter 5

Discussion and Conclusions

5.1 Total Cross sections

5.1.1 Comparison with previous measurements

The results of the total cross section measurements for the reaction $p + p \rightarrow p + p + \pi^0$ of this investigation are shown in Figures 5.1 and 5.2 along with those of Dunaitsev and Prokoshkin [15], Stallwood et al. [14], Cence et al. [17], Shimizu et al. [16] and Marshall et al. [89]. Figure 5.1 shows the results in a logarithmic scale whereas Figure 5.2 shows the same in a linear scale. As seen in the figures our results are in very good agreement with the previous measurements. The results of Dunaitsev and Prokoshkin are slightly higher than ours at lower energies while our results tend to be a bit higher at higher energies. The data set of Stallwood et al. are closer to our results, whereas the recent measurements of Shimizu et al. are systematically larger than all the others in our energy region. Our results are of much higher accuracy compared to the earlier measurements at higher energies ($\geq$ 400 MeV). At lower energies (319 and 350 MeV) they are still better than the previous measurements, but our error bars are slightly larger due to the poor statistics and insufficient information on the π^0 angular distribution. Data for these energies were taken during the last two days of the assigned beam time and hence complete measurements were not possible. The major problem is that the data taking rate is low, and limited by pile-up due to elastic protons. At these low cross sections the large background π^0 production from carbon also contributes to the large error bars. An experiment devoted entirely to the low energy range

($\leq$ 350 MeV) is required to make a very precise measurement of the total cross section. However such a measurement is not essential as a fair amount of important information for the energy region can be extracted from the higher energy data (section 5.1.2).

In the analysis, although fits were performed using the predicted energy distributions of Gell-Mann [8], our total cross section results are not model dependent because alternate fits with general functions produced identical results.

The main differences between this investigation and the previous ones are: In the present experiment

1. The energy of the decay γ-rays were fairly precisely measured whereas in previous measurements in this energy range the energy was not measured at all. Only Cence et al.[17] measured the γ-ray energy but this was at a higher energy of 735 MeV.

2. Both the decay γ-rays were detected whereby the direction and the energy of the π^0 mesons were precisely determined. In the previous experiments the energy and the direction of the π^0 were not both measured but were obtained by fairly complicated fitting procedures.

These improvements of the technique are clearly demonstrated in Figures 5.1 and 5.2.

5.1.2 S-wave total cross sections

As mentioned in chapter 4 two types of fits were performed, individual energy fits and global fits. In all the fits there were parameters that would decide the contribution from each intensity class to the total cross section. The resulting contributions obtained from individual energy fits have been listed in table 4.7 and the results from global fits given in equations 4.36 and 4.37. The two sets of

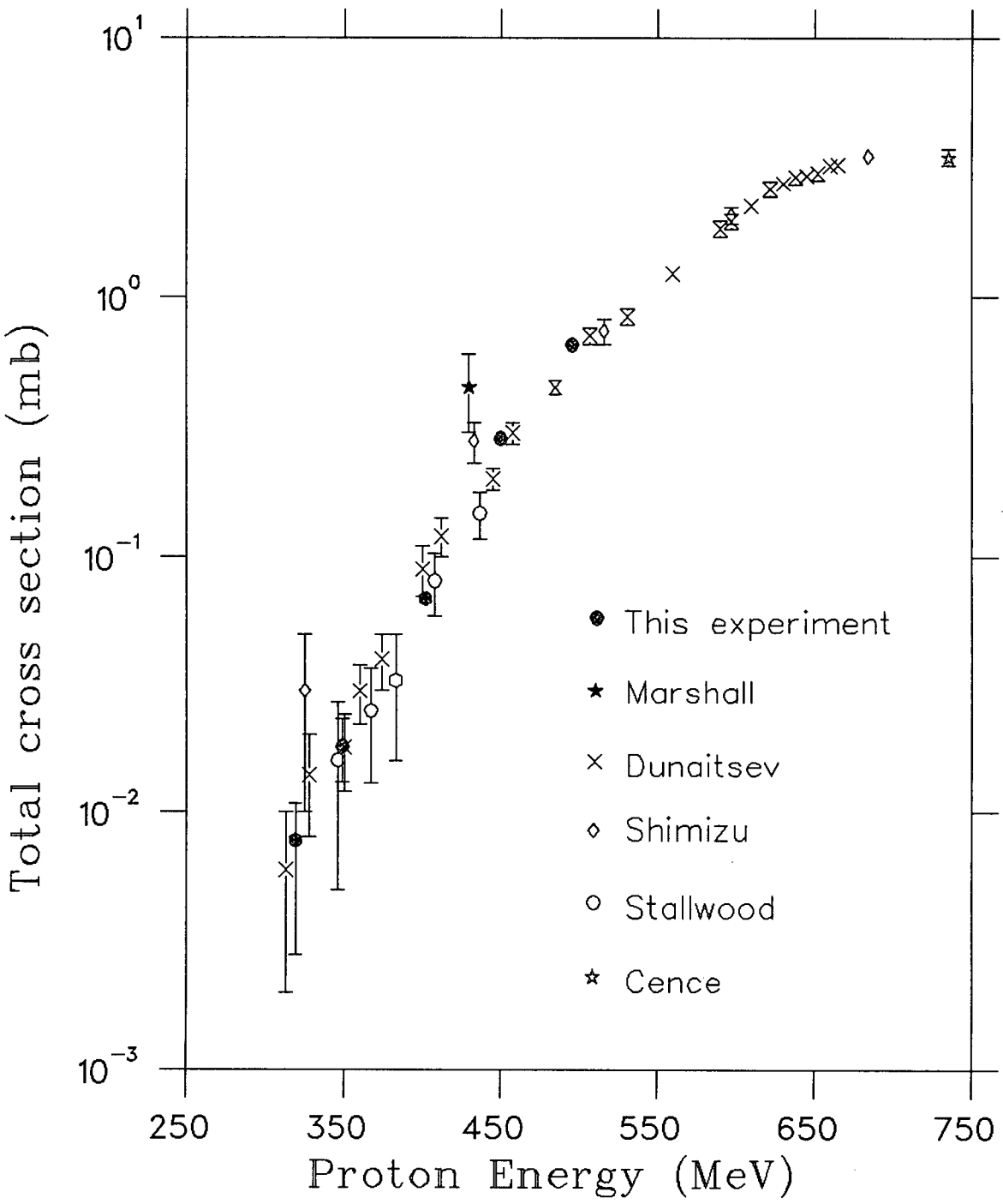

Figure 5.1: Total cross sections for the reaction $p + p \rightarrow p + p + \pi^0$.

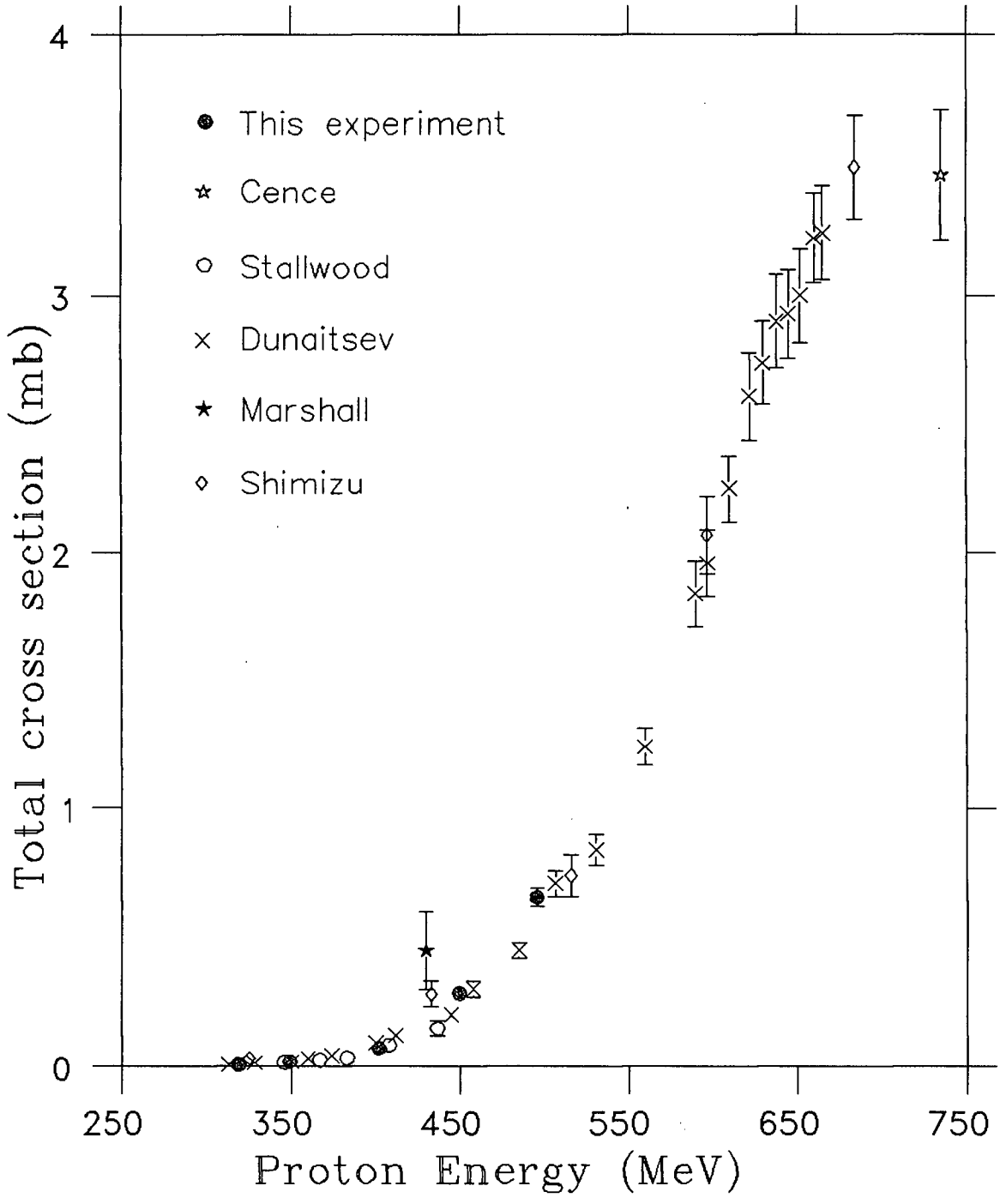

Figure 5.2: Total cross sections for the reaction $p + p \rightarrow p + p + \pi^0$

results appear to show slight differences. Although the s-wave transitions should be dominant at lower energies, the s-wave total cross sections given by the individual energy fits to 319 and 349 MeV data seem to give a lower cross section than the value obtained from the global fits. The reason for this is clear from tables 4.6 or 4.7. The errors given in these tables are an indication of the sensitivity of our data (or the sensitivity of a particular energy) to the three classes of transitions. Low energies are insensitive to p-waves whereas the high energies are very sensitive to p-waves, as expected. Thus at these low energies there is very little information on p-wave transitions and the fitting program cannot determine them. This is demonstrated by the large error bars on p-wave cross sections seen in table 4.7. The inability to determine the p-wave cross sections has affected the s-wave results of the low energy individual energy fits. This was checked by refitting the 319 and 349 MeV data, but this time constraining the p-waves to the values obtained from the global fits. The s-wave total cross sections obtained from the resulting fits are in good agreement with those obtained from global fits. The two fits had reduced χ^2 values of 0.90 and 0.98 respectively which are not worse than the ones given in table 4.3. The results obtained were:

$$319 \text{ MeV}: \quad \sigma_T^{Ss}(\mu b) = (14.8 \pm 0.6)\eta_0^2 \tag{5.1}$$

$$349 \text{ MeV}: \quad \sigma_T^{Ss}(\mu b) = (14.1 \pm 1.4)\eta_0^2 \tag{5.2}$$

Hence it is very clear that the contribution from the Ss class to the total cross section is $(15.2 \pm 0.4)\eta_0^2$ (μb). This is confirmed by the results of the fit to total cross sections (equation 4.35) which gives this contribution as $(15.6 \pm 6.1)\eta_0^2$ (μb). The very small error bars on the result of the global fit as compared to the total cross section fit is an indication of the large amount of information available to the global fit which is not available to the total cross section fit. The errors quoted here are purely the statistical errors given by MINUIT. In addition to this there are

the errors due to the choice of the functions (see section 4.9), constraints from the high energy data and the uncertainty of the resolution of the detectors. Of these, the constraints from high energy data make the largest contributions to the errors. In order to study this effect the 319 MeV and 349 MeV individual energy fits were redone by constraining the Ps and Pp parameters as follows. These two energies were chosen as they are the most sensitive to the Ss transition.

1. The excitation function $\sigma_{11} = B_1\eta_0^2 + B_2\eta_0^6 + B_3\eta_0^8$ was fitted to all the available $pp \rightarrow pp\pi^0$ data for the total cross section from threshold up to 500 MeV. B_2 and B_3 were then constrained to the values obtained from this fit.

2. (1) was repeated using world data up to 550 MeV.

3. (1) and (2) were repeated for 349 MeV, with only B_3 constrained.

The value of the B_1 parameter obtained along with those obtained from the global fit and the individual energy fits with all three parameters free, are given in Table 5.1. As mentioned earlier, the low value of B_1 in individual energy fits with all B_i parameters free is due to the unavailability of sufficient information on P-waves at these low energies. In the other fits, at 319 MeV, the value of B_1 does not seem to be too sensitive to B_2 and B_3 as long as they are reasonable, but at 349 MeV B_1 is fairly sensitive. This of course is expected as B_2 and B_3 are significant relative to B_1 as seen in Tables 4.6 or 4.7. Now the values at which we have fixed B_2 and B_3 may not be quite valid, as these were obtained from fits to higher energies at which the predictions of Gell Mann may not be valid any more. Yet the wander of B_1 in the 349 MeV fit is an indication that it is fairly sensitive to the values of B_2 and B_3. But notice that when B_2 is let free in the 349 MeV fit, B_1 settles back to around 15.0. Because of the variations between the different fits we have assigned an error of 3.0 μb for these systematic problems. This gives the s-wave total cross section

Table 5.1: Variations of B_1 with B_2 and B_3

Type of fit	B_1 from 319 MeV fit	B_1 from 349 MeV fit
All B_i free	8.6 ± 1.5	8.8 ± 2.3
Global fit	15.2 ± 0.4	15.2 ± 0.4
B_2 and B_3 from 300-510 MeV fit	14.0 ± 0.5	25.6 ± 1.0
B_2 and B_3 from 300-560 MeV fit	13.5 ± 0.6	22.1 ± 1.0
B_3 from from 300-500 MeV fit B_2 free		14.6 ± 1.4

as $(15.2 \pm 3.0)\eta_0^2$ (μb). For a model independent result the uncertainty should be about 6.0 μb.

In order to compare our fits with the results of the previous measurements total cross section fits were performed to the measurements of Dunaitsev and Prokoshkin and also Stallwood et al. in the energy region below 450 MeV, and the results obtained were:

$$\text{Dunaitsev} : \sigma_{11}(\mu b) = (23.9 \pm^{10.4}_{8.2})\eta_0^2 + (82 \pm^{11}_{50})\eta_0^6 + (0 \pm^{37}_{0})\eta_0^8 \tag{5.3}$$

$$\text{Stallwood} : \sigma_{11}(\mu b) = (22.6 \pm^{14.9}_{19.1})\eta_0^2 + (21 \pm^{100}_{21})\eta_0^6 + (38 \pm^{32}_{38})\eta_0^8 \tag{5.4}$$

The Ss contributions given by these fits, though of very poor quality, are in agreement with our measurements. Although our fit to the data of Dunaitsev and Prokoshkin gives the Ss parameter as $(23.9 \pm^{10.4}_{8.2})$, the number given by the authors is 32 ± 7. They obtained this parameter by assuming the Mandelstam model and fixing the p-wave parameters at the values given by the model. Hence the

value given by them clearly depends on the validity of Mandelstam's model and cannot be compared with our result. The reason for this approach, we believe is that their data below 450 MeV were not accurate enough to determine the s and p-wave contributions as seen by the results of our fits to their data. In Figure 5.3 the excitation function obtained from the three fits to our data as well as from the fits to the data of Dunaitsev and Prokoshkin and of Stallwood et al. are shown. The three lines fitted to our data do not deviate significantly from each other,and so are fairly consistent. The fits obtained from earlier experiments appear to deviate significantly from ours, but it should be remembered that their fits have large uncertainties, both statistical and systematic.

Although both global fits give identical values for the parameter B_1, the values obtained for B_2 and B_3 are outside their errors in the two fits. This is an indication that our data are unable to completely distinguish between Ps and Pp classes. Hence using the two sets of values given in equations 4.37 and 4.38 we have obtained an average set for B_2 and B_3. They have been assigned a larger error to cover the results from both fits. With these the overall result obtained from our experiment is estimated to be:

$$\sigma_{11}(\mu b) = (15.6 \pm 6.0)\eta_0^2 + (17 \pm 8)\eta_0^6 + (66 \pm 11)\eta_0^8 \qquad (5.5)$$

The energy dependence of the total cross sections of the three classes obtained from the above excitation function is shown in Figure 5.4. In Figure 5.5 the same is shown as a fraction of the total cross section. It is clear that near threshold the Ss transition is the dominant cross section, but as the energy increases its contribution becomes less important due to the rapid increase of Pp. The contribution from Ps is less important and is around 20%.

Our results for the s-wave total cross sections are very sensitive to the assumption that the π^0 energy distributions are those given by Gell-Mann. Near threshold

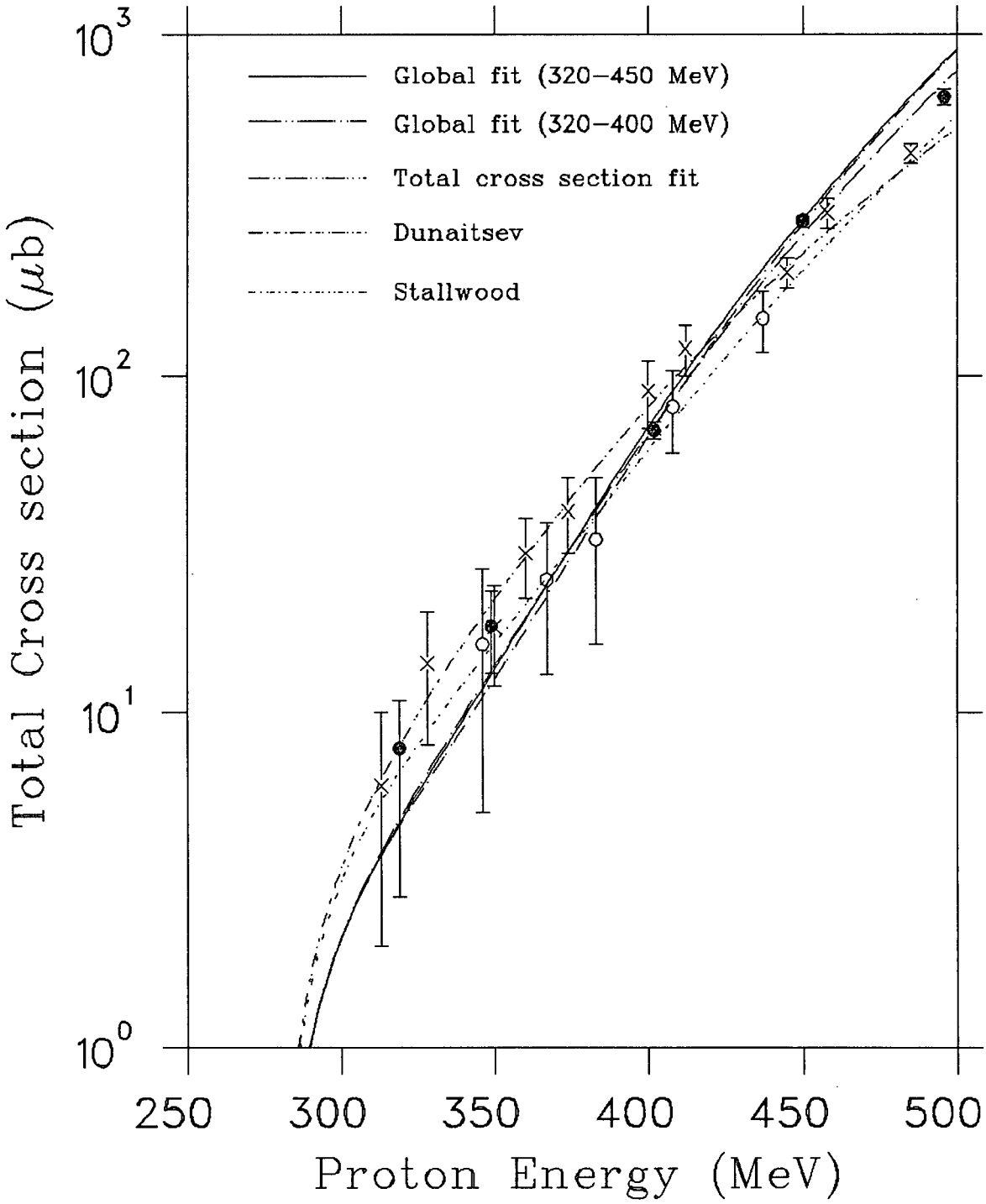

Figure 5.3: The excitation function for the reaction $p + p \rightarrow p + p + \pi^0$.

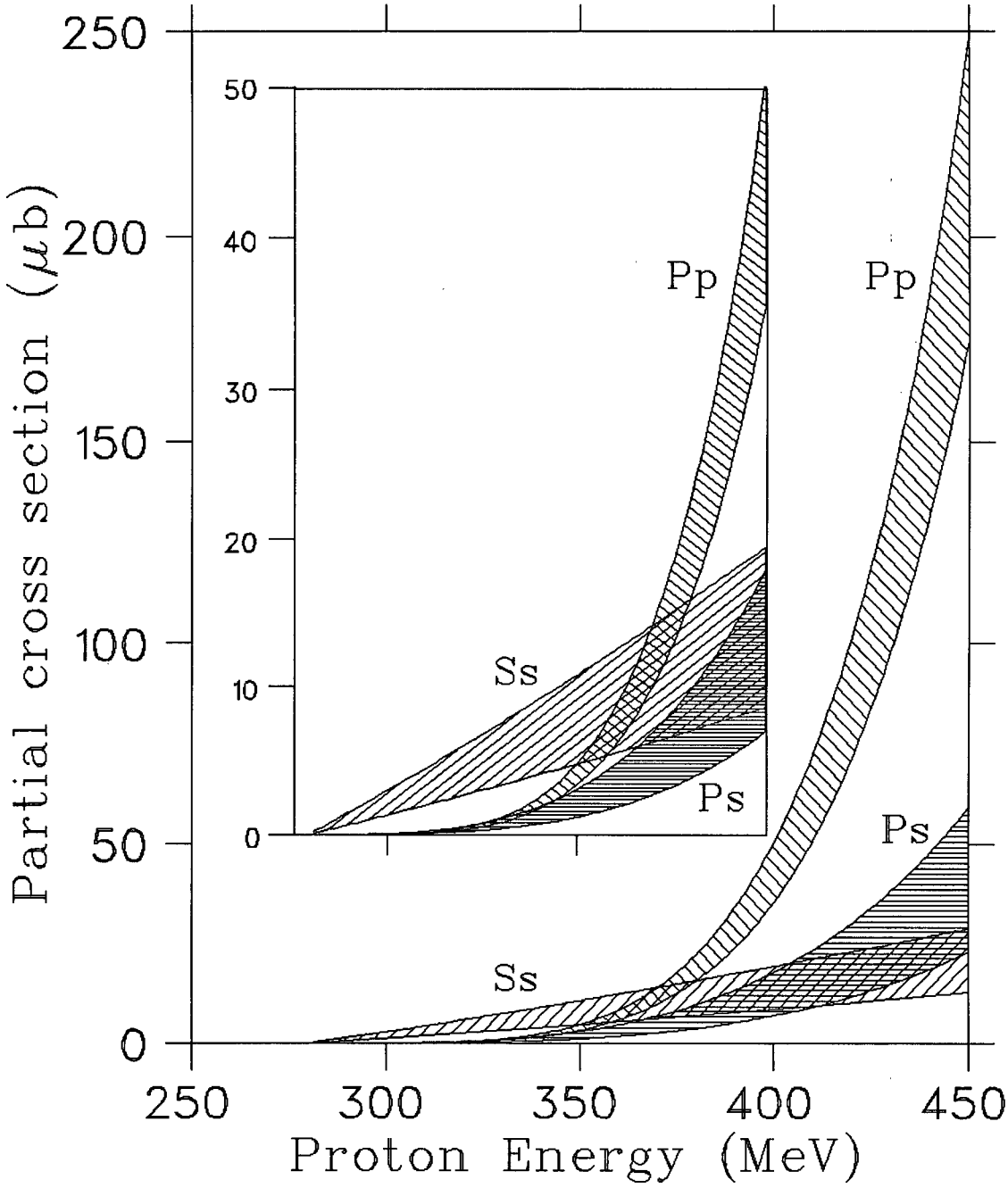

Figure 5.4: The energy dependence of the Ss, Ps and Pp partial cross sections. The shaded areas represent the uncertainties

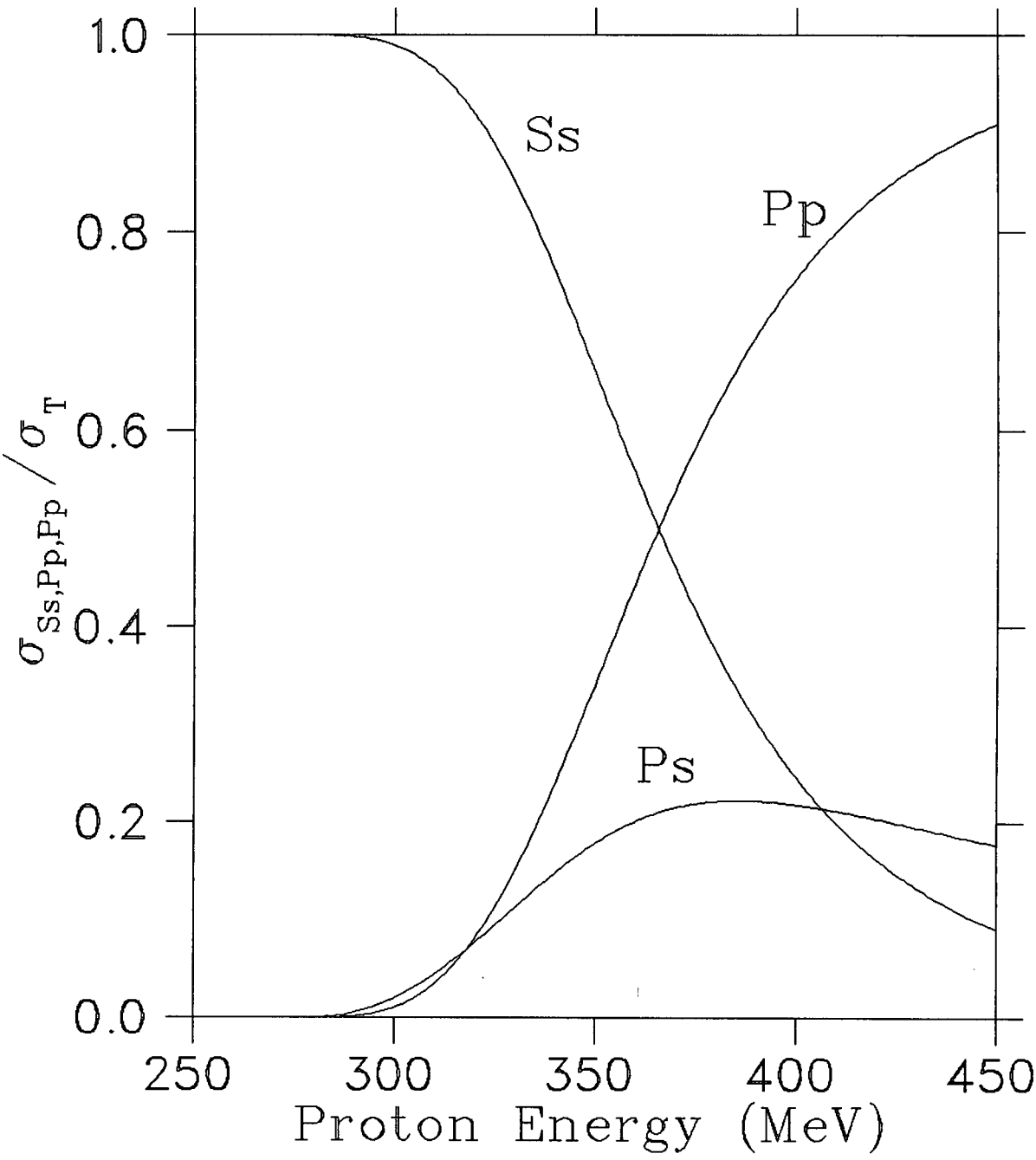

Figure 5.5: The energy dependence of the Ss, Ps and Pp partial cross sections.

the relations derived by Gell-Mann will be accurate, but it is not clear how good the assumption is at 400 or 500 MeV.

It is interesting to compare the S-wave production of pions in the reaction $pp \rightarrow pp\pi^0$ with other reactions. For the reaction $pp \rightarrow \pi^+ d$ the equivalent parameter fits the relation $\sigma(pp \rightarrow \pi^+ d) = \alpha\eta + \beta\eta^3$, with α being the S-wave contribution, which has the value of ~ 250 μb [90] much higher than in our reaction. Unfortunately for $np \rightarrow \pi^- pp$ there is only evidence from Handler, but it is clearly small.

5.1.3 Comparison with theory

As stated in chapter 2 only a few of the theoretical calculations make specific predictions of the reaction $pp \rightarrow pp\pi^0$. The S-wave calculations done by Efrosinin et al.[56] predict B_1 to be in the range 11-18 μb. The calculations of Koltun and Reitan for S-wave pion production near threshold found B_1 to be 17 μb. These calculations are in good agreement with our measurements. Unfortunately none of the other recent calculations that have worked fairly well for the reaction $pp \rightarrow \pi^+ d$ make any predictions for the reaction $pp \rightarrow pp\pi^0$, hence no comparisons can be made at the moment.

5.2 Angular Distribution of the π^0

In Figure 5.6 are shown our measurements of the π^0 angular distribution parameter b along with the results of Dunaitsev and Prokoshkin [15], Cence et al.[17] and Guzhavin et al.[18]. The two solid lines represent the values of the parameter obtained from the two global fits. The dotted lines are an extrapolation of the same to higher energies. As seen in the figure our results are consistent with the earlier measurements but of much higher precision. In their measurements Dunaitsev and Prokoshkin obtained the angular distribution of the π^0 mesons from measurements of the angular distribution of the γ-rays from the decay of the

π^0. The angular distributions of the γ-rays and the π^0 mesons are connected by relations, the analysis of which has shown that even at very high energies and with an anisotropic distribution of the π^0 mesons, the γ-ray angular distribution differs comparatively little from isotropic [13]. Only at π^0 meson energies above 200 MeV does the angular distribution of the γ-rays approach that of the π^0 mesons. This uncertainty is clearly demonstrated by the large error bars seen in their results. An accurate measurement of the γ-ray energy along with the angular distribution would have minimised these uncertainties. Cence et al.[17] in their measurements at 735 MeV did measure both energy and angular distribution of the γ-rays and were able to obtain a very precise measurement of the b parameter. In the present measurement the results have very small uncertainties because we improved the technique significantly by measuring both the angular and energy distributions of the π^0 mesons instead of those of the γ-rays. The improvement is very clearly seen in Figure 5.6. Unfortunately the maximum energy available at TRIUMF is 500 MeV. It would be valuable to determine the b parameter from 500 to 750 MeV to map out the change in the character of the angular distribution. Although it is not clear how far we can extrapolate the results from our global fits due to the non validity of Gell Mann and Watson's functions, the extrapolated values of b (dotted lines) are consistent with the experimental results of Dunaitsev and Prokoshkin and of Guzhavin et al.

5.3 Comparison with $np \rightarrow NN\pi^{\pm}$

As mentioned in chapter 1 there has been an ongoing interest concerning the value of σ_{01}. The normal practice in determining σ_{01} has been to use the total cross sections of the reactions $pp \rightarrow pp\pi^0$ and $np \rightarrow NN\pi^{\pm}$.

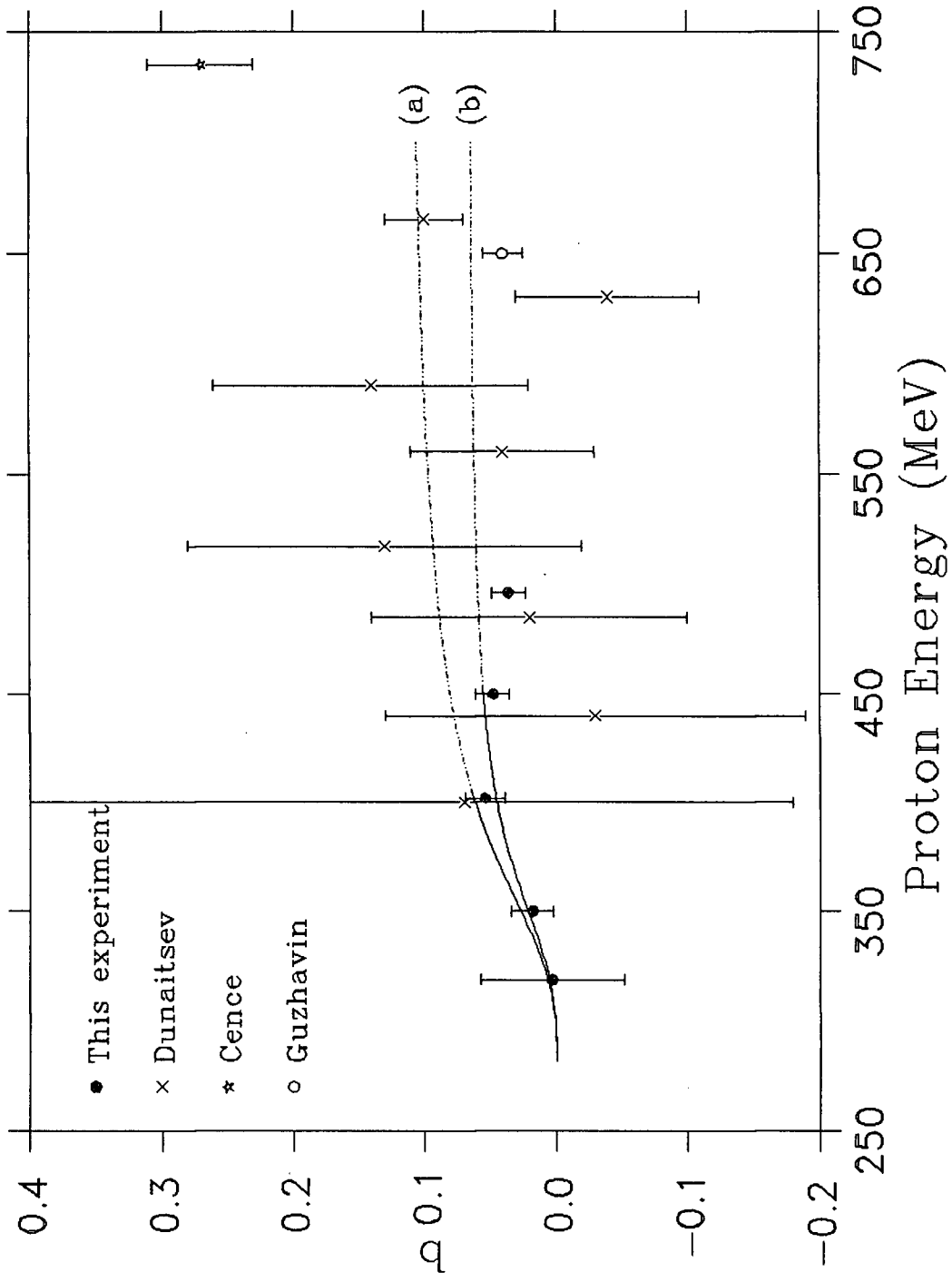

Figure 5.6: Energy dependence of the π^0 angular distribution parameter b from the relation $d\sigma/d\Omega \propto \frac{1}{3} + b\ cos^2\theta$. The solid lines are the values obtained from the global fits (a) 320-402 MeV and (b) 320-450 MeV. The dotted lines are extrapolations to higher energies.

Since:-

$$\sigma(pp \rightarrow pp\pi^0) = \sigma_{11}$$

$$and \qquad \sigma(np \rightarrow NN\pi^{\pm}) = \tfrac{1}{2}(\sigma_{01} + \sigma_{11})$$

$$thus \quad \sigma_{01} = 2\sigma(np \rightarrow NN\pi^{\pm}) - \sigma(pp \rightarrow pp\pi^0) \tag{5.6}$$

In Figure 5.7 all the available data on $\sigma(pp \rightarrow pp\pi^0)$ and $2\sigma(np \rightarrow NN\pi^{\pm})$ are plotted. The following observations can be made from the plot.

1. Between 400 and ~600 MeV σ_{01} is small but non-zero.

2. Between ~600 and 700 MeV σ_{01} appears to be consistent with zero, but it seems reasonable to assume that it is larger than in the lower energy region.

3. Above 700 MeV σ_{01} is non-zero and increases with energy.

Apart from the above no other conclusions can be made due to the unavailability of data in certain energy regions and the inconsistency of data in other energy regions. An obvious way to determine σ_{01} would be to fit both sets of data and do the subtraction. Such an approach was taken recently by Bystricky et al. [91] who used all the available inelastic nucleon-nucleon data and did a consistent fit. They found that above 3 GeV the I=1 and I=0 inelastic cross sections are of the same magnitude. Below 600 MeV σ_{01} was found to be small, but they have stated that this still plays an important role and cannot be neglected. They have estimated the I=0 cross sections in two different approaches ((A) using the $np \rightarrow np\pi^0$, $np \rightarrow pp\pi^-$, $pp \rightarrow pp\pi^0$, and $pp \rightarrow pn\pi^+$ data and (B) using only $pp \rightarrow pp\pi^0$ and $np \rightarrow pp\pi^-$ data). The two estimates obtained by them are shown in Figure 5.8. The two results are not consistent. The inconsistencies are attributed to the uncertainties in different experimental measurements.

Since the indications are that σ_{01} is relatively small in our energy region one might expect the two reactions $pp \rightarrow pp\pi^0$ and $np \rightarrow NN\pi^{\pm}$ to be similar. One

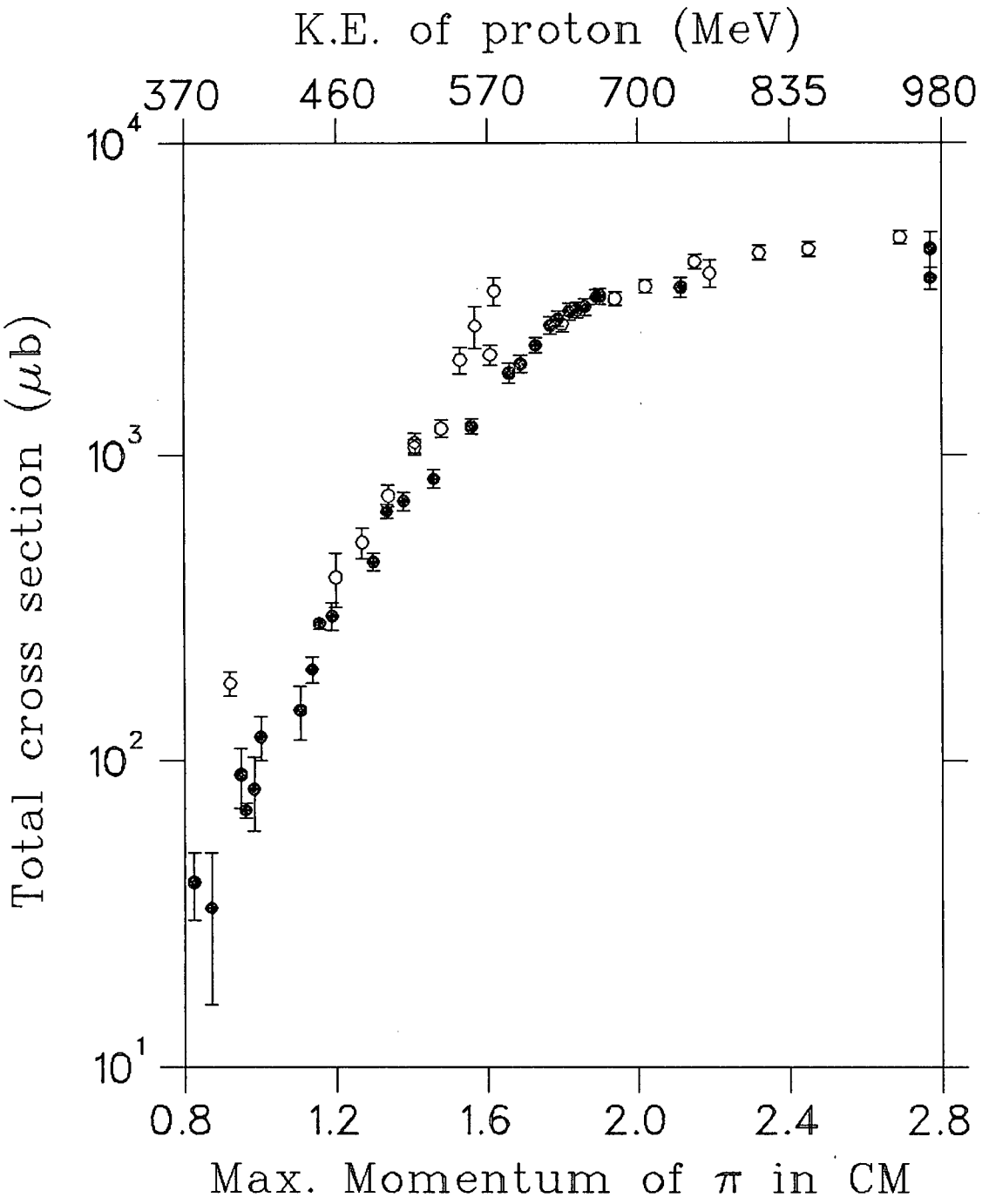

Figure 5.7: Total cross sections for the reaction $pp \rightarrow pp\pi^0$ and $np \rightarrow NN\pi^{\pm}$. The closed circles refer to $pp \rightarrow pp\pi^0$ and open circles correspond to $2\sigma(np \rightarrow NN\pi^{\pm})$

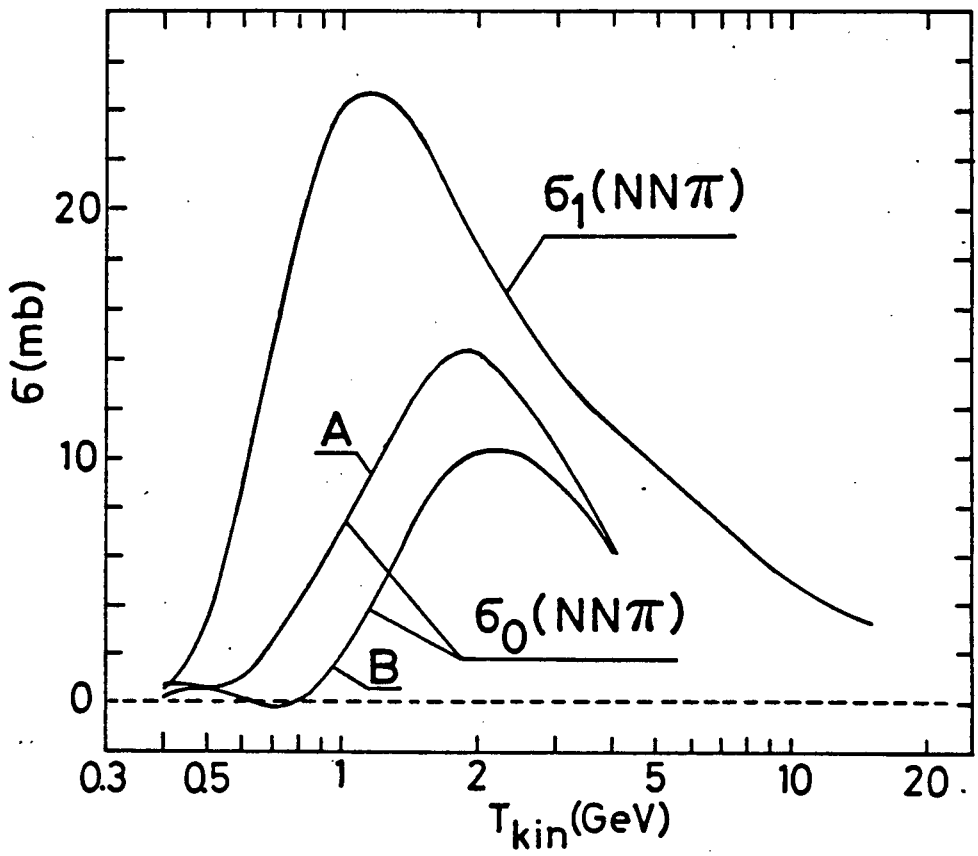

Figure 5.8: Energy dependence of the total cross section for isospin states I=0 and I=1 (from ref [91]).

way of comparing the two reactions is to look at the angular distribution parameter b. We obtained $b \sim 0.04$. However Kleinschmidt et al.[21] obtained $b \sim 0.6$ for the np reaction. Later analysis by the same group indicates that they need to include a $cos\theta$ term in their fit but the $cos^2\theta$ term is likely to remain substantially larger than the same term for $pp \rightarrow pp\pi^0$. We await the results of their new analysis to compare in detail with $pp\pi^0$, but their measurements are similar to earlier results of Nikitin's group at Dubna [23],as well as Handler, so there is little doubt that significant $cos\theta$ and $cos^2\theta$ terms are needed to describe the $\pi^{\pm}$ angular distribution. Thus there must be an important contribution in these reactions from pion production in the I=0 channel. (Note that at 800 MeV the $cos\theta$ term is insignificant [24].)

Yet another way of comparing the two reactions is to look at the energy spectra of the pion. In Figure 5.9 the centre of mass π^+ energy spectrum of Kleinschmidt et al. at 500 MeV is plotted along with the centre of mass energy spectrum of π^0 mesons obtained from the fit to our data. The actual numbers were not available for Kleinschmidt's spectrum, so they were read off their figure. Since the maximum kinetic energy of the pions is different for the two reactions, mainly due to the small mass differences between π^0 and π^+, and between the neutron and proton, our spectrum was scaled and normalised to their spectrum in order to be able to compare the shapes of the two spectra. Now, if there is a difference between the two reactions (due to σ_{01}) the two spectra could be different, but clearly they are very similar apart from the very small bump seen in the $pp \rightarrow pp\pi^0$ spectrum at the highest energy due to the Ss transition. Similarly Thomas et al. [24] found that the π^+ and π^- spectra from np collisions were almost identical at 800 MeV. As no significant difference is seen in such comparisons, σ_{01} is probably small relative to σ_{01}.

In Figure 5.10 the centre of mass π^- momentum spectrum of Handler [20] from the reaction $np \rightarrow pp\pi^-$ is compared with that obtained from our global fit. The

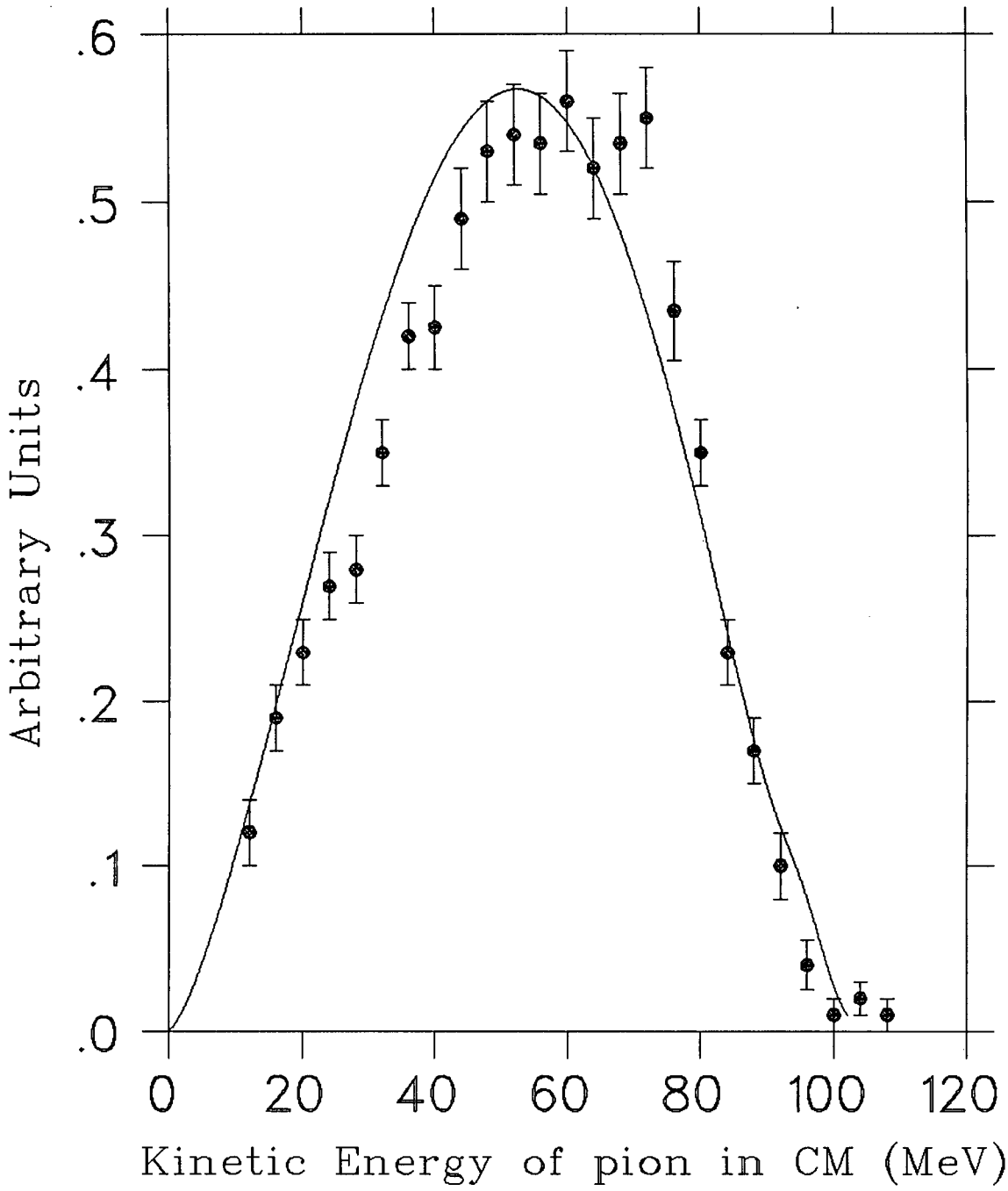

Figure 5.9: The centre of mass energy spectra of pions at 500 MeV. The data points are those of Kleinschmidt et al. for the reaction $np \rightarrow nn\pi^+$ and the smooth curve is for the reaction $pp \rightarrow pp\pi^0$ obtained from the fit to our data (see text).

two spectra look very different. Assuming that Handler's data are correct, some of the differences may be attributed to the following:

1. The $np \rightarrow pp\pi^-$ reaction has a Sp transition (from σ_{01}) which is not available to the $pp \rightarrow pp\pi^0$ reaction. This term enhances the peak at the highest pion momentum.

2. The spectrum obtained by Handler was for an incident neutron energy spectrum ranging from threshold to 440 MeV. The spectrum plotted from our results is for 409 Mev, the mean energy of his neutron spectrum.

But these alone cannot explain the large differences seen. A comparison of the results from the two experiments show noticeable differences. First the $cos\theta$ term observed by Handler requires that the σ_{01} contribution is important. Furthermore, in the analysis of the np data Handler found that the contribution from the Ps transition was negligible ($\sim$ 1%). In our analysis a fairly significant Ps term was observed, though it decreases in favour of the Pp transitions as the energy increases. The fairly large asymmetries observed by us are also in favour of a non negligible Ps term. Handler also found that the Ss contribution to the total cross section was fairly large; i.e. $B_1 \sim 38\mu b$. For the Pp transition he suggested that the contribution from σ_{01} was larger than that from σ_{11}. Overall his estimate was that σ_{01} was comparable to σ_{11}, if not larger. The fairly significant differences seen in the two spectra suggest a large σ_{01} (compared to σ_{11}). Thus there seem to be two effects, one is the large σ_{01} term, the other is that the individual contribution to σ_{11} do not tie in with our results. Is it possible that the information available from Handler's results was not sufficient to avoid ambiguities ? At 500 MeV the differences between the spectra are minimal. This suggests that by 500 MeV σ_{11} has risen much faster than σ_{01}.

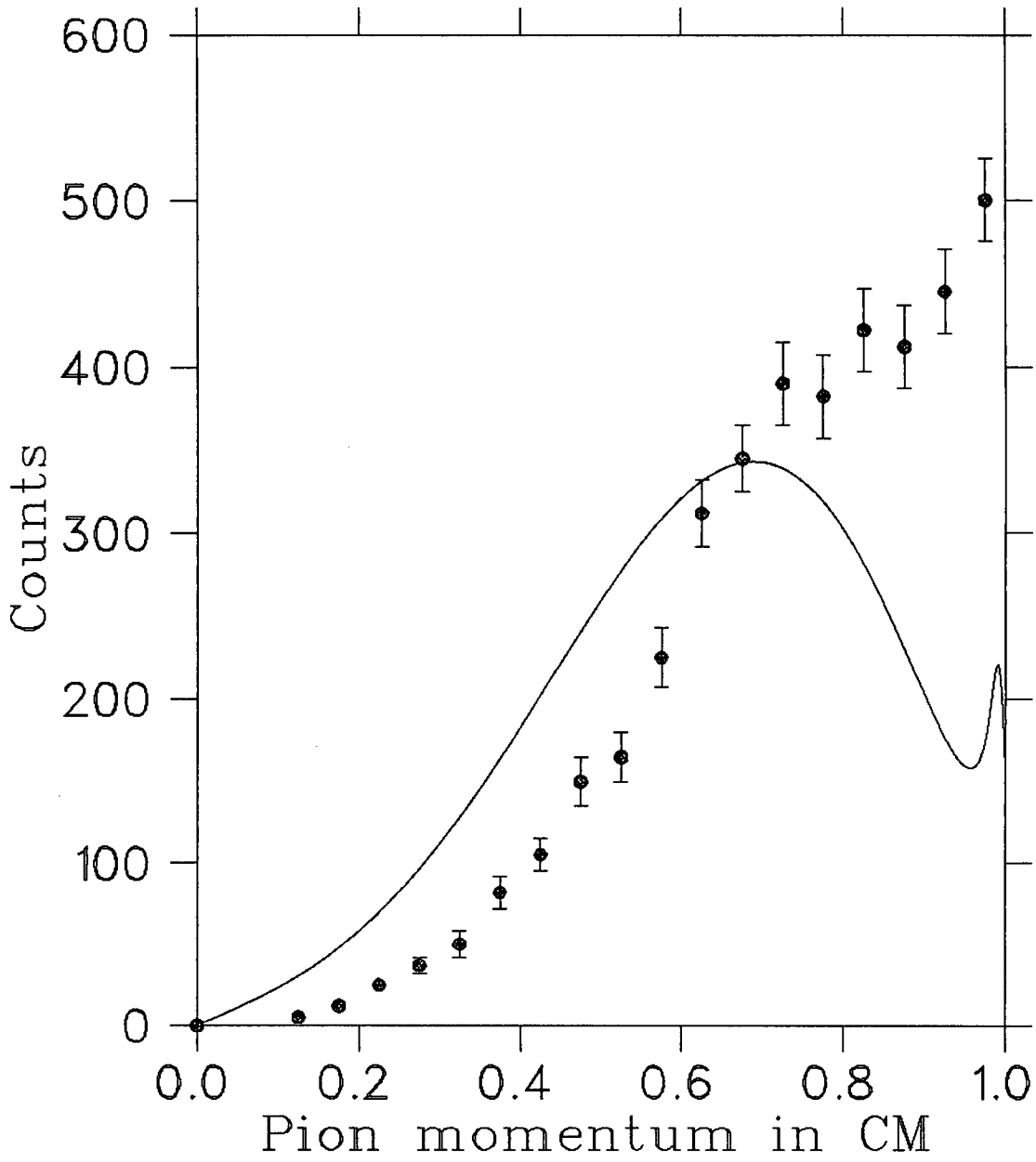

Figure 5.10: The centre of mass momentum spectra of pions at 409 MeV. The momentum is in units of maximum momentum in the CM. The data points are those of Handler for the reaction $np \rightarrow pp\pi^-$ and the smooth curve is for the reaction $pp \rightarrow pp\pi^0$ obtained from the fit to our data (see text).

There is also evidence from the total cross sections, see Figure 5.7. The cross sections observed in the reaction $np \rightarrow \pi^{\pm}NN$ are only slightly greater than $\sigma_{11}/2$, thus σ_{01} can be only a few percent of σ_{11}. Some caution should be exercised however. First the comparison relies on absolute cross sections which are notoriously difficult to obtain (especially if measured in *pd* collisions which is often the case). Secondly it is not clear at what energy to make the comparison, as has been discussed by Kleinschmidt.

In Figure 5.11 are shown the centre of mass π^0 energy spectra obtained from the global fit parameters [from equation 5.5]. Since the Ss transition gives a sharp spike at the highest pion energy, the spectra shown are folded with a gaussian of 2% resolution. These energy spectra are very similar to the ones obtained by Cence et al. [17] at 735 MeV, but are far from the phase space predictions. This is probably because phase space distributions assume an infinite number of angular momentum states which are really not available near threshold. For low π^0 energy the spectra are nearly linear in kinetic energy, a feature which is observed in many pion production reactions, but our experiment is particularly sensitive to this energy region, because the detection efficiency becomes quite large at low π^0 energy.

5.4 Analysing Power

The asymmetry measurements of this investigation are the first such measurements for the reaction $pp \rightarrow pp\pi^0$. The asymmetry observed is principally a result of the interference between the Ps and Pp transitions; because all other terms are relatively small. The large asymmetry observed is consistent with the fairly similar cross sections for the Ps and Pp transitions. The sign of the asymmetry is negative, the same as observed in the $pp \rightarrow \pi^+ d$ and $pp \rightarrow pn\pi^+$ [92] reactions. In an experiment at Indiana Korkmaz et al. [93] have found that there is evidence from the $^{13}C(p,\pi^-)$ reaction at 200 MeV suggesting that the asymmetry for $pn \rightarrow \pi^- pp$

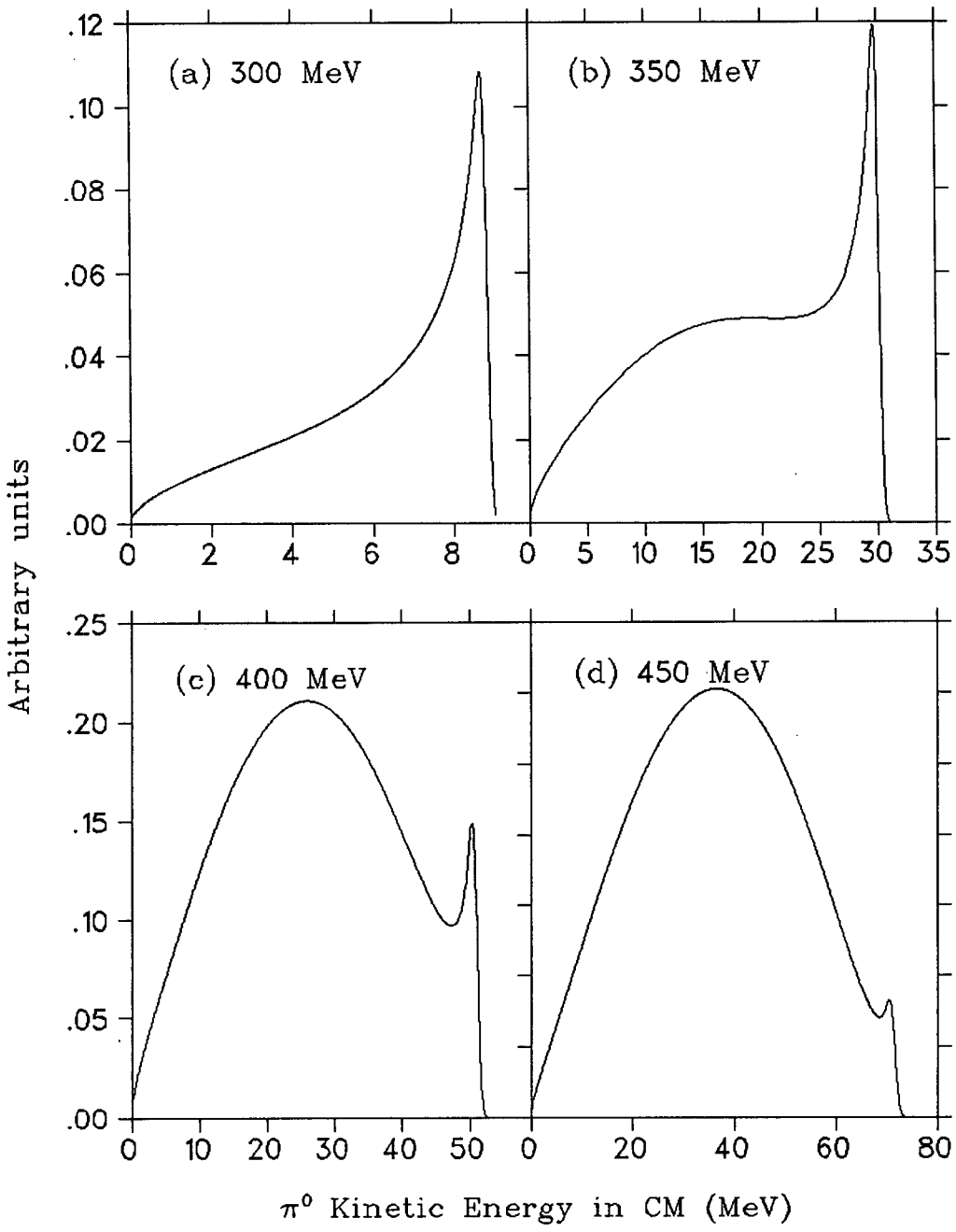

Figure 5.11: The centre of mass energy spectra of π^0at (a) 300 MeV (b) 350 MeV (c) 400 MeV and (d) 450 MeV, calculated from the global fit parameters.

might be positive. This is not found in our measurements, so we need $\pi^{\pm}$ asymmetries from free np collisions to settle this puzzle. Since Handler found σ_{01} to be important at 400 MeV, it would not be strange if the asymmetries for $np \rightarrow NN\pi^{\pm}$ and $pp \rightarrow pp\pi^0$ were quite different in our energy range. Unfortunately at the present moment there are no theoretical predictions for this observable and hence no comparisons can be made.

Since the asymmetry seen is a result of interference, it is possible to use the analysing power results to restrict the uncertainties of σ_T^{Ss} discussed earlier. In order to do this, theoretical calculations are necessary as guidance in showing how the analysing power is related to the various amplitudes of the Ps and Pp transitions. Once this is available they could be fitted to analysing power results to determine the Ps and Pp amplitudes which could be incorporated into the earlier fits to obtain a more dependable value for the B_1 parameter.

5.5 Summary and Conclusions

We have measured the total and differential cross sections and the analysing powers of the π^0 energy spectra for the reaction $pp \rightarrow pp\pi^0$ for five incident proton energies between 319 and 496 MeV. This was done by detecting the γ-rays from the decay of the π^0. The scattered protons were not detected. The cross sections were determined by fitting to the experimental measurements the centre of mass π^0 energy functions which were derived by Gell-Mann . Two types of fits were performed :

1. Individual energy fits, where all π^0 energy spectra at different angles for a given proton energy were fitted simultaneously and

2. Global fits, where spectra at all angles and all proton energies were fitted simultaneously.

Our results for the total cross sections are consistent with the earlier measurements but are of a much higher precision.

Using the π^0 energy and angular distributions we have been able to improve previous measurements and determine accurately the S-wave total cross section. The S-wave total cross section is given by $\sigma_T^{Ss}(\mu b) = (15.2 \pm 3.0)\eta_0^2$ where η_0 is the maximum momentum of the π^0 in the centre of mass in units of the π^0 mass. Because Gell-Mann's relations are valid only near threshold, our model independent result was assessed to be $\sigma_T^{Ss}(\mu b) = (15.2 \pm 6.0)\eta_0^2$. This result is lower than the fits to previous measurements but in good agreement with the predictions of the soft pion calculations of Efrosinin et al.[56] and the non relativistic calculations of Koltun and Reitan [65]. This result should be a very good test for theoretical calculations. Recently there have been a number of fairly successful theoretical calculations on πd elastic scattering and on pion production in proton proton collisions, but none of them has made detailed predictions for the reaction $pp \rightarrow pp\pi^0$. It is interesting that recent results for $\gamma p \rightarrow \pi^0 p$ also find a lower S-wave contribution [94].

We have also estimated the partial cross sections from Ps and Pp transitions. Using the partial cross sections from Ss, Ps and Pp transitions the total cross section can be expressed as:

$$\sigma_{11}(\mu b) = (15.6 \pm 6.0)\eta_0^2 + (17 \pm 8)\eta_0^6 + (66 \pm 11)\eta_0^8 \qquad (5.7)$$

The measured π^0 angular measurements show that in the energy region 319 to 496 MeV, more than 95% of the pions are distributed isotropically in the centre of mass.

The shape of the centre of mass energy spectrum of the π^0 mesons from the reaction $pp \rightarrow pp\pi^0$ is very similar to that of the π^+ mesons from the reaction $np \rightarrow nn\pi^+$ at 500 MeV, but at 409 MeV the π^- energy spectrum from the reaction $np \rightarrow pp\pi^-$ is quite different from that of the π^0 mesons. Now the σ_{01} term is likely

to be mainly an Sp transition which increases as η_0^4 so that at 409 MeV it could be important, but at higher energies it could become relatively smaller because the Ps and Pp terms increase even faster with energy. The total cross sections are also in favour of a small σ_{01} at higher energies, but the $\pi^{\pm}$ angular distributions from the SIN and Dubna data indicate large $cos\theta$ and $cos^2\theta$ terms, so the σ_{01} term is clearly non zero. A σ_{01} term with an amplitude of $\sim$ 30% of σ_{11} ($\sim$10% intensity ratio) could explain all of these results.

Our results for the analysing powers are the first measurements of this observable for the reaction $pp \rightarrow pp\pi^0$. The values are fairly independent of angle and energy and are all significantly negative. These values, along with the Ss total cross sections should prove to be useful in testing theoretical calculations of pion production in nucleon-nucleon collisions.

Bibliography

[1] W.O. Lock and D.F. Measday. Intermediate Energy Nuclear Physics. Methuen and Co Ltd., (1970).

[2] F.H. Cverna et al. Phys. Rev., **C23**:1698, (1981).

[3] K.M. Watson and K.A. Brueckner. Phys. Rev., **83**:1, (1951).

[4] A.H. Rosenfeld. Phys. Rev., **96**:139, (1954).

[5] D.V. Bugg. Ann. Rev. Nucl. Sci., **35**:295, (1985).

[6] D.V. Bugg, A. Hasan, and R.L. Shypit. (1987). TRIUMF received preprint 87-1461.

[7] B.J. VerWest and R.A. Arndt. Phys. Rev, **C25**:1979, (1982).

[8] M. Gell-Mann and K.M. Watson. Ann. Rev. Nucl. Sci., **4**:219, (1954).

[9] J. Marshall, L. Marshall, V.A. Nedzel, and S.D. Warshaw. Phys. Rev., **88**:632, (1952).

[10] J.W. Mather and E.A. Martinelli. Phys. Rev., **92**:780, (1953).

[11] L.M. Soroko. Sov. Phys. JETP, **3**:184, (1956).

[12] B.J. Moyer and R.K. Squire. Phys. Rev., **107**:283, (1957).

[13] Yu. D. Prokoshkin and A.A. Tiapkin. Sov. Phys. JETP, **5**:618, (1957).

[14] R.A. Stallwood, R.B. Sutton, T.H. Fields, J.G. Fox, and J.A. Kane. Phys. Rev., **109**:1716, (1958).

[15] A.F. Dunaitsev and Yu. D. Prokoshkin. Sov. Phys. JETP, **36**:1179, (1959).

[16] F. Shimizu, Y. Kubota, H. Koiso, F. Sai, S. Sakamoto, and S.S. Yamamoto. Nucl. Phys., **A386**:571, (1982).

[17] R.J. Cence, D.L. Lind, G.D. Mead, and B.J. Moyer. Phys. Rev., **131**:2713, (1963).

[18] V.M. Guzhavin et al. Sov. Phys. JETP, **19**:847, (1964).

[19] S. Mandelstam. Proc. Roy. Soc., **A244**:491, (1958).

[20] R. Handler. Phys. Rev., **B138**:1230, (1965).

[21] M. Kleinschmidt, T. Fisher, G. Hammel, W. Hurster, K. Kern, L. Lehmann, E. Rossle, and H. Schmitt. Z. Phys., **A298**:253, (1980).

[22] H. Fisher, J. Franz, V. Grundies, S. Jacoby, A. Klett, P. Koncz, M. Marx, E. Rossle, C. Sauerwein, H. Schledermann, H. Schmitt, and H.L. Woolverton. Pion production in neutron-proton collisions. SIN Newsletter 19, SIN, (1987).

[23] A. Abdivaliev et al. (1981). Dubna preprint JINR D1-81-756.

[24] W. Thomas, R. Carlini, C. Cassapakis, B. Dieterle, J. Donahue, C. Leavitt, T. Rupp, D. Wolfe, M.L. Evans, G. Glass, M. Jain, L. Northcliffe, B. Bonner, and J. Simmons. Phys. Rev., **D24**:1736, (1981).

[25] L.G. Dakhno, A.V. Kravtsov, E.A. Lobachev, M.M. Makarov, V.I. Medvedev, G.Z. Obrant, V.I. Poromov, V.V. Sarantsev, V.M. Sirin, G.L. Sokolov, and S.G. Sherman. Phys. Lett, **114B**:409, (1982).

[26] J. Bystricky, C. Lechanoine-Leluc, and F.Lehar. J. Phys., **48**:199, (1987).

[27] D.V. Bugg. Nucl. Phys., **A437**:534, (1985).

[28] C. Lechanoine-LeLuc. Nucleon-nucleon scattering at intermediate energies. In Proceedings of the 7th international symposium on high energy spin physics, Protvino (USSR), (1986).

[29] A.B. Wicklund, M.W. Arenton, D.S. Ayres, R. Diebold, E.N. May, L.J. Nodulman, J.R. Sauer, E.C. Swallow, M.M. Calkin, M.D. Corcoran, J. Hoftiezer, H.E. Miettinen, and G.S. Mutchler. Phys. Rev., **D35**:2670, (1987).

[30] R.A. Arndt, L.D. Roper, R.A. Bryan, R.B. Clark, B.J. VerWest, and P. Signell. Phys. Rev., **D28**:97, (1983).

[31] N. Davison. (1986). TRIUMF EEC proposal, exp.372.

[32] U. Amaldi, Jr. Rev. Mod. Phys., **39**:649, (1967).

[33] A. Matsuyama and T.-S.H. Lee. Phys. Rev., **C34**:1900, (1986).

[34] A.M. Green and J.A. Niskanen. Nucl. Phys., **A271**:503, (1976).

[35] P.U. Sauer. Prog. Part. Nucl. Phys., **16**:35, (1986).

[36] J.A. Niskanen. Nucl. Phys., **A298**:417, (1978).

[37] J.A. Niskanen. Phys. Lett., **141B**:301, (1984).

[38] S.C.B. Andrade and E. Ferreira. Phys. Rev., **C34**:226, (1986).

[39] H. Garcilazo and L. Mathelitsch. Phys. Rev., **C34**:1425, (1986).

[40] T. Mizutani, B. Saghai, C. Fayard, and G.H. Lamot. Phys. Rev., **C35**:667, (1987).

[41] E. Ferrari and F. Selleri. Nuovo Cimento, **27**:1450, (1963).

[42] W.Busza et al. Nuovo Cimento, **42A**:871, (1966).

[43] P.C. Gugelot, S. Kullander, G. Landau, F. Lemeilleur, and J. Yonnet. Nucl. Phys., **B37**:93, (1972).

[44] A. König and P. Kroll. Nucl. Phys., **A356**:345, (1981).

[45] B.J. VerWest. Phys. Lett., **83B**:161, (1979).

[46] G. Glass et al. Nucleon - Nucleon interaction, page 305. AIP, New York, (1978).

[47] J.H. Gruben and B.J. VerWest. Phys. Rev., **C28**:836, (1983).

[48] V.K. Suslenko and I.I. Haysak. Sov. J. Nucl. Phys., **43**:252, (1986).

[49] S.L. Adler and Y. Dothan. Phys. Rev., **151**:1267, (1966).

[50] D.S. Beder. Nuovo Cimento, **56A**:625, (1968).

[51] R. Baier and H. Kühnelt. Nuovo Cimento, **63A**:135, (1969).

[52] M. Schillaci, R.R. Silbar, and J.E. Young. Phys. Rev., **179**:1539, (1969).

[53] D. Drechsel and H.J. Weber. Nucl. Phys., **B25**:159, (1970).

[54] F. Hachenberg and H.J. Pirner. Ann. Phys., **112**:401, (1978).

[55] V.P. Efrosinin, D.A. Zaikin, and I.I. Osipchuk. Sov. J. Nucl. Phys., **42**:604, (1985).

[56] V.P. Efrosinin, D.A. Zaikin, and I.I. Osipchuk. Z. Phys., **A322**:322, (1985).

[57] W.M. Kloet and R.R. Silbar. Nucl. Phys., **A338**:281, (1980).

[58] J. Dubach, W.M. Kloet, and R.R.Silbar. Nucl. Phys., **A466**:573, (1987).

[59] R. Aaron, R.D. Amado, and J.E. Young. Phys. Rev., **174**:2022, (1968).

[60] Y. Avishai and T. Mizutani. Nucl. Phys., **A326**:352, (1979).

[61] Y. Avishai and T. Mizutani. Phys. Rev., **C27**:312, (1983).

[62] H. Tanabe and K. Ohta. Phys. Rev., **C36**:2495, (1987).

[63] T. Ueda. Nucl. Phys., **A463**:69, (1987).

[64] T.-S.H. Lee and A. Matsuyama. Phys. Rev., **C36**:1459, (1987).

[65] D.S. Koltun and A. Reitan. Phys. Rev., **141**:1413, (1966).

[66] T. Hamada and I.D. Johnston. Nucl. Phys., **34**:382, (1962).

[67] D. Zollmann. Phys. Rev., **C2**:2128, (1970).

[68] E. van Faassen and J.A. Tjon. Phys. Rev., **C33**:2105, (1986).

[69] I.R. Afnan and B. Blankleider. Phys. Rev., **C32**:2006, (1985).

[70] G.E. Brown and M. Rho. Phys. Lett., **82B**:177, (1979).

[71] A. Chodos and C.B. Thorn. Phys. Rev., **D12**:2733, (1975).

[72] Z.-J. Cao and W-Y.B. Hwang. Phys. Rev., **C34**:1785, (1986).

[73] M. Harvey, J. Letourneux, and B. Lorazo. Nucl. Phys., **A424**:428, (1984).

[74] A. Faessler, F. Fernandez, G. Lübeck, and K. Shimizu. Nucl. Phys., **A402**:555, (1983).

[75] M.P. Locher, M.E. Sainio, and A. Švarc. Advances in Nucl. Phys., **17**:47, (1986).

[76] H. Hidaka, A. Beretvas, K. Nield, H. Spinka, D. Underwood, Y. Watanabe, and A. Yokosawa. Phys. Lett., **70B**:479, (1977).

[77] W. Jauch, A. Koenig, and P. Kroll. Phys. Lett., **143B**:509, (1984).

[78] R.L. Shypit, D.V. Bugg, D.M. Lee, M.W. McNaughton, R.R. Silbar, N.M. Stewart, A.S. Clough, C.L. Hollas, K.H. McNaughton, P. Riley, and C.A. Davis. Phys. Rev. Lett., **60**:901, (1988).

[79] J.F. Bartlett, J.R. Biel, D.B. Curtis, R.J. Dosen, T.D. Lagerhund, E.K. Quigg, D.J. Ritchie, and L.M. Taff. Fermilab multi computer program for data acquisition and analysis. 1981. TRIUMF implementation by Y. Miles.

[80] Anne W. Bennett. A command language programme:**MOLLI**. 1983. MOLLI, A command language programme that reads data written with the TRIUMF Data Acquisition programme (commonly known as the MULTI format.) Initially written in April 1983 by A. Bennett and subsequently revised by J. Lloyd in June 1983.

[81] F. James and M. Roos. Comp. Phys. Comm., **10**:343, (1975).

[82] R.E. Marshak. Meson Physics, chapter 3. McGraw-Hill, New York, (1952).

[83] M. Salomon, D.F. Measday, J.-M. Poutissou, and B.C. Robertson. Nucl. Phys., **A414**:493, (1984).

[84] R.L. Ford and W.R. Nelson. The EGS code system: computer programs for the Monte Carlo simulation of electromagnetic cascade showers (version 3). (1978).

[85] A.Bagheri. The pion-nucleon interaction at low energy. PhD thesis, University of British Columbia, 1986. unpublished.

[86] Gunnar Kallen. Elementary Particle Physics, pages 31–33. Addison-Wesley publishing company, (1964).

[87] B. Bassalleck, F. Corriveau, M.D. Hasinoff, T. Marks, D.F. Measday, J.-M. Poutissou, and M. Salomon. Nucl. Phys., **A362**:445, (1981).

[88] H.H. Barschall and W. Haeberli. Polarisation phenomena in nuclear reactions, page xxv. The University of Wisconsin, (1970).

[89] J.Marshall, L. Marshall, V.A. Nedzel, and S.D. Warshaw. Phys. Rev., **88**:632, (1952).

[90] J. Spuller and D.F. Measday. Phys. Rev., **D12**:3550, (1975).

[91] J. Bystricky, P.La France, F. Lehar, F. Perrot, T. Siemiarczuk, and P. Winternitz. (1987). Saclay preprint DPhPE 87-03, to be published in J. Phys.

[92] W.R. Falk, E.G. Auld, G. Giles, G. Jones, G.J. Lolos, W. Ziegler, and P.L. Walden. Phys. Rev., **C32**:1972, (1985).

[93] E. Korkmaz, L.C. Bland, W.W. Jacobs, T.G. Throwe, S.E. Vidgor, M.C. Green, P.L. Jolivette, and J.D. Brown. Phys. Rev. Lett., **58**:104, (1987).

[94] E. Mazzucato, P. Argan, G. Audit, A. Bloch, N. de Botton, N. d'Hose, J.L. Faure, M.L. Ghedira, C. Guerra, J. Martin, C. Schuhl, G. Tamas, and E. Vincent. Phys. Rev. Lett., **57**:3144, (1986).

Appendix A

The Analysing Powers

Table A.1: π^0 Analysing powers for the reaction $p+p \rightarrow p+p+\pi^0$ obtained from the 180^0 geometry at 496 MeV.

π^0 Laboratory Angle	π^0 Laboratory Kinetic Energy (MeV)	Analysing Power
40^0	2.5	0.18 ± 0.16
	10	-0.37 ± 0.31
	20	-0.54 ± 0.33
	30	-0.53 ± 0.33
	40	-0.21 ± 0.33
	50	-0.53 ± 0.27
	60	-0.27 ± 0.34
	70	-0.64 ± 0.30
	80	-0.62 ± 0.29
	90	-0.36 ± 0.31
	100	-0.58 ± 0.44
	110	-0.37 ± 0.32
60^0	2.5	-0.52 ± 0.15
	10	-0.14 ± 0.18
	20	-0.33 ± 0.19
	30	-0.37 ± 0.23
	40	-0.17 ± 0.23
	50	-0.76 ± 0.26
	60	-0.61 ± 0.26

Table A.2: π^0 Analysing powers for the reaction $p+p \rightarrow p+p+\pi^0$ obtained from the 180^0 geometry at 496 MeV.

π^0 Laboratory Angle	π^0 Laboratory Kinetic Energy (MeV)	Analysing Power
80^0	2.5	-0.38 ± 0.14
	10	-0.01 ± 0.16
	20	-0.67 ± 0.20
	30	-0.93 ± 0.29
	40	-0.51 ± 0.27
	50	-0.93 ± 0.43
	60	-0.72 ± 0.50
90^0	2.5	-0.22 ± 0.05
	10	-0.30 ± 0.07
	20	-0.26 ± 0.08
	30	-0.37 ± 0.09
	40	-0.43 ± 0.14
	50	-0.53 ± 0.24
100^0	2.5	-0.02 ± 0.11
	10	-0.26 ± 0.13
	20	-0.40 ± 0.15
	30	-0.68 ± 0.24
120^0	2.5	0.11 ± 0.11
	10	-0.35 ± 0.16
	20	-0.70 ± 0.47
140^0	2.5	-0.09 ± 0.09
	10	-0.44 ± 0.17
	20	-0.15 ± 0.66

Table A.3: π^0 Analysing powers for the reaction $p+p \rightarrow p+p+\pi^0$ obtained from the 180^0 geometry at 450 MeV.

π^0 Laboratory Angle	π^0 Laboratory Kinetic Energy (MeV)	Analysing Power
40^0	2.5	-0.10 ± 0.08
	10	-0.10 ± 0.15
	20	0.01 ± 0.17
	30	-0.60 ± 0.15
	40	-0.01 ± 0.15
	50	-0.28 ± 0.14
	60	-0.15 ± 0.16
	70	-0.25 ± 0.16
	80	-0.25 ± 0.26
	90	-0.39 ± 0.25
	100	-0.56 ± 0.50
60^0	2.5	-0.33 ± 0.09
	10	-0.39 ± 0.11
	20	-0.39 ± 0.11
	30	-0.39 ± 0.15
	40	-0.18 ± 0.13
	50	-0.52 ± 0.22
	60	-0.56 ± 0.34
80^0	2.5	-0.18 ± 0.06
	10	-0.30 ± 0.08
	20	-0.40 ± 0.11
	30	-0.35 ± 0.20
	40	-0.30 ± 0.40

Table A.4: π^0 Analysing powers for the reaction $p+p \rightarrow p+p+\pi^0$ obtained from the 180^0 geometry at 450 MeV.

π^0 Laboratory Angle	π^0 Laboratory Kinetic Energy (MeV)	Analysing Power
90^0	2.5	-0.31 ± 0.04
	10	-0.28 ± 0.06
	20	-0.34 ± 0.07
	30	-0.64 ± 0.13
	40	-0.25 ± 0.27
100^0	2.5	-0.13 ± 0.06
	10	-0.21 ± 0.09
	20	-0.43 ± 0.13
	30	-0.20 ± 0.28
120^0	2.5	-0.35 ± 0.07
	10	-0.16 ± 0.14
	20	0.27 ± 1.47
140^0	2.5	-0.27 ± 0.08
	10	-0.27 ± 0.13

Table A.5: π^0 Analysing powers for the reaction $p+p \rightarrow p+p+\pi^0$ obtained from the 180^0 geometry at 402, 349 and 319 MeV.

π^0 Laboratory Angle	π^0 Laboratory Kinetic Energy (MeV)	Analysing Power
40^0	2.5	-0.11 ± 0.13
	10	-0.24 ± 0.14
	20	-0.41 ± 0.15
	30	-0.40 ± 0.16
	40	-0.52 ± 0.18
	50	-0.17 ± 0.21
	60	0.45 ± 0.54
	70	0.25 ± 1.13
60^0	2.5	-0.14 ± 0.07
	10	-0.30 ± 0.08
	20	-0.32 ± 0.10
	30	-0.22 ± 0.13
	40	-0.36 ± 0.15
	50	-0.49 ± 0.40
80^0	2.5	-0.17 ± 0.07
	10	-0.25 ± 0.13
	20	-0.11 ± 0.22
90^0	2.5	-0.08 ± 0.05
	10	-0.35 ± 0.10
	20	-0.33 ± 0.18
	30	-0.38 ± 0.57
100^0	2.5	-0.17 ± 0.07
	10	-0.35 ± 0.12
120^0	2.5	-0.15 ± 0.08
	10	-0.12 ± 0.56
140^0	2.5	-0.13 ± 0.17

Table A.6: π^0 Analysing powers for the reaction $p+p \rightarrow p+p+\pi^0$ obtained from the 180^0 geometry at 349 and 319 MeV.

Proton Energy (MeV)	π^0 Laboratory Angle	π^0 Laboratory Kinetic Energy (MeV)	Analysing Power
349	60^0	2.5	0.19 ± 0.27
		10	-0.16 ± 0.35
		20	-0.06 ± 0.49
	80^0	2.5	-0.20 ± 0.08
		10	-0.24 ± 0.15
	90^0	2.5	-0.14 ± 0.07
		10	-0.20 ± 0.17
	100^0	2.5	-0.12 ± 0.12
		10	-0.63 ± 0.81
	120^0	2.5	-0.49 ± 0.86
		10	-0.50 ± 0.90
320	90^0	2.5	-0.04 ± 0.08

Table A.7: π^0 Analysing powers for the reaction $p + p \rightarrow p + p + \pi^0$ obtained from the symmetric geometry at 450 and 402 MeV.

Proton Energy (MeV)	Geometry	π^0 Laboratory Angle	π^0 Laboratory Kinetic Energy (MeV)	Analysing Power
450	40^0-40^0	0	70	-0.22 ± 0.09
		10	80	-0.27 ± 0.08
		17	90	-0.47 ± 0.08
		21	100	-0.28 ± 0.09
		23	110	-0.42 ± 0.13
		25	120	-0.20 ± 0.17
		27	130	-0.11 ± 0.26
		28	140	-0.29 ± 0.45
	60^0-60^0	1	20	-0.31 ± 0.10
		30	30	-0.47 ± 0.10
		38	40	-0.47 ± 0.10
		43	50	-0.64 ± 0.11
		46	60	-0.39 ± 0.14
		48	70	-0.77 ± 0.15
		50	80	-0.26 ± 0.34
402	40^0-40^0	0	70	-0.19 ± 0.10
		10	80	-0.25 ± 0.11
		17	90	-0.18 ± 0.26
	60^0-60^0	1	20	-0.49 ± 0.07
		30	30	-0.22 ± 0.08
		38	40	-0.40 ± 0.09
		43	50	-0.37 ± 0.13
		46	60	-0.41 ± 0.27

Table A.8: π^0 Analysing powers for the reaction $p+p \rightarrow p+p+\pi^0$ obtained from the symmetric geometry at 496 MeV.

Geometry	π^0 Laboratory Angle	π^0 Laboratory Kinetic Energy (MeV)	Analysing Power
60^0-60^0	1	20	-0.14 ± 0.16
	30	30	-0.38 ± 0.14
	38	40	-0.55 ± 0.14
	43	50	-0.75 ± 0.14
	46	60	-0.41 ± 0.13
	48	70	-0.49 ± 0.16
	50	80	-0.30 ± 0.16
	51	90	-0.68 ± 0.25
	52	100	-0.47 ± 0.38
70^0-70^0	0	2.5	-0.81 ± 0.27
	20	10	0.17 ± 0.17
	46	20	-0.48 ± 0.16
	53	30	-0.23 ± 0.16
	57	40	-0.52 ± 0.15
	60	50	-0.19 ± 0.16
	62	60	-0.60 ± 0.17
80^0-80^0	4	2.5	-0.21 ± 0.09
	61	10	-0.36 ± 0.12
	69	20	-0.35 ± 0.13
	72	30	-0.53 ± 0.15
	74	40	-0.47 ± 0.15
	75	50	-0.57 ± 0.22
	76	60	-0.44 ± 0.43

PUBLICATIONS

1. J. R. H. Smith, A. S. Clough, D. F. Jackson, K. R. Smith, D. F. Measday, F. Entezami, A. J. Noble, S. Stanislaus, C. J. Virtue, M. Salomon, K. A. Aniole
   "Gamma-ray coincidence measurements for studies on pion chemistry"
   Nuclear Instruments and Methods **A242**,465(1986).

2. S. Stanislaus, F. Entezami, A. Bagheri, D. F. Measday and D. Garner
   "Atomic Capture ratios for muons in oxides"
   Nuclear Physics **A475**,630(1987).

3. S. Stanislaus, F. Entezami, and D. F. Measday
   "Atomic Capture of muons and density"
   Nuclear Physics **A475**,642(1987).

4. S. Stanislaus, A. J. Noble, M. Ahmad, D. F. Measday, D. Horváth, M. Salomon
   "Study of the reaction $p + p \rightarrow p + p + \pi^0$"
   Proceedings of the LAMPF Workshop on Photon and Neutral Meson Physics at Intermediate Energies, January 1987, Los Alamos, p435.

5. D. F. Measday, M. S. Ahmad, A. J. Noble,S. Stanislaus, D. Horváth and M. Salomon
   "Pion production in Nucleon-Nucleon Collisions below 600 MeV"
   Proceedings of the International Conference on the Theory of Few-Body and Quark-Hadronic Systems, June 1987, JINR, Dubna.